Draft version July 16, 2024
Typeset using LaTeX **twocolumn** style in AASTeX631

Swift-BAT GUANO follow-up of gravitational-wave triggers in the third LIGO–Virgo–KAGRA observing run

The Swift-BAT/GUANO Team

Gayathri Raman,[1] Samuele Ronchini,[1] James Delaunay,[2,1] Aaron Tohuvavohu,[3,4] Jamie A. Kennea,[1]
Tyler Parsotan,[5]

The Swift Collaboration

Elena Ambrosi,[6] Maria Grazia Bernardini,[7] Sergio Campana,[7] Giancarlo Cusumano,[6] Antonino D'Aì,[6]
Paolo D'Avanzo,[7] Valerio D'Elia,[8,9] Massimiliano De Pasquale,[10] Simone Dichiara,[1] Phil Evans,[11]
Dieter Hartmann,[12] Paul Kuin,[13] Andrea Melandri,[14] Paul O'Brien,[11] Julian P. Osborne,[11] Kim Page,[11]
David M. Palmer,[15] Boris Sbarufatti,[16] Gianpiero Tagliaferri,[7] Eleonora Troja,[17]

The LIGO Scientific Collaboration, the Virgo Collaboration, and the KAGRA Collaboration

A. G. Abac,[18] R. Abbott,[19] H. Abe,[20] I. Abouelfettouh,[21] F. Acernese,[22,23] K. Ackley,[24] C. Adamcewicz,[25]
S. Adhicary,[26] N. Adhikari,[27] R. X. Adhikari,[19] V. K. Adkins,[28] V. B. Adya,[29] C. Affeldt,[30,31]
D. Agarwal,[32] M. Agathos,[33] O. D. Aguiar,[34] I. Aguilar,[35] L. Aiello,[36] A. Ain,[37] T. Akutsu,[38,39]
S. Albanesi,[40,41] R. A. Alfaidi,[42] A. Al-Jodah,[43] C. Alléné,[44] A. Allocca,[45,23] S. Al-Shammari,[36]
P. A. Altin,[29] S. Alvarez-Lopez,[46] A. Amato,[47,48] L. Amez-Droz,[49] A. Amorosi,[49] C. Amra,[50] S. Anand,[19]
A. Ananyeva,[19] S. B. Anderson,[19] W. G. Anderson,[19] M. Andia,[51] M. Ando,[52] T. Andrade,[53]
N. Andres,[44] M. Andrés-Carcasona,[54] T. Andrić,[18,55] J. Anglin,[56] S. Ansoldi,[57,58] J. M. Antelis,[59]
S. Antier,[60] M. Aoumi,[61] E. Z. Appavuravther,[62,63] S. Appert,[19] S. K. Apple,[64] K. Arai,[19] A. Araya,[65]
M. C. Araya,[19] J. S. Areeda,[66] N. Aritomi,[21] F. Armato,[67] N. Arnaud,[51,68] M. Arogeti,[69]
S. M. Aronson,[28] G. Ashton,[70] Y. Aso,[38,71] M. Assiduo,[72,73] S. Assis de Souza Melo,[68] S. M. Aston,[74]
P. Astone,[75] F. Aubin,[76] K. AultONeal,[59] G. Avallone,[77] S. Babak,[78] F. Badaracco,[67]
C. Badger,[79] S. Bae,[80] S. Bagnasco,[41] E. Bagui,[81] Y. Bai,[19] J. G. Baier,[82] R. Bajpai,[38] T. Baka,[83]
M. Ball,[84] G. Ballardin,[68] S. W. Ballmer,[85] S. Banagiri,[86] B. Banerjee,[55] D. Bankar,[32] P. Baral,[27]
J. C. Barayoga,[19] B. C. Barish,[19] D. Barker,[21] P. Barneo,[53,87] F. Barone,[88,23] B. Barr,[42] L. Barsotti,[46]
M. Barsuglia,[78] D. Barta,[89] S. D. Barthelmy,[90] M. A. Barton,[42] I. Bartos,[56] S. Basak,[91]
A. Basalaev,[92] R. Bassiri,[35] A. Basti,[93,37] M. Bawaj,[94,62] P. Baxi,[95] J. C. Bayley,[42] A. C. Baylor,[27]
M. Bazzan,[96,97] B. Bécsy,[98] V. M. Bedakihale,[99] F. Beirnaert,[100] M. Bejger,[101] D. Belardinelli,[102]
A. S. Bell,[42] V. Benedetto,[103] D. Beniwal,[104] W. Benoit,[105] J. D. Bentley,[92] M. Ben Yaala,[106]
S. Bera,[107] M. Berbel,[108] F. Bergamin,[30,31] B. K. Berger,[35] S. Bernuzzi,[109] M. Beroiz,[19]
C. P. L. Berry,[42] D. Bersanetti,[67] A. Bertolini,[48] J. Betzwieser,[74] D. Beveridge,[43] N. Bevins,[110]
R. Bhandare,[111] U. Bhardwaj,[112,48] R. Bhatt,[19] D. Bhattacharjee,[82,113] S. Bhaumik,[56] S. Bhowmick,[114]
A. Bianchi,[48,115] I. A. Bilenko,[116] G. Billingsley,[19] A. Binetti,[117] S. Bini,[118,119] O. Birnholtz,[120]
S. Biscoveanu,[86,46] A. Bisht,[31] M. Bitossi,[68,37] M.-A. Bizouard,[60] J. K. Blackburn,[19] C. D. Blair,[43,74]
D. G. Blair,[43] F. Bobba,[77,121] N. Bode,[30,31] G. Bogaert,[60] G. Boileau,[122,60] M. Boldrini,[123,75]
G. N. Bolingbroke,[104] A. Bolliand,[124,50] L. D. Bonavena,[96] R. Bondarescu,[53] F. Bondu,[125]
E. Bonilla,[35] M. S. Bonilla,[66] A. Bonino,[126] R. Bonnand,[44] P. Booker,[30,31] A. Borchers,[30,31]
V. Boschi,[37] S. Bose,[32] V. Bossilkov,[74] V. Boudart,[127] A. Boumerdassi,[36] A. Bozzi,[68] C. Bradaschia,[37]
P. R. Brady,[27] M. Braglia,[128] A. Branch,[74] M. Branchesi,[55,129] M. Breschi,[109] T. Briant,[130]
A. Brillet,[60] M. Brinkmann,[30,31] P. Brockill,[27] E. Brockmueller,[30,31] A. F. Brooks,[19] D. D. Brown,[104]
M. L. Brozzetti,[94,62] S. Brunett,[19] G. Bruno,[131] R. Bruntz,[132] J. Bryant,[126] F. Bucci,[73] J. Buchanan,[132]
O. Bulashenko,[53,87] T. Bulik,[133] H. J. Bulten,[48] A. Buonanno,[134,18] K. Burtnyk,[21] R. Buscicchio,[135,136]
D. Buskulic,[44] C. Buy,[137] R. L. Byer,[35] G. S. Cabourn Davies,[138] G. Cabras,[57,58] R. Cabrita,[131]
L. Cadonati,[69] G. Cagnoli,[139] C. Cahillane,[85] J. Calderón Bustillo,[140] J. D. Callaghan,[42]
T. A. Callister,[141] E. Calloni,[45,23] J. B. Camp,[90] M. Canepa,[142,67] G. Caneva Santoro,[54]
M. Cannavacciuolo,[77] K. C. Cannon,[52] H. Cao,[143] Z. Cao,[144] L. A. Capistran,[145] E. Capocasa,[78]
E. Capote,[85] G. Carapella,[77,121] F. Carbognani,[68] M. Carlassara,[30,31] J. B. Carlin,[146] M. Carpinelli,[135,147,68]
G. Carrillo,[84] J. J. Carter,[30,31] G. Carullo,[148] J. Casanueva Diaz,[68] C. Casentini,[149,102] G. Castaldi,[150]
S. Y. Castro-Lucas,[114] S. Caudill,[151,48,83] M. Cavaglià,[113] R. Cavalieri,[68] G. Cella,[37]

P. Cerdá-Durán,[152,153] E. Cesarini,[102] W. Chaibi,[60] P. Chakraborty,[30,31]
S. Chalathadka Subrahmanya,[92] C. Chan,[52] J. C. L. Chan,[141] K. H. M. Chan,[154] M. Chan,[155]
W. L. Chan,[154] K. Chandra,[156] R.-J. Chang,[157] P. Chanial,[78] S. Chao,[158,159] C. Chapman-Bird,[42]
E. L. Charlton,[132] P. Charlton,[160] E. Chassande-Mottin,[78] C. Chatterjee,[43] Debarati Chatterjee,[32]
Deep Chatterjee,[46] M. Chaturvedi,[111] S. Chaty,[78] A. Chen,[161] A. H.-Y. Chen,[162] D. Chen,[163] H. Chen,[158]
H. Y. Chen,[164] K. H. Chen,[159] X. Chen,[43] Yi-Ru Chen,[158] Yanbei Chen,[165] Yitian Chen,[166] H. P. Cheng,[56]
P. Chessa,[93,37] H. T. Cheung,[95] H. Y. Chia,[56] F. Chiadini,[167,121] C. Chiang,[159] G. Chiarini,[97] A. Chiba,[168]
R. Chiba,[169] R. Chierici,[170] A. Chincarini,[67] M. L. Chiofalo,[93,37] A. Chiummo,[23,68] C. Chou,[162]
S. Choudhary,[43] N. Christensen,[60] S. S. Y. Chua,[29] K. W. Chung,[79] G. Ciani,[96,97] P. Ciecielag,[101]
M. Cieślar,[101] M. Cifaldi,[102] A. A. Ciobanu,[104] R. Ciolfi,[171,97] F. Clara,[21] J. A. Clark,[19,69]
T. A. Clarke,[25] P. Clearwater,[172] S. Clesse,[81] F. Cleva,[60] E. Coccia,[55,129,54] E. Codazzo,[55]
P.-F. Cohadon,[130] M. Colleoni,[107] C. G. Collette,[49] J. Collins,[74] S. Colloms,[42] A. Colombo,[135,136,173]
M. Colpi,[135,136] C. M. Compton,[21] L. Conti,[97] S. J. Cooper,[126] T. R. Corbitt,[28]
I. Cordero-Carrión,[174] S. Corezzi,[94,62] N. J. Cornish,[98] A. Corsi,[175] S. Cortese,[68] C. A. Costa,[34]
R. Cottingham,[74] M. W. Coughlin,[105] A. Couineaux,[75] J.-P. Coulon,[60] S. T. Countryman,[176]
J.-F. Coupechoux,[170] B. Cousins,[26] P. Couvares,[19,69] D. M. Coward,[43] M. J. Cowart,[74] D. C. Coyne,[19]
R. Coyne,[177] K. Craig,[106] R. Creed,[36] J. D. E. Creighton,[27] T. D. Creighton,[178] P. Cremonese,[107]
A. W. Criswell,[105] J. C. G. Crockett-Gray,[28] M. Croquette,[130] R. Crouch,[21] S. G. Crowder,[179]
J. R. Cudell,[127] T. J. Cullen,[19] A. Cumming,[42] E. Cuoco,[68,180,37] M. Cusinato,[152] P. Dabadie,[139]
T. Dal Canton,[51] S. Dall'Osso,[75] G. Dálya,[100] B. D'Angelo,[67] S. Danilishin,[47,48] S. D'Antonio,[102]
K. Danzmann,[31,30,31] K. E. Darroch,[132] L. P. Dartez,[21] A. Dasgupta,[99] S. Datta,[181] V. Dattilo,[68] A. Daumas,[78]
N. Davari,[182,147] I. Dave,[111] A. Davenport,[114] M. Davier,[51] T. F. Davies,[43] D. Davis,[19] L. Davis,[43]
M. C. Davis,[110] E. J. Daw,[183] M. Dax,[18] J. De Bolle,[100] M. Deenadayalan,[32] J. Degallaix,[184]
M. De Laurentis,[45,23] S. Deléglise,[130] V. Del Favero,[90] F. De Lillo,[131] D. Dell'Aquila,[182,147]
W. Del Pozzo,[93,37] F. De Marco,[75,123] F. De Matteis,[149,102] V. D'Emilio,[36] N. Demos,[46] T. Dent,[140]
A. Depasse,[131] N. DePergola,[110] R. De Pietri,[185,186] R. De Rosa,[45,23] C. De Rossi,[68] R. De Simone,[167]
A. Dhani,[18] S. Dhurandhar,[32] R. Diab,[56] M. C. Díaz,[178] M. Di Cesare,[45] G. Dideron,[187] N. A. Didio,[85]
T. Dietrich,[18] L. Di Fiore,[23] C. Di Fronzo,[49] F. Di Giovanni,[152] M. Di Giovanni,[123,75]
T. Di Girolamo,[45,23] D. Diksha,[48,47] A. Di Michele,[94] J. Ding,[78,188] S. Di Pace,[123,75] I. Di Palma,[123,75]
F. Di Renzo,[170] Divyajyoti,[189] A. Dmitriev,[126] Z. Doctor,[86] E. Dohmen,[21] P. P. Doleva,[132]
L. Donahue,[190] L. D'Onofrio,[75] F. Donovan,[46] K. L. Dooley,[36] T. Dooney,[83] S. Doravari,[32] O. Dorosh,[191]
M. Drago,[123,75] J. C. Driggers,[21] Y. Drori,[19] J.-G. Ducoin,[192,78] L. Dunn,[146] U. Dupletsa,[55]
D. D'Urso,[182,147] H. Duval,[193] P.-A. Duverne,[51] S. E. Dwyer,[21] C. Eassa,[21] M. Ebersold,[194,44]
T. Eckhardt,[92] G. Eddolls,[42] B. Edelman,[84] T. B. Edo,[19] O. Edy,[138] A. Effler,[74] J. Eichholz,[29]
H. Einsle,[60] M. Eisenmann,[38] R. A. Eisenstein,[46] A. Ejlli,[36] M. Emma,[70] E. Engelby,[66] A. J. Engl,[35]
L. Errico,[45,23] R. C. Essick,[195] H. Estellés,[18] D. Estevez,[76] T. Etzel,[19] M. Evans,[46] T. Evstafyeva,[33]
B. E. Ewing,[26] J. M. Ezquiaga,[141] F. Fabrizi,[72,73] F. Faedi,[73,72] V. Fafone,[149,102] S. Fairhurst,[36]
P. C. Fan,[190] A. M. Farah,[141] B. Farr,[84] W. M. Farr,[196,197] G. Favaro,[96] M. Favata,[198] M. Fays,[127]
M. Fazio,[106] J. Feicht,[19] M. M. Fejer,[35] E. Fenyvesi,[89,199] D. L. Ferguson,[164] I. Ferrante,[93,37]
T. A. Ferreira,[28] F. Fidecaro,[93,37] A. Fiori,[37,93] I. Fiori,[68] M. Fishbach,[195] R. P. Fisher,[132]
R. Fittipaldi,[200,121] V. Fiumara,[201,121] R. Flaminio,[44] S. M. Fleischer,[202] L. S. Fleming,[203] E. Floden,[105]
E. M. Foley,[105] H. Fong,[155] J. A. Font,[152,153] B. Fornal,[204] P. W. F. Forsyth,[29] K. Franceschetti,[185]
N. Franchini,[78] S. Frasca,[123,75] F. Frasconi,[37] A. Frattale Mascioli,[123,75] Z. Frei,[205] A. Freise,[48,115]
O. Freitas,[206,152] R. Frey,[84] W. Frischhertz,[74] P. Fritschel,[46] V. V. Frolov,[74] G. G. Fronzé,[41]
M. Fuentes-Garcia,[19] S. Fujii,[169] I. Fukunaga,[207] P. Fulda,[56] M. Fyffe,[74] W. E. Gabella,[208] B. Gadre,[83]
J. R. Gair,[18] S. Galaudage,[25,209] S. Gallardo,[210] B. Gallego,[210] R. Gamba,[109] A. Gamboa,[18]
D. Ganapathy,[46] A. Ganguly,[32] S. G. Gaonkar,[32] B. Garaventa,[67,142] J. Garcia-Bellido,[128]
C. García-Núñez,[203] C. García-Quirós,[194] J. W. Gardner,[29] K. A. Gardner,[155] J. Gargiulo,[68]
A. Garron,[107] F. Garufi,[45,23] C. Gasbarra,[149,102] B. Gateley,[21] V. Gayathri,[27] G. Gemme,[67]
A. Gennai,[37] J. George,[111] R. George,[164] O. Gerberding,[92] L. Gergely,[211] N. Ghadiri,[66]
Archisman Ghosh,[100] Shaon Ghosh,[198] Shrobana Ghosh,[30,31] Suprovo Ghosh,[32] Tathagata Ghosh,[32]
L. Giacoppo,[123,75] J. A. Giaime,[28,74] K. D. Giardina,[74] D. R. Gibson,[203] D. T. Gibson,[33] C. Gier,[106]
P. Giri,[37,93] F. Gissi,[103] S. Gkaitatzis,[93,37] J. Glanzer,[28] A. E. Gleckl,[66] F. Glotin,[51] J. Godfrey,[84]
P. Godwin,[19] N. L. Goebbels,[92] E. Goetz,[155] J. Golomb,[19] S. Gomez Lopez,[123,75] B. Goncharov,[55]
G. González,[28] P. Goodarzi,[143] A. W. Goodwin-Jones,[43] M. Gosselin,[68] A. S. Göttel,[36] R. Gouaty,[44]

D. W. Gould,[29] S. Goyal,[91] B. Grace,[29] A. Grado,[212,23] V. Graham,[42] A. E. Granados,[105]
M. Granata,[184] V. Granata,[77] L. Granda Argianas,[110] S. Gras,[46] P. Grassia,[19] C. Gray,[21] R. Gray,[42]
G. Greco,[62] A. C. Green,[48,115] S. M. Green,[138] S. R. Green,[18] A. M. Gretarsson,[59] E. M. Gretarsson,[59]
D. Griffith,[19] W. L. Griffiths,[36] H. L. Griggs,[69] G. Grignani,[94,62] A. Grimaldi,[118,119] C. Grimaud,[44]
H. Grote,[36] A. S. Gruson,[66] D. Guerra,[152] D. Guetta,[213,75] G. M. Guidi,[72,73] A. R. Guimaraes,[28]
H. K. Gulati,[99] F. Gulminelli,[214,215] A. M. Gunny,[46] H. Guo,[204] W. Guo,[43] Y. Guo,[48,47]
Anchal Gupta,[19] Anuradha Gupta,[216] Ish Gupta,[26] N. C. Gupta,[99] P. Gupta,[48,83] S. K. Gupta,[56]
T. Gupta,[98] N. Gupte,[18] R. Gurav,[143] J. Gurs,[92] N. Gutierrez,[184] F. Guzman,[145] D. Haba,[20] M. Haberland,[18]
L. Haegel,[78] G. Hain,[132] S. Haino,[217] E. D. Hall,[46] E. Z. Hamilton,[194] G. Hammond,[42] W.-B. Han,[218]
M. Haney,[194,48] J. Hanks,[21] C. Hanna,[26] M. D. Hannam,[36] O. A. Hannuksela,[154] A. G. Hanselman,[141]
H. Hansen,[21] J. Hanson,[74] R. Harada,[52] T. Harder,[60] K. Haris,[48,83] T. Harmark,[148] J. Harms,[55,129]
G. M. Harry,[219] I. W. Harry,[138] B. Haskell,[101] C.-J. Haster,[220] J. S. Hathaway,[221] K. Haughian,[42]
H. Hayakawa,[61] K. Hayama,[222] J. Healy,[221] A. Heffernan,[107] A. Heidmann,[130] M. C. Heintze,[74]
J. Heinze,[126] J. Heinzel,[46] H. Heitmann,[60] F. Hellman,[223] P. Hello,[51] A. F. Helmling-Cornell,[84]
G. Hemming,[68] M. Hendry,[42] I. S. Heng,[42] E. Hennes,[48] J.-S. Hennig,[47,48] M. Hennig,[47,48] C. Henshaw,[69]
A. Hernandez,[198] T. Hertog,[117] M. Heurs,[30,31] A. L. Hewitt,[33,224] S. Higginbotham,[36] S. Hild,[47,48] P. Hill,[106]
S. Hill,[42] Y. Himemoto,[225] A. S. Hines,[145] N. Hirata,[38] C. Hirose,[226] J. Ho,[159] S. Hoang,[51] S. Hochheim,[30,31]
D. Hofman,[184] N. A. Holland,[48,115] K. Holley-Bockelmann,[208] I. J. Hollows,[183] Z. J. Holmes,[104]
D. E. Holz,[141] C. Hong,[35] J. Hornung,[84] S. Hoshino,[226] J. Hough,[42] S. Hourihane,[19] E. J. Howell,[43]
C. G. Hoy,[138] D. Hoyland,[126] C. A. Hrishikesh,[149] H.-F. Hsieh,[158] C. Hsiung,[227] H. C. Hsu,[159] S.-C. Hsu,[64,158]
W.-F. Hsu,[117] P. Hu,[208] Q. Hu,[42] H. Y. Huang,[159] Y.-J. Huang,[26] Y. Huang,[46] Y. T. Huang,[64]
A. D. Huddart,[228] B. Hughey,[59] D. C. Y. Hui,[229] V. Hui,[44] R. Hur,[84] S. Husa,[107] R. Huxford,[26]
T. Huynh-Dinh,[74] A. Iakovlev,[230] G. A. Iandolo,[47] A. Iess,[180,37] K. Inayoshi,[231] Y. Inoue,[159] G. Iorio,[96]
J. Irwin,[42] M. Isi,[196,197] M. A. Ismail,[159] Y. Itoh,[207,232] M. Iwaya,[169] B. R. Iyer,[91]
V. JaberianHamedan,[43] P.-E. Jacquet,[130] S. J. Jadhav,[233] S. P. Jadhav,[172] T. Jain,[33] A. L. James,[36]
P. A. James,[132] R. Jamshidi,[49] A. Z. Jan,[164] K. Jani,[208] L. Janiurek,[42] J. Janquart,[83,48] K. Janssens,[122,60]
N. N. Janthalur,[233] S. Jaraba,[128] P. Jaranowski,[234] P. Jasal,[53] R. Jaume,[107] W. Javed,[36] A. Jennings,[21]
W. Jia,[46] J. Jiang,[56] H.-B. Jin,[235,236] K. Johansmeyer,[198] G. R. Johns,[132] N. A. Johnson,[56] R. Johnston,[42]
N. Johny,[30,31] D. H. Jones,[29] D. I. Jones,[237] R. Jones,[42] S. Jose,[189] P. Joshi,[26] L. Ju,[43] K. Jung,[238]
J. Junker,[30,31] V. Juste,[76] T. Kajita,[239] C. Kalaghatgi,[83,48,240] V. Kalogera,[86] M. Kamiizumi,[61]
N. Kanda,[232,207] S. Kandhasamy,[32] G. Kang,[241] J. B. Kanner,[19] S. J. Kapadia,[32] D. P. Kapasi,[29]
S. Karat,[19] C. Karathanasis,[54] S. Karki,[113] R. Kashyap,[26] M. Kasprzack,[19] W. Kastaun,[30,31] J. Kato,[168]
T. Kato,[169] S. Katsanevas,[68,*] E. Katsavounidis,[46] W. Katzman,[74] T. Kaur,[43] R. Kaushik,[111] K. Kawabe,[21]
D. Keitel,[107] J. Kelley-Derzon,[56] J. Kennington,[26] R. Kesharwani,[32] J. S. Key,[242] S. Khadka,[35]
F. Y. Khalili,[116] F. Khan,[30,31] I. Khan,[243,50] T. Khanam,[175] E. A. Khazanov,[230] M. Khursheed,[111]
W. Kiendrebeogo,[60,244] N. Kijbunchoo,[104] C. Kim,[245] J. C. Kim,[246] K. Kim,[247] M. H. Kim,[248] S. Kim,[229]
W. S. Kim,[249] Y.-M. Kim,[247] C. Kimball,[86] N. Kimura,[61] M. Kinley-Hanlon,[42] M. Kinnear,[36]
J. S. Kissel,[21] T. Kiyota,[207] S. Klimenko,[56] T. Klinger,[36] A. M. Knee,[155] N. Knust,[30,31] P. Koch,[30,31]
S. M. Koehlenbeck,[35] G. Koekoek,[48,47] K. Kohri,[250] K. Kokeyama,[36] S. Koley,[55] P. Kolitsidou,[126]
M. Kolstein,[54] K. Komori,[52] A. K. H. Kong,[158] A. Kontos,[251] M. Korobko,[92] R. V. Kossak,[30,31]
X. Kou,[105] A. Koushik,[122] N. Kouvatsos,[79] M. Kovalam,[43] N. Koyama,[226] D. B. Kozak,[19] S. L. Kranzhoff,[47,48]
V. Kringel,[30,31] N. V. Krishnendu,[91] A. Królak,[252,191] G. Kuehn,[30,31] P. Kuijer,[48] S. Kulkarni,[216]
A. Kulur Ramamohan,[29] A. Kumar,[233] Praveen Kumar,[140] Prayush Kumar,[91] Rahul Kumar,[21]
Rakesh Kumar,[99] J. Kume,[52] K. Kuns,[46] S. Kuroyanagi,[128,253] S. Kuwahara,[52] K. Kwak,[238] K. Kwan,[29]
G. Lacaille,[42] P. Lagabbe,[44] D. Laghi,[137] S. Lai,[162] A. H. Laity,[177] M. H. Lakkis,[49] E. Lalande,[254]
M. Lalleman,[122] M. Landry,[21] B. B. Lane,[46] R. N. Lang,[46] J. Lange,[164] B. Lantz,[35] A. La Rana,[75]
I. La Rosa,[107,123,44] A. Lartaux-Vollard,[51] P. D. Lasky,[25] J. Lawrence,[175] M. Laxen,[74] A. Lazzarini,[19]
C. Lazzaro,[96,97] P. Leaci,[123,75] S. LeBohec,[204] Y. K. Lecoeuche,[155] H. M. Lee,[246] H. W. Lee,[255]
K. Lee,[248] R.-K. Lee,[158] R. Lee,[46] S. Lee,[247] Y. Lee,[159] I. N. Legred,[19] J. Lehmann,[30,31] L. Lehner,[187]
A. Lemaître,[256] M. Lenti,[73,257] M. Leonardi,[258,38] E. Leonova,[112] M. Lequime,[50] N. Leroy,[51]
M. Lesovsky,[19] N. Letendre,[44] M. Lethuillier,[170] C. Levesque,[254] Y. Levin,[25] K. Leyde,[78] A. K. Y. Li,[19]
K. L. Li,[157] T. G. F. Li,[154,117] X. Li,[165] Chien-Yu Lin,[159,158] Chun-Yu Lin,[259] E. T. Lin,[158] F. Lin,[159]
H. Lin,[159] L. C.-C. Lin,[157] F. Linde,[240,48] S. D. Linker,[150,210] T. B. Littenberg,[260] A. Liu,[154] G. C. Liu,[227]
Jian Liu,[43] F. Llamas,[178] J. Llobera-Querol,[107] R. K. L. Lo,[19] J.-P. Locquet,[117] L. London,[112]
A. Longo,[72,73] D. Lopez,[194] M. Lopez Portilla,[83] M. Lorenzini,[149,102] V. Loriette,[51] M. Lormand,[74]

G. Losurdo,[37] T. P. Lott IV,[69] J. D. Lough,[30, 31] H. A. Loughlin,[46] C. O. Lousto,[221] M. J. Lowry,[132]
H. Lück,[31, 30, 31] D. Lumaca,[102] A. P. Lundgren,[138] A. W. Lussier,[254] L.-T. Ma,[158] S. Ma,[165] M. Ma'arif,[159]
R. Macas,[138] M. MacInnis,[46] R. R. Maciy,[30, 31] D. M. Macleod,[36] I. A. O. MacMillan,[19] A. Macquet,[54]
D. Macri,[46] K. Maeda,[168] S. Maenaut,[117] I. Magaña Hernandez,[27] S. S. Magare,[32] C. Magazzù,[37]
R. M. Magee,[19] E. Maggio,[18] R. Maggiore,[48, 115] M. Magnozzi,[67, 142] M. Mahesh,[92] S. Mahesh,[261] M. Maini,[177]
S. Majhi,[32] E. Majorana,[123, 75] C. N. Makarem,[19] J. A. Malaquias-Reis,[34] S. Maliakal,[19] A. Malik,[111] N. Man,[60]
V. Mandic,[105] V. Mangano,[75, 123] B. Mannix,[84] G. L. Mansell,[85, 46] M. Manske,[27] M. Mantovani,[68]
M. Mapelli,[96, 97] F. Marchesoni,[63, 62, 262] D. Marín Pina,[53, 87, 263] F. Marion,[44] S. Márka,[176] Z. Márka,[176]
C. Markakis,[161] A. S. Markosyan,[35] A. Markowitz,[19] E. Maros,[19] A. Marquina,[174] S. Marsat,[137]
F. Martelli,[72, 73] I. W. Martin,[42] R. M. Martin,[198] B. B. Martinez,[145] M. Martinez,[54, 264] V. Martinez,[139]
A. Martini,[118] K. Martinovic,[79] J. C. Martins,[34] D. V. Martynov,[126] E. J. Marx,[46] L. Massaro,[47, 48]
A. Masserot,[44] M. Masso-Reid,[42] M. Mastrodicasa,[75] S. Mastrogiovanni,[75] M. Mateu-Lucena,[107]
M. Matiushechkina,[30, 31] M. Matsuyama,[207] N. Mavalvala,[46] N. Maxwell,[21] G. McCarrol,[74] R. McCarthy,[21]
D. E. McClelland,[29] S. McCormick,[74] L. McCuller,[19] G. I. McGhee,[42] K. B. M. McGowan,[208]
M. Mchedlidze,[198] C. McIsaac,[138] J. McIver,[155] K. McKinney,[179] A. McLeod,[43] T. McRae,[29]
S. T. McWilliams,[261] D. Meacher,[27] A. K. Mehta,[18] Q. Meijer,[83] A. Melatos,[146] S. Mellaerts,[117]
A. Menendez-Vazquez,[54] C. S. Menoni,[114] R. A. Mercer,[27] L. Mereni,[184] K. Merfeld,[84] E. L. Merilh,[74]
J. R. Mérou,[107] J. D. Merritt,[84] M. Merzougui,[60] C. Messenger,[42] C. Messick,[27] M. Meyer-Conde,[207]
F. Meylahn,[30, 31] A. Mhaske,[32] A. Miani,[118, 119] H. Miao,[265] I. Michaloliakos,[56] C. Michel,[184]
Y. Michimura,[19, 52] H. Middleton,[126] A. L. Miller,[48] S. Miller,[19] M. Millhouse,[69] E. Milotti,[266, 58]
Y. Minenkov,[102] N. Mio,[267] Ll. M. Mir,[54] L. Mirasola,[268, 75] M. Miravet-Tenés,[152] C.-A. Miritescu,[54]
A. K. Mishra,[91] A. Mishra,[32] C. Mishra,[189] T. Mishra,[56] A. L. Mitchell,[48, 115] J. G. Mitchell,[59] S. Mitra,[32]
V. P. Mitrofanov,[116] G. Mitselmakher,[56] R. Mittleman,[46] O. Miyakawa,[61] S. Miyamoto,[169] S. Miyoki,[61]
G. Mo,[46] L. Mobilia,[72, 73] L. M. Modafferi,[107] S. R. P. Mohapatra,[19] S. R. Mohite,[27] M. Molina-Ruiz,[223]
C. Mondal,[214] M. Mondin,[210] M. Montani,[72, 73] C. J. Moore,[126] M. Morales,[66] D. Moraru,[21] F. Morawski,[101]
A. More,[32] S. More,[32] C. Moreno,[59] G. Moreno,[21] S. Morisaki,[52, 169] Y. Moriwaki,[168] G. Morras,[128]
A. Moscatello,[96] P. Mourier,[107] B. Mours,[76] C. M. Mow-Lowry,[48, 115] S. Mozzon,[138]
F. Muciaccia,[123, 75] D. Mukherjee,[260] Samanwaya Mukherjee,[32] Soma Mukherjee,[178] Subroto Mukherjee,[99]
Suvodip Mukherjee,[269, 187, 112] N. Mukund,[46] A. Mullavey,[74] J. Munch,[104] C. L. Mungioli,[43] M. Munn,[21]
W. R. Munn Oberg,[270] M. Murakoshi,[271] P. G. Murray,[42] S. Muusse,[29] S. L. Nadji,[30, 31] A. Nagar,[41, 272]
N. Nagarajan,[42] K. N. Nagler,[59] K. Nakamura,[38] H. Nakano,[273] M. Nakano,[19] D. Nandi,[28] V. Napolano,[68]
P. Narayan,[216] I. Nardecchia,[149, 102] H. Narola,[83] L. Naticchioni,[75] R. K. Nayak,[274] B. F. Neil,[43]
J. Neilson,[103, 121] A. Nelson,[145] T. J. N. Nelson,[74] M. Nery,[30, 31] A. Neunzert,[21] S. Ng,[66] C. Nguyen,[78]
P. Nguyen,[84] L. Nguyen Quynh,[275] S. A. Nichols,[28] A. B. Nielsen,[276] G. Nieradka,[101] A. Niko,[159]
Y. Nishino,[38, 277] A. Nishizawa,[52] S. Nissanke,[112, 48] E. Nitoglia,[170] W. Niu,[26] F. Nocera,[68] M. Norman,[36]
C. North,[36] J. Novak,[124, 278, 279, 280] J. F. Nuño Siles,[128] G. Nurbek,[178] L. K. Nuttall,[138] K. Obayashi,[271]
J. Oberling,[21] J. O'Dell,[228] M. Oertel,[124, 278, 279, 281, 280] A. Offermans,[117] G. Oganesyan,[55, 129] J. J. Oh,[249]
K. Oh,[229] S. H. Oh,[249] T. O'Hanlon,[74] M. Ohashi,[61] M. Ohkawa,[226] F. Ohme,[30, 31] H. Ohta,[52]
A. S. Oliveira,[176] R. Oliveri,[124, 278, 279] V. Oloworaran,[43] B. O'Neal,[132] K. Oohara,[282, 283] B. O'Reilly,[74]
N. D. Ormsby,[132] M. Orselli,[62, 94] R. O'Shaughnessy,[221] Y. Oshima,[284] S. Oshino,[61] S. Ossokine,[18]
C. Osthelder,[19] D. J. Ottaway,[104] A. Ouzriat,[170] H. Overmier,[74] B. J. Owen,[175] A. E. Pace,[26] R. Pagano,[28]
M. A. Page,[38] A. Pai,[156] S. A. Pai,[111] A. Pal,[285] S. Pal,[274] M. A. Palaia,[37, 93] O. Palashov,[230] M. Pálfi,[205]
P. P. Palma,[149, 102] C. Palomba,[75] K. C. Pan,[158] P. K. Panda,[233] L. Panebianco,[72, 73] P. T. H. Pang,[48, 83]
F. Pannarale,[123, 75] B. C. Pant,[111] F. H. Panther,[43] C. D. Panzer,[105] F. Paoletti,[37] A. Paoli,[68]
A. Paolone,[75, 286] E. E. Papalexakis,[143] L. Papalini,[37, 93] G. Papigkiotis,[287] A. Parisi,[48, 112] J. Park,[247]
W. Parker,[74] G. Pascale,[30, 31] D. Pascucci,[100] A. Pasqualetti,[68] R. Passaquieti,[93, 37] D. Passuello,[37]
O. Patane,[21] M. Patel,[132] D. Pathak,[32] M. Pathak,[104] A. Patra,[36] B. Patricelli,[93, 37] A. S. Patron,[28]
S. Paul,[84] E. Payne,[19] T. Pearce,[36] M. Pedraza,[19] R. Pegna,[37] A. Pele,[19] F. E. Peña Arellano,[61]
S. Penn,[270] M. D. Penuliar,[66] A. Perego,[118, 119] A. Pereira,[139] J. J. Perez,[56] C. Périgois,[171, 97, 96]
C. C. Perkins,[56] G. Perna,[96] A. Perreca,[118, 119] J. Perret,[78] S. Perriès,[170] J. W. Perry,[48, 115] D. Pesios,[287]
C. Petrillo,[94] H. P. Pfeiffer,[18] H. Pham,[74] K. A. Pham,[105] K. S. Phukon,[126, 48, 240] H. Phurailatpam,[154]
O. J. Piccinni,[54] M. Pichot,[60] M. Piendibene,[93, 37] F. Piergiovanni,[72, 73] L. Pierini,[75] G. Pierra,[170]
V. Pierro,[103, 121] M. Pietrzak,[101] M. Pillas,[51] F. Pilo,[37] L. Pinard,[184] C. Pineda-Bosque,[210]
I. M. Pinto,[103, 121, 288, 45] M. Pinto,[68] B. J. Piotrzkowski,[27] M. Pirello,[21] M. D. Pitkin,[33, 224]
A. Placidi,[62, 94] E. Placidi,[123, 75] M. L. Planas,[107] W. Plastino,[289, 290] R. Poggiani,[93, 37] E. Polini,[44]
L. Pompili,[18] J. Poon,[154] E. Porcelli,[48] J. Portell,[53, 87, 263] E. K. Porter,[78] C. Posnansky,[26] R. Poulton,[68]

J. Powell,[172] M. Pracchia,[44] B. K. Pradhan,[32] T. Pradier,[76] A. K. Prajapati,[99] K. Prasai,[35] R. Prasanna,[233]
P. Prasia,[32] G. Pratten,[126] M. Principe,[150,103,288,121] G. A. Prodi,[291,119] L. Prokhorov,[126] P. Prosposito,[149,102]
L. Prudenzi,[18] A. Puecher,[48,83] J. Pullin,[28] M. Punturo,[62] F. Puosi,[37,93] P. Puppo,[75] M. Pürrer,[177]
H. Qi,[161] J. Qin,[29] G. Quéméner,[215,124,214] V. Quetschke,[178] C. Quigley,[36] P. J. Quinonez,[59]
R. Quitzow-James,[113] F. J. Raab,[21] G. Raaijmakers,[112,48] N. Radulesco,[60] P. Raffai,[205] S. X. Rail,[254]
S. Raja,[111] C. Rajan,[111] B. Rajbhandari,[221,175] D. S. Ramirez,[59] K. E. Ramirez,[74] F. A. Ramis Vidal,[107]
A. Ramos-Buades,[18] D. Rana,[32] E. Randel,[114] S. Ranjan,[69] P. Rapagnani,[123,75] B. Ratto,[59] S. Rawat,[105]
A. Ray,[27] V. Raymond,[36] M. Razzano,[93,37] J. Read,[66] M. Recaman Payo,[117] T. Regimbau,[44] L. Rei,[67]
S. Reid,[106] S. W. Reid,[132] D. H. Reitze,[19] P. Relton,[36] A. Renzini,[19] P. Rettegno,[41] B. Revenu,[78,292]
A. Reza,[48] M. Rezac,[66] A. S. Rezaei,[75,123] F. Ricci,[123,75] M. Ricci,[75] D. Richards,[228] C. J. Richardson,[59]
J. W. Richardson,[143] A. Rijal,[59] K. Riles,[95] H. K. Riley,[36] S. Rinaldi,[93,37] J. Rittmeyer,[92]
C. Robertson,[228] F. Robinet,[51] M. Robinson,[21] A. Rocchi,[102] L. Rolland,[44] J. G. Rollins,[19]
M. Romanelli,[125] A. E. Romano,[293] R. Romano,[22,23] A. Romero,[193] I. M. Romero-Shaw,[33] J. H. Romie,[74]
T. J. Roocke,[104] L. Rosa,[23,45] T. J. Rosauer,[143] C. A. Rose,[27] D. Rosińska,[133] M. P. Ross,[64]
M. Rossello,[107] S. Rowan,[42] S. K. Roy,[196,197] S. Roy,[83] D. Rozza,[182,147] P. Ruggi,[68] E. Ruiz Morales,[294,128]
K. Ruiz-Rocha,[208] S. Sachdev,[69] T. Sadecki,[21] J. Sadiq,[140] P. Saffarieh,[48,115] M. R. Sah,[269] S. S. Saha,[158]
T. Sainrat,[76] S. Sajith Menon,[213,123,75] K. Sakai,[295] M. Sakellariadou,[79] T. Sako,[168] S. Sakon,[26]
O. S. Salafia,[173,136,135] F. Salces-Carcoba,[19] L. Salconi,[68] M. Saleem,[105] F. Salemi,[123,75] M. Sallé,[48]
S. Salvador,[215,214,124] A. Sanchez,[21] E. J. Sanchez,[19] J. H. Sanchez,[86] L. E. Sanchez,[19]
N. Sanchis-Gual,[296,152] J. R. Sanders,[297] E. M. Sänger,[18] T. R. Saravanan,[32] N. Sarin,[25] A. Sasli,[287]
P. Sassi,[62,94] B. Sassolas,[184] H. Satari,[43] R. Sato,[226] S. Sato,[168] Y. Sato,[168] O. Sauter,[56] R. L. Savage,[21]
T. Sawada,[61] H. L. Sawant,[32] S. Sayah,[44] D. Schaetzl,[19] M. Scheel,[165] J. Scheuer,[86] M. G. Schiworski,[104]
P. Schmidt,[126] S. Schmidt,[83] R. Schnabel,[92] M. Schneewind,[30,31] R. M. S. Schofield,[84] K. Schouteden,[117]
H. Schuler,[26] B. W. Schulte,[30,31] B. F. Schutz,[36,30,31] E. Schwartz,[36] J. Scott,[42] S. M. Scott,[29]
T. C. Seetharamu,[42] M. Seglar-Arroyo,[54] Y. Sekiguchi,[298] D. Sellers,[74] A. S. Sengupta,[299] D. Sentenac,[68]
E. G. Seo,[42] J. W. Seo,[117] V. Sequino,[45,23] A. Sergeev,[230] M. Serra,[75] G. Servignat,[278] Y. Setyawati,[83]
T. Shaffer,[21] U. S. Shah,[69] M. S. Shahriar,[86] M. A. Shaikh,[246] B. Shams,[204] L. Shao,[231] A. K. Sharma,[91]
P. Sharma,[111] S. Sharma-Chaudhary,[113] P. Shawhan,[134] N. S. Shcheblanov,[300,256] B. Shen,[134]
Y. Shikano,[301,302] M. Shikauchi,[52] K. Shimode,[61] H. Shinkai,[303] J. Shiota,[271] D. H. Shoemaker,[46]
D. M. Shoemaker,[164] R. W. Short,[21] S. ShyamSundar,[111] A. Sider,[49] H. Siegel,[176,196,197] M. Sieniawska,[131]
D. Sigg,[21] L. Silenzi,[62,63] M. Simmonds,[104] L. P. Singer,[90] A. Singh,[216] D. Singh,[26] M. K. Singh,[91]
A. Singha,[47,48] A. M. Sintes,[107] V. Sipala,[182,147] V. Skliris,[36] B. J. J. Slagmolen,[29] T. J. Slaven-Blair,[43]
J. Smetana,[126] J. R. Smith,[66] L. Smith,[42] R. J. E. Smith,[25] W. J. Smith,[208] J. Soldateschi,[257,304,73]
S. N. Somala,[305] K. Somiya,[20] K. Soni,[32] S. Soni,[46] V. Sordini,[170] F. Sorrentino,[67] N. Sorrentino,[93,37]
R. Soulard,[60] T. Souradeep,[32,306] A. Southgate,[36] E. Sowell,[175] V. Spagnuolo,[47,48] A. P. Spencer,[42]
M. Spera,[96,97] P. Spinicelli,[68] A. K. Srivastava,[99] F. Stachurski,[42] D. A. Steer,[78] J. Steinlechner,[47,48]
S. Steinlechner,[47,48] N. Stergioulas,[287] P. Stevens,[51] M. StPierre,[177] L. C. Strang,[146]
G. Stratta,[307,308,75,309] M. D. Strong,[28] A. Strunk,[21] R. Sturani,[310] A. L. Stuver,[110] M. Suchenek,[101]
S. Sudhagar,[32,101] N. Sueltmann,[92] A. G. Sullivan,[176] K. D. Sullivan,[28] L. Sun,[29] S. Sunil,[99] A. Sur,[101]
J. Suresh,[52,131] P. J. Sutton,[36] Takamasa Suzuki,[226] Takanori Suzuki,[20] B. L. Swinkels,[48] A. Syx,[76]
M. J. Szczepańczyk,[56] P. Szewczyk,[133] M. Tacca,[48] H. Tagoshi,[169] S. C. Tait,[42] H. Takahashi,[311]
R. Takahashi,[38] A. Takamori,[65] K. Takatani,[207] H. Takeda,[312] M. Takeda,[207] C. J. Talbot,[106] C. Talbot,[46]
M. Tamaki,[169] N. Tamanini,[137] D. Tanabe,[159] K. Tanaka,[313] S. J. Tanaka,[271] T. Tanaka,[312]
A. J. Tanasijczuk,[131] D. Tang,[43] S. Tanioka,[85] D. B. Tanner,[56] L. Tao,[56] R. D. Tapia,[26]
E. N. Tapia San Martín,[48] R. Tarafder,[19] C. Taranto,[149,102] A. Taruya,[314] J. D. Tasson,[190] M. Teloi,[49]
R. Tenorio,[107] H. Themann,[210] A. Theodoropoulos,[152] M. P. Thirugnanasambandam,[32] L. M. Thomas,[126]
M. Thomas,[74] P. Thomas,[21] J. E. Thompson,[165] S. R. Thondapu,[111] K. A. Thorne,[74] E. Thrane,[25] J. Tissino,[55]
A. Tiwari,[32] Shubhanshu Tiwari,[194] Srishti Tiwari,[32] V. Tiwari,[126] M. R. Todd,[85] A. M. Toivonen,[105]
K. Toland,[42] A. E. Tolley,[138] T. Tomaru,[38] K. Tomita,[207] T. Tomura,[61] C. Tong-Yu,[159] A. Toriyama,[271]
N. Toropov,[126] A. Torres-Forné,[152,153] C. I. Torrie,[19] M. Toscani,[137] I. Tosta e Melo,[315]
E. Tournefier,[44] A. A. Trani,[52] A. Trapananti,[63,62] F. Travasso,[63,62] G. Traylor,[74] J. Trenado,[53]
M. Trevor,[134] M. C. Tringali,[68] A. Tripathee,[95] L. Troiano,[316,121] A. Trovato,[58,266] L. Trozzo,[23]
R. J. Trudeau,[19] T. T. L. Tsang,[36] R. Tso,[165,†] S. Tsuchida,[317] L. Tsukada,[26] T. Tsutsui,[52]
K. Turbang,[193,122] M. Turconi,[60] C. Turski,[100] H. Ubach,[53,87] A. S. Ubhi,[126] N. Uchikata,[169]
T. Uchiyama,[61] R. P. Udall,[19] T. Uehara,[318] K. Ueno,[52] C. S. Unnikrishnan,[269] T. Ushiba,[61]

A. Utina,[47,48] M. Vacatello,[37,93] H. Vahlbruch,[30,31] N. Vaidya,[19] G. Vajente,[19] A. Vajpeyi,[25]
G. Valdes,[145] J. Valencia,[107] M. Valentini,[115,48] S. A. Vallejo-Peña,[293] S. Vallero,[41] V. Valsan,[27]
N. van Bakel,[48] M. van Beuzekom,[48] M. van Dael,[48,319] J. F. J. van den Brand,[47,115,48]
C. Van Den Broeck,[83,48] D. C. Vander-Hyde,[85] M. van der Sluys,[48,83] A. Van de Walle,[51]
J. van Dongen,[48,115] K. Vandra,[110] H. van Haevermaet,[122] J. V. van Heijningen,[131] J. Vanosky,[19]
M. H. P. M. van Putten,[320] Z. van Ranst,[47,48] N. van Remortel,[122] M. Vardaro,[47,48] A. F. Vargas,[146]
V. Varma,[18] M. Vasúth,[89] A. Vecchio,[126] G. Vedovato,[97] J. Veitch,[42] P. J. Veitch,[104]
S. Venikoudis,[131] J. Venneberg,[30,31] P. Verdier,[170] D. Verkindt,[44] B. Verma,[151] P. Verma,[191]
Y. Verma,[111] S. M. Vermeulen,[19] D. Veske,[176] F. Vetrano,[72] A. Veutro,[75] A. M. Vibhute,[21]
A. Viceré,[72,73] S. Vidyant,[85] A. D. Viets,[321] A. Vijaykumar,[91] A. Vilkha,[221] V. Villa-Ortega,[140]
E. T. Vincent,[69] J.-Y. Vinet,[60] S. Viret,[170] A. Virtuoso,[266,58] S. Vitale,[46] H. Vocca,[94,62] D. Voigt,[92]
E. R. G. von Reis,[21] J. S. A. von Wrangel,[30,31] S. P. Vyatchanin,[116] L. E. Wade,[82] M. Wade,[82]
K. J. Wagner,[221] R. C. Walet,[48] M. Walker,[132] G. S. Wallace,[106] L. Wallace,[19] H. Wang,[284] J. Z. Wang,[95]
W. H. Wang,[178] Z. Wang,[159] G. Waratkar,[156] R. L. Ward,[29] J. Warner,[21] M. Was,[44] T. Washimi,[38]
N. Y. Washington,[19] D. Watarai,[52] K. E. Wayt,[82] B. Weaver,[21] C. R. Weaving,[138] S. A. Webster,[42]
M. Weinert,[30,31] A. J. Weinstein,[19] R. Weiss,[46] C. M. Weller,[64] R. A. Weller,[208] F. Wellmann,[30,31]
L. Wen,[43] P. Wessels,[30,31] K. Wette,[29] J. T. Whelan,[221] D. D. White,[66] B. F. Whiting,[56] C. Whittle,[46]
J. B. Wildberger,[18] O. S. Wilk,[82] D. Wilken,[30,31,31] K. Willetts,[36] D. Williams,[42] M. J. Williams,[42]
N. S. Williams,[126] J. L. Willis,[19] B. Willke,[31,30,31] M. Wils,[117] C. C. Wipf,[19] G. Woan,[42] J. Woehler,[47,48]
J. K. Wofford,[221] N. E. Wolfe,[46] D. Wong,[155] H. T. Wong,[159] H. W. Y. Wong,[154] I. C. F. Wong,[154]
J. L. Wright,[29] M. Wright,[42] C. Wu,[158] D. S. Wu,[30,31] H. Wu,[158] D. M. Wysocki,[27] L. Xiao,[19]
V. A. Xu,[46] Y. Xu,[194] N. Yadav,[101] H. Yamamoto,[19] K. Yamamoto,[168] M. Yamamoto,[168]
T. S. Yamamoto,[253] T. Yamamoto,[61] S. Yamamura,[169] R. Yamazaki,[271] S. Yan,[35] T. Yan,[126] F. W. Yang,[204]
F. Yang,[176] K. Z. Yang,[105] L.-C. Yang,[162] Y. Yang,[162] Z. Yarbrough,[28] S.-W. Yeh,[158] A. B. Yelikar,[221]
S. M. C. Yeung,[27] X. Yin,[46] J. Yokoyama,[52] T. Yokozawa,[61] J. Yoo,[166] H. Yu,[165] H. Yuzurihara,[61]
A. Zadrożny,[191] A. J. Zannelli,[132] M. Zanolin,[59] M. Zeeshan,[221] T. Zelenova,[68] J.-P. Zendri,[97] M. Zeoli,[127,131]
M. Zerrad,[50,243] M. Zevin,[86] A. C. Zhang,[176] J. Zhang,[29] L. Zhang,[19] R. Zhang,[56] T. Zhang,[126]
Y. Zhang,[29] C. Zhao,[43] Yue Zhao,[204] Yuhang Zhao,[169,38,78] Y. Zheng,[113] H. Zhong,[105] S. Zhong,[43]
R. Zhou,[223] Z.-H. Zhu,[144,322] A. B. Zimmerman,[164] M. E. Zucker,[46,19] J. Zweizig,[19]

[1] *Department of Astronomy and Astrophysics, The Pennsylvania State University, 525 Davey Lab, University Park, PA 16802, USA*
[2] *Department of Physics and Astronomy, University of Alabama, Tuscaloosa, AL 35487, USA*
[3] *Department of Astronomy & Astrophysics, University of Toronto, Toronto, ON M5S 3H4*
[4] *Dunlap Institute for Astronomy & Astrophysics, University of Toronto, Toronto, ON M5S 3H4*
[5] *Astrophysics Science Division, NASA Goddard Space Flight Center, Greenbelt, MD 20771, USA*
[6] *INAF – IASF-Palermo, via Ugo La Malfa 153, 90146 Palermo PA, Italy*
[7] *INAF-Osservatorio Astronomico di Brera, Via E. Bianchi 46, 23807 Merate, LC, Italy*
[8] *Space Science Data Center (SSDC) – Agenzia Spaziale Italiana (ASI), 00133 Roma, Italy*
[9] *INAF – Osservatorio Astronomico di Roma, Via Frascati 33, 00040 Monte Porzio Catone, Italy*
[10] *MIFT Department, Polo Papardo, University of Messina, Viale Ferdinando Stagno d'Alcontres, 31, 98166 Messina, Italy*
[11] *School of Physics and Astronomy, University of Leicester, University Road, Leicester LE1 7RH, UK*
[12] *Department of Physics & Astronomy, Clemson University, Kinard Lab of Physics, Clemson, SC 29634, USA*
[13] *Mullard Space Science Laboratory, University College London, Holmbury St. Mary, Dorking, Surrey RH5 6NT, UK*
[14] *INAF-Osservatorio Astronomico di Roma, Via di Frascati 33, 00040 Monte Porzio Catone, RM, Italy*
[15] *Los Alamos National Laboratory, PO Box 1663, Los Alamos New Mexico 87545*
[16] *INAF - Osservatorio Astronomico di Brera, Via E. Bianchi 46, 23807 Merate, Italy*
[17] *University of Rome Tor Vergata, via Cracovia 50, 00100 Roma, Italy*
[18] *Max Planck Institute for Gravitational Physics (Albert Einstein Institute), D-14476 Potsdam, Germany*
[19] *LIGO Laboratory, California Institute of Technology, Pasadena, CA 91125, USA*
[20] *Graduate School of Science, Tokyo Institute of Technology, 2-12-1 Ookayama, Meguro-ku, Tokyo 152-8551, Japan*
[21] *LIGO Hanford Observatory, Richland, WA 99352, USA*
[22] *Dipartimento di Farmacia, Università di Salerno, I-84084 Fisciano, Salerno, Italy*
[23] *INFN, Sezione di Napoli, I-80126 Napoli, Italy*
[24] *University of Warwick, Coventry CV4 7AL, United Kingdom*
[25] *OzGrav, School of Physics & Astronomy, Monash University, Clayton 3800, Victoria, Australia*
[26] *The Pennsylvania State University, University Park, PA 16802, USA*
[27] *University of Wisconsin-Milwaukee, Milwaukee, WI 53201, USA*

[28]*Louisiana State University, Baton Rouge, LA 70803, USA*
[29]*OzGrav, Australian National University, Canberra, Australian Capital Territory 0200, Australia*
[30]*Max Planck Institute for Gravitational Physics (Albert Einstein Institute), D-30167 Hannover, Germany*
[31]*Leibniz Universität Hannover, D-30167 Hannover, Germany*
[32]*Inter-University Centre for Astronomy and Astrophysics, Pune 411007, India*
[33]*University of Cambridge, Cambridge CB2 1TN, United Kingdom*
[34]*Instituto Nacional de Pesquisas Espaciais, 12227-010 São José dos Campos, São Paulo, Brazil*
[35]*Stanford University, Stanford, CA 94305, USA*
[36]*Cardiff University, Cardiff CF24 3AA, United Kingdom*
[37]*INFN, Sezione di Pisa, I-56127 Pisa, Italy*
[38]*Gravitational Wave Science Project, National Astronomical Observatory of Japan, 2-21-1 Osawa, Mitaka City, Tokyo 181-8588, Japan*
[39]*Advanced Technology Center, National Astronomical Observatory of Japan, 2-21-1 Osawa, Mitaka City, Tokyo 181-8588, Japan*
[40]*Dipartimento di Fisica, Università degli Studi di Torino, I-10125 Torino, Italy*
[41]*INFN Sezione di Torino, I-10125 Torino, Italy*
[42]*SUPA, University of Glasgow, Glasgow G12 8QQ, United Kingdom*
[43]*OzGrav, University of Western Australia, Crawley, Western Australia 6009, Australia*
[44]*Univ. Savoie Mont Blanc, CNRS, Laboratoire d'Annecy de Physique des Particules - IN2P3, F-74000 Annecy, France*
[45]*Università di Napoli "Federico II", I-80126 Napoli, Italy*
[46]*LIGO Laboratory, Massachusetts Institute of Technology, Cambridge, MA 02139, USA*
[47]*Maastricht University, 6200 MD Maastricht, Netherlands*
[48]*Nikhef, 1098 XG Amsterdam, Netherlands*
[49]*Université Libre de Bruxelles, Brussels 1050, Belgium*
[50]*Institut Fresnel, Aix Marseille Université, CNRS, Centrale Marseille, F-13013 Marseille, France*
[51]*Université Paris-Saclay, CNRS/IN2P3, IJCLab, 91405 Orsay, France*
[52]*University of Tokyo, Tokyo, 113-0033, Japan.*
[53]*Institut de Ciències del Cosmos (ICCUB), Universitat de Barcelona (UB), c. Martí i Franquès, 1, 08028 Barcelona, Spain*
[54]*Institut de Física d'Altes Energies (IFAE), The Barcelona Institute of Science and Technology, Campus UAB, E-08193 Bellaterra (Barcelona), Spain*
[55]*Gran Sasso Science Institute (GSSI), I-67100 L'Aquila, Italy*
[56]*University of Florida, Gainesville, FL 32611, USA*
[57]*Dipartimento di Scienze Matematiche, Informatiche e Fisiche, Università di Udine, I-33100 Udine, Italy*
[58]*INFN, Sezione di Trieste, I-34127 Trieste, Italy*
[59]*Embry-Riddle Aeronautical University, Prescott, AZ 86301, USA*
[60]*Université Côte d'Azur, Observatoire de la Côte d'Azur, CNRS, Artemis, F-06304 Nice, France*
[61]*Institute for Cosmic Ray Research, KAGRA Observatory, The University of Tokyo, 238 Higashi-Mozumi, Kamioka-cho, Hida City, Gifu 506-1205, Japan*
[62]*INFN, Sezione di Perugia, I-06123 Perugia, Italy*
[63]*Università di Camerino, I-62032 Camerino, Italy*
[64]*University of Washington, Seattle, WA 98195, USA*
[65]*Earthquake Research Institute, The University of Tokyo, 1-1-1 Yayoi, Bunkyo-ku, Tokyo 113-0032, Japan*
[66]*California State University Fullerton, Fullerton, CA 92831, USA*
[67]*INFN, Sezione di Genova, I-16146 Genova, Italy*
[68]*European Gravitational Observatory (EGO), I-56021 Cascina, Pisa, Italy*
[69]*Georgia Institute of Technology, Atlanta, GA 30332, USA*
[70]*Royal Holloway, University of London, London TW20 0EX, United Kingdom*
[71]*The Graduate University for Advanced Studies (SOKENDAI), 2-21-1 Osawa, Mitaka City, Tokyo 181-8588, Japan*
[72]*Università degli Studi di Urbino "Carlo Bo", I-61029 Urbino, Italy*
[73]*INFN, Sezione di Firenze, I-50019 Sesto Fiorentino, Firenze, Italy*
[74]*LIGO Livingston Observatory, Livingston, LA 70754, USA*
[75]*INFN, Sezione di Roma, I-00185 Roma, Italy*
[76]*Université de Strasbourg, CNRS, IPHC UMR 7178, F-67000 Strasbourg, France*
[77]*Dipartimento di Fisica "E.R. Caianiello", Università di Salerno, I-84084 Fisciano, Salerno, Italy*
[78]*Université Paris Cité, CNRS, Astroparticule et Cosmologie, F-75013 Paris, France*
[79]*King's College London, University of London, London WC2R 2LS, United Kingdom*
[80]*Korea Institute of Science and Technology Information, Daejeon 34141, Republic of Korea*
[81]*Université libre de Bruxelles, 1050 Bruxelles, Belgium*
[82]*Kenyon College, Gambier, OH 43022, USA*

[83]*Institute for Gravitational and Subatomic Physics (GRASP), Utrecht University, 3584 CC Utrecht, Netherlands*
[84]*University of Oregon, Eugene, OR 97403, USA*
[85]*Syracuse University, Syracuse, NY 13244, USA*
[86]*Northwestern University, Evanston, IL 60208, USA*
[87]*Departament de Física Quàntica i Astrofísica (FQA), Universitat de Barcelona (UB), c. Martí i Franqués, 1, 08028 Barcelona, Spain*
[88]*Dipartimento di Medicina, Chirurgia e Odontoiatria "Scuola Medica Salernitana", Università di Salerno, I-84081 Baronissi, Salerno, Italy*
[89]*Wigner RCP, RMKI, H-1121 Budapest, Hungary*
[90]*NASA Goddard Space Flight Center, Greenbelt, MD 20771, USA*
[91]*International Centre for Theoretical Sciences, Tata Institute of Fundamental Research, Bengaluru 560089, India*
[92]*Universität Hamburg, D-22761 Hamburg, Germany*
[93]*Università di Pisa, I-56127 Pisa, Italy*
[94]*Università di Perugia, I-06123 Perugia, Italy*
[95]*University of Michigan, Ann Arbor, MI 48109, USA*
[96]*Università di Padova, Dipartimento di Fisica e Astronomia, I-35131 Padova, Italy*
[97]*INFN, Sezione di Padova, I-35131 Padova, Italy*
[98]*Montana State University, Bozeman, MT 59717, USA*
[99]*Institute for Plasma Research, Bhat, Gandhinagar 382428, India*
[100]*Universiteit Gent, B-9000 Gent, Belgium*
[101]*Nicolaus Copernicus Astronomical Center, Polish Academy of Sciences, 00-716, Warsaw, Poland*
[102]*INFN, Sezione di Roma Tor Vergata, I-00133 Roma, Italy*
[103]*Dipartimento di Ingegneria, Università del Sannio, I-82100 Benevento, Italy*
[104]*OzGrav, University of Adelaide, Adelaide, South Australia 5005, Australia*
[105]*University of Minnesota, Minneapolis, MN 55455, USA*
[106]*SUPA, University of Strathclyde, Glasgow G1 1XQ, United Kingdom*
[107]*IAC3–IEEC, Universitat de les Illes Balears, E-07122 Palma de Mallorca, Spain*
[108]*Departamento de Matemáticas, Universitat Autònoma de Barcelona, 08193 Bellaterra (Barcelona), Spain*
[109]*Theoretisch-Physikalisches Institut, Friedrich-Schiller-Universität Jena, D-07743 Jena, Germany*
[110]*Villanova University, Villanova, PA 19085, USA*
[111]*RRCAT, Indore, Madhya Pradesh 452013, India*
[112]*GRAPPA, Anton Pannekoek Institute for Astronomy and Institute for High-Energy Physics, University of Amsterdam, 1098 XH Amsterdam, Netherlands*
[113]*Missouri University of Science and Technology, Rolla, MO 65409, USA*
[114]*Colorado State University, Fort Collins, CO 80523, USA*
[115]*Department of Physics and Astronomy, Vrije Universiteit Amsterdam, 1081 HV Amsterdam, Netherlands*
[116]*Lomonosov Moscow State University, Moscow 119991, Russia*
[117]*Katholieke Universiteit Leuven, Oude Markt 13, 3000 Leuven, Belgium*
[118]*Università di Trento, Dipartimento di Fisica, I-38123 Povo, Trento, Italy*
[119]*INFN, Trento Institute for Fundamental Physics and Applications, I-38123 Povo, Trento, Italy*
[120]*Bar-Ilan University, Ramat Gan, 5290002, Israel*
[121]*INFN, Sezione di Napoli, Gruppo Collegato di Salerno, I-80126 Napoli, Italy*
[122]*Universiteit Antwerpen, 2000 Antwerpen, Belgium*
[123]*Università di Roma "La Sapienza", I-00185 Roma, Italy*
[124]*Centre national de la recherche scientifique, 75016 Paris, France*
[125]*Univ Rennes, CNRS, Institut FOTON - UMR 6082, F-35000 Rennes, France*
[126]*University of Birmingham, Birmingham B15 2TT, United Kingdom*
[127]*Université de Liège, B-4000 Liège, Belgium*
[128]*Instituto de Fisica Teorica UAM-CSIC, Universidad Autonoma de Madrid, 28049 Madrid, Spain*
[129]*INFN, Laboratori Nazionali del Gran Sasso, I-67100 Assergi, Italy*
[130]*Laboratoire Kastler Brossel, Sorbonne Université, CNRS, ENS-Université PSL, Collège de France, F-75005 Paris, France*
[131]*Université catholique de Louvain, B-1348 Louvain-la-Neuve, Belgium*
[132]*Christopher Newport University, Newport News, VA 23606, USA*
[133]*Astronomical Observatory Warsaw University, 00-478 Warsaw, Poland*
[134]*University of Maryland, College Park, MD 20742, USA*
[135]*Università degli Studi di Milano-Bicocca, I-20126 Milano, Italy*
[136]*INFN, Sezione di Milano-Bicocca, I-20126 Milano, Italy*
[137]*L2IT, Laboratoire des 2 Infinis - Toulouse, Université de Toulouse, CNRS/IN2P3, UPS, F-31062 Toulouse Cedex 9, France*

[138] *University of Portsmouth, Portsmouth, PO1 3FX, United Kingdom*
[139] *Université de Lyon, Université Claude Bernard Lyon 1, CNRS, Institut Lumière Matière, F-69622 Villeurbanne, France*
[140] *IGFAE, Universidade de Santiago de Compostela, 15782 Spain*
[141] *University of Chicago, Chicago, IL 60637, USA*
[142] *Dipartimento di Fisica, Università degli Studi di Genova, I-16146 Genova, Italy*
[143] *University of California, Riverside, Riverside, CA 92521, USA*
[144] *Department of Astronomy, Beijing Normal University, Xinjiekouwai Street 19, Haidian District, Beijing 100875, China*
[145] *Texas A&M University, College Station, TX 77843, USA*
[146] *OzGrav, University of Melbourne, Parkville, Victoria 3010, Australia*
[147] *INFN, Laboratori Nazionali del Sud, I-95125 Catania, Italy*
[148] *Niels Bohr Institute, Copenhagen University, 2100 København, Denmark*
[149] *Università di Roma Tor Vergata, I-00133 Roma, Italy*
[150] *University of Sannio at Benevento, I-82100 Benevento, Italy and INFN, Sezione di Napoli, I-80100 Napoli, Italy*
[151] *University of Massachusetts Dartmouth, North Dartmouth, MA 02747, USA*
[152] *Departamento de Astronomía y Astrofísica, Universitat de València, E-46100 Burjassot, València, Spain*
[153] *Observatori Astronòmic, Universitat de València, E-46980 Paterna, València, Spain*
[154] *The Chinese University of Hong Kong, Shatin, NT, Hong Kong*
[155] *University of British Columbia, Vancouver, BC V6T 1Z4, Canada*
[156] *Indian Institute of Technology Bombay, Powai, Mumbai 400 076, India*
[157] *Department of Physics, National Cheng Kung University, No.1, University Road, Tainan City 701, Taiwan*
[158] *National Tsing Hua University, Hsinchu City 30013, Taiwan*
[159] *National Central University, Taoyuan City 320317, Taiwan*
[160] *OzGrav, Charles Sturt University, Wagga Wagga, New South Wales 2678, Australia*
[161] *Queen Mary University of London, London E1 4NS, United Kingdom*
[162] *Department of Electrophysics, National Yang Ming Chiao Tung University, 101 Univ. Street, Hsinchu, Taiwan*
[163] *Kamioka Branch, National Astronomical Observatory of Japan, 238 Higashi-Mozumi, Kamioka-cho, Hida City, Gifu 506-1205, Japan*
[164] *University of Texas, Austin, TX 78712, USA*
[165] *CaRT, California Institute of Technology, Pasadena, CA 91125, USA*
[166] *Cornell University, Ithaca, NY 14850, USA*
[167] *Dipartimento di Ingegneria Industriale (DIIN), Università di Salerno, I-84084 Fisciano, Salerno, Italy*
[168] *Faculty of Science, University of Toyama, 3190 Gofuku, Toyama City, Toyama 930-8555, Japan*
[169] *Institute for Cosmic Ray Research, KAGRA Observatory, The University of Tokyo, 5-1-5 Kashiwa-no-Ha, Kashiwa City, Chiba 277-8582, Japan*
[170] *Université Lyon, Université Claude Bernard Lyon 1, CNRS, IP2I Lyon / IN2P3, UMR 5822, F-69622 Villeurbanne, France*
[171] *INAF, Osservatorio Astronomico di Padova, I-35122 Padova, Italy*
[172] *OzGrav, Swinburne University of Technology, Hawthorn VIC 3122, Australia*
[173] *INAF, Osservatorio Astronomico di Brera sede di Merate, I-23807 Merate, Lecco, Italy*
[174] *Departamento de Matemáticas, Universitat de València, E-46100 Burjassot, València, Spain*
[175] *Texas Tech University, Lubbock, TX 79409, USA*
[176] *Columbia University, New York, NY 10027, USA*
[177] *University of Rhode Island, Kingston, RI 02881, USA*
[178] *The University of Texas Rio Grande Valley, Brownsville, TX 78520, USA*
[179] *Bellevue College, Bellevue, WA 98007, USA*
[180] *Scuola Normale Superiore, I-56126 Pisa, Italy*
[181] *Chennai Mathematical Institute, Chennai 603103, India*
[182] *Università degli Studi di Sassari, I-07100 Sassari, Italy*
[183] *The University of Sheffield, Sheffield S10 2TN, United Kingdom*
[184] *Université Lyon, Université Claude Bernard Lyon 1, CNRS, Laboratoire des Matériaux Avancés (LMA), IP2I Lyon / IN2P3, UMR 5822, F-69622 Villeurbanne, France*
[185] *Dipartimento di Scienze Matematiche, Fisiche e Informatiche, Università di Parma, I-43124 Parma, Italy*
[186] *INFN, Sezione di Milano Bicocca, Gruppo Collegato di Parma, I-43124 Parma, Italy*
[187] *Perimeter Institute, Waterloo, ON N2L 2Y5, Canada*
[188] *Corps des Mines, Mines Paris, Université PSL, 60 Bd Saint-Michel, 75272 Paris, France*
[189] *Indian Institute of Technology Madras, Chennai 600036, India*
[190] *Carleton College, Northfield, MN 55057, USA*
[191] *National Center for Nuclear Research, 05-400 Świerk-Otwock, Poland*
[192] *Institut d'Astrophysique de Paris, Sorbonne Université, CNRS, UMR 7095, 75014 Paris, France*

[193] *Vrije Universiteit Brussel, 1050 Brussel, Belgium*
[194] *University of Zurich, Winterthurerstrasse 190, 8057 Zurich, Switzerland*
[195] *Canadian Institute for Theoretical Astrophysics, University of Toronto, Toronto, ON M5S 3H8, Canada*
[196] *Stony Brook University, Stony Brook, NY 11794, USA*
[197] *Center for Computational Astrophysics, Flatiron Institute, New York, NY 10010, USA*
[198] *Montclair State University, Montclair, NJ 07043, USA*
[199] *Institute for Nuclear Research, H-4026 Debrecen, Hungary*
[200] *CNR-SPIN, I-84084 Fisciano, Salerno, Italy*
[201] *Scuola di Ingegneria, Università della Basilicata, I-85100 Potenza, Italy*
[202] *Western Washington University, Bellingham, WA 98225, USA*
[203] *SUPA, University of the West of Scotland, Paisley PA1 2BE, United Kingdom*
[204] *The University of Utah, Salt Lake City, UT 84112, USA*
[205] *Eötvös University, Budapest 1117, Hungary*
[206] *Centro de Física das Universidades do Minho e do Porto, Universidade do Minho, PT-4710-057 Braga, Portugal*
[207] *Department of Physics, Graduate School of Science, Osaka Metropolitan University, 3-3-138 Sugimoto-cho, Sumiyoshi-ku, Osaka City, Osaka 558-8585, Japan*
[208] *Vanderbilt University, Nashville, TN 37235, USA*
[209] *Université Côte d'Azur, Observatoire de la Côte d'Azur, CNRS, Lagrange, F-06304 Nice, France*
[210] *California State University, Los Angeles, Los Angeles, CA 90032, USA*
[211] *University of Szeged, Dóm tér 9, Szeged 6720, Hungary*
[212] *INAF, Osservatorio Astronomico di Capodimonte, I-80131 Napoli, Italy*
[213] *Ariel University, Ramat HaGolan St 65, Ari'el, Israel*
[214] *Université de Normandie, ENSICAEN, UNICAEN, CNRS/IN2P3, LPC Caen, F-14000 Caen, France*
[215] *Laboratoire de Physique Corpusculaire Caen, 6 boulevard du maréchal Juin, F-14050 Caen, France*
[216] *The University of Mississippi, University, MS 38677, USA*
[217] *Institute of Physics, Academia Sinica, 128 Sec. 2, Academia Rd., Nankang, Taipei 11529, Taiwan*
[218] *Shanghai Astronomical Observatory, Chinese Academy of Sciences, 80 Nandan Road, Shanghai 200030, China*
[219] *American University, Washington, DC 20016, USA*
[220] *University of Nevada, Las Vegas, Las Vegas, NV 89154, USA*
[221] *Rochester Institute of Technology, Rochester, NY 14623, USA*
[222] *Department of Applied Physics, Fukuoka University, 8-19-1 Nanakuma, Jonan, Fukuoka City, Fukuoka 814-0180, Japan*
[223] *University of California, Berkeley, CA 94720, USA*
[224] *University of Lancaster, Lancaster LA1 4YW, United Kingdom*
[225] *College of Industrial Technology, Nihon University, 1-2-1 Izumi, Narashino City, Chiba 275-8575, Japan*
[226] *Faculty of Engineering, Niigata University, 8050 Ikarashi-2-no-cho, Nishi-ku, Niigata City, Niigata 950-2181, Japan*
[227] *Department of Physics, Tamkang University, No. 151, Yingzhuan Rd., Danshui Dist., New Taipei City 25137, Taiwan*
[228] *Rutherford Appleton Laboratory, Didcot OX11 0DE, United Kingdom*
[229] *Department of Astronomy and Space Science, Chungnam National University, 9 Daehak-ro, Yuseong-gu, Daejeon 34134, Republic of Korea*
[230] *Institute of Applied Physics, Nizhny Novgorod, 603950, Russia*
[231] *Kavli Institute for Astronomy and Astrophysics, Peking University, Yiheyuan Road 5, Haidian District, Beijing 100871, China*
[232] *Nambu Yoichiro Institute of Theoretical and Experimental Physics (NITEP), Osaka Metropolitan University, 3-3-138 Sugimoto-cho, Sumiyoshi-ku, Osaka City, Osaka 558-8585, Japan*
[233] *Directorate of Construction, Services & Estate Management, Mumbai 400094, India*
[234] *University of Białystok, 15-424 Białystok, Poland*
[235] *National Astronomical Observatories, Chinese Academic of Sciences, 20A Datun Road, Chaoyang District, Beijing, China*
[236] *School of Astronomy and Space Science, University of Chinese Academy of Sciences, 20A Datun Road, Chaoyang District, Beijing, China*
[237] *University of Southampton, Southampton SO17 1BJ, United Kingdom*
[238] *Department of Physics, Ulsan National Institute of Science and Technology (UNIST), 50 UNIST-gil, Ulju-gun, Ulsan 44919, Republic of Korea*
[239] *Institute for Cosmic Ray Research, The University of Tokyo, 5-1-5 Kashiwa-no-Ha, Kashiwa City, Chiba 277-8582, Japan*
[240] *Institute for High-Energy Physics, University of Amsterdam, 1098 XH Amsterdam, Netherlands*
[241] *Chung-Ang University, Seoul 06974, Republic of Korea*
[242] *University of Washington Bothell, Bothell, WA 98011, USA*
[243] *Aix Marseille Université, Jardin du Pharo, 58 Boulevard Charles Livon, 13007 Marseille, France*
[244] *Laboratoire de Physique et de Chimie de l'Environnement, Université Joseph KI-ZERBO, 9GH2+3V5, Ouagadougou, Burkina Faso*

[245]*Ewha Womans University, Seoul 03760, Republic of Korea*
[246]*Seoul National University, Seoul 08826, Republic of Korea*
[247]*Korea Astronomy and Space Science Institute, Daejeon 34055, Republic of Korea*
[248]*Sungkyunkwan University, Seoul 03063, Republic of Korea*
[249]*National Institute for Mathematical Sciences, Daejeon 34047, Republic of Korea*
[250]*Institute of Particle and Nuclear Studies (IPNS), High Energy Accelerator Research Organization (KEK), 1-1 Oho, Tsukuba City, Ibaraki 305-0801, Japan*
[251]*Bard College, Annandale-On-Hudson, NY 12504, USA*
[252]*Institute of Mathematics, Polish Academy of Sciences, 00656 Warsaw, Poland*
[253]*Department of Physics, Nagoya University, ES building, Furocho, Chikusa-ku, Nagoya, Aichi 464-8602, Japan*
[254]*Université de Montréal/Polytechnique, Montreal, Quebec H3T 1J4, Canada*
[255]*Inje University Gimhae, South Gyeongsang 50834, Republic of Korea*
[256]*NAVIER, École des Ponts, Univ Gustave Eiffel, CNRS, Marne-la-Vallée, France*
[257]*Università di Firenze, Sesto Fiorentino I-50019, Italy*
[258]*Department of Physics, University of Trento, via Sommarive 14, Povo, 38123 TN, Italy*
[259]*National Center for High-performance computing, National Applied Research Laboratories, No. 7, R&D 6th Rd., Hsinchu Science Park, Hsinchu City 30076, Taiwan*
[260]*NASA Marshall Space Flight Center, Huntsville, AL 35811, USA*
[261]*West Virginia University, Morgantown, WV 26506, USA*
[262]*School of Physics Science and Engineering, Tongji University, Shanghai 200092, China*
[263]*Institut d'Estudis Espacials de Catalunya, c. Gran Capità, 2-4, 08034 Barcelona, Spain*
[264]*Institucio Catalana de Recerca i Estudis Avançats (ICREA), Passeig de Lluís Companys, 23, 08010 Barcelona, Spain*
[265]*Tsinghua University, Beijing 100084, China*
[266]*Dipartimento di Fisica, Università di Trieste, I-34127 Trieste, Italy*
[267]*Institute for Photon Science and Technology, The University of Tokyo, 2-11-16 Yayoi, Bunkyo-ku, Tokyo 113-8656, Japan*
[268]*INFN Cagliari, Physics Department, Università degli Studi di Cagliari, Cagliari 09042, Italy*
[269]*Tata Institute of Fundamental Research, Mumbai 400005, India*
[270]*Hobart and William Smith Colleges, Geneva, NY 14456, USA*
[271]*Department of Physical Sciences, Aoyama Gakuin University, 5-10-1 Fuchinobe, Sagamihara City, Kanagawa 252-5258, Japan*
[272]*Institut des Hautes Etudes Scientifiques, F-91440 Bures-sur-Yvette, France*
[273]*Faculty of Law, Ryukoku University, 67 Fukakusa Tsukamoto-cho, Fushimi-ku, Kyoto City, Kyoto 612-8577, Japan*
[274]*Indian Institute of Science Education and Research, Kolkata, Mohanpur, West Bengal 741252, India*
[275]*Department of Physics and Astronomy, University of Notre Dame, 225 Nieuwland Science Hall, Notre Dame, IN 46556, USA*
[276]*University of Stavanger, 4021 Stavanger, Norway*
[277]*Department of Astronomy, The University of Tokyo, 7-3-1 Hongo, Bunkyo-ku, Tokyo 113-0033, Japan*
[278]*Laboratoire Univers et Théories, Observatoire de Paris, 92190 Meudon, France*
[279]*Observatoire de Paris, 75014 Paris, France*
[280]*Université PSL, 75006 Paris, France*
[281]*Université de Paris Cité, 75006 Paris, France*
[282]*Graduate School of Science and Technology, Niigata University, 8050 Ikarashi-2-no-cho, Nishi-ku, Niigata City, Niigata 950-2181, Japan*
[283]*Niigata Study Center, The Open University of Japan, 754 Ichibancho, Asahimachi-dori, Chuo-ku, Niigata City, Niigata 951-8122, Japan*
[284]*Department of Physics, The University of Tokyo, 7-3-1 Hongo, Bunkyo-ku, Tokyo 113-0033, Japan*
[285]*CSIR-Central Glass and Ceramic Research Institute, Kolkata, West Bengal 700032, India*
[286]*Consiglio Nazionale delle Ricerche - Istituto dei Sistemi Complessi, I-00185 Roma, Italy*
[287]*Department of Physics, Aristotle University of Thessaloniki, 54124 Thessaloniki, Greece*
[288]*Museo Storico della Fisica e Centro Studi e Ricerche "Enrico Fermi", I-00184 Roma, Italy*
[289]*Dipartimento di Ingegneria Industriale, Elettronica e Meccanica, Università degli Studi Roma Tre, I-00146 Roma, Italy*
[290]*INFN, Sezione di Roma Tre, I-00146 Roma, Italy*
[291]*Università di Trento, Dipartimento di Matematica, I-38123 Povo, Trento, Italy*
[292]*Subatech, CNRS/IN2P3 - IMT Atlantique - Nantes Université, 4 rue Alfred Kastler BP 20722 44307 Nantes CÉDEX 03, France*
[293]*Universidad de Antioquia, Medellín, Colombia*
[294]*Departamento de Física - ETSIDI, Universidad Politécnica de Madrid, 28012 Madrid, Spain*
[295]*Department of Electronic Control Engineering, National Institute of Technology, Nagaoka College, 888 Nishikatakai, Nagaoka City, Niigata 940-8532, Japan*
[296]*Departamento de Matemática da Universidade de Aveiro and Centre for Research and Development in Mathematics and Applications, 3810-183 Aveiro, Portugal*

[297] Marquette University, Milwaukee, WI 53233, USA
[298] Faculty of Science, Toho University, 2-2-1 Miyama, Funabashi City, Chiba 274-8510, Japan
[299] Indian Institute of Technology, Palaj, Gandhinagar, Gujarat 382355, India
[300] Laboratoire MSME, Cité Descartes, 5 Boulevard Descartes, Champs-sur-Marne, 77454 Marne-la-Vallée Cedex 2, France
[301] Graduate School of Science and Technology, Gunma University, 4-2 Aramaki, Maebashi, Gunma 371-8510, Japan
[302] Institute for Quantum Studies, Chapman University, 1 University Dr., Orange, CA 92866, USA
[303] Faculty of Information Science and Technology, Osaka Institute of Technology, 1-79-1 Kitayama, Hirakata City, Osaka 573-0196, Japan
[304] INAF, Osservatorio Astrofisico di Arcetri, I-50125 Firenze, Italy
[305] Indian Institute of Technology Hyderabad, Sangareddy, Khandi, Telangana 502285, India
[306] Indian Institute of Science Education and Research, Pune, Maharashtra 411008, India
[307] Institut für Theoretische Physik, Johann Wolfgang Goethe-Universität, Max-von-Laue-Str. 1, 60438 Frankfurt am Main, Germany
[308] Istituto di Astrofisica e Planetologia Spaziali di Roma, 00133 Roma, Italy
[309] INAF, Osservatorio di Astrofisica e Scienza dello Spazio, I-40129 Bologna, Italy
[310] Universidade Estadual Paulista, 01140-070 Campinas, São Paulo, Brazil
[311] Research Center for Space Science, Advanced Research Laboratories, Tokyo City University, 8-15-1 Todoroki, Setagaya, Tokyo 158-0082, Japan
[312] Department of Physics, Kyoto University, Kita-Shirakawa Oiwake-cho, Sakyou-ku, Kyoto City, Kyoto 606-8502, Japan
[313] Institute for Cosmic Ray Research, Research Center for Cosmic Neutrinos, The University of Tokyo, 5-1-5 Kashiwa-no-Ha, Kashiwa City, Chiba 277-8582, Japan
[314] Yukawa Institute for Theoretical Physics (YITP), Kyoto University, Kita-Shirakawa Oiwake-cho, Sakyou-ku, Kyoto City, Kyoto 606-8502, Japan
[315] University of Catania, Department of Physics and Astronomy, Via S. Sofia, 64, 95123 Catania CT, Italy
[316] Dipartimento di Scienze Aziendali - Management and Innovation Systems (DISA-MIS), Università di Salerno, I-84084 Fisciano, Salerno, Italy
[317] National Institute of Technology, Fukui College, Geshi-cho, Sabae-shi, Fukui 916-8507, Japan
[318] Department of Communications Engineering, National Defense Academy of Japan, 1-10-20 Hashirimizu, Yokosuka City, Kanagawa 239-8686, Japan
[319] Eindhoven University of Technology, 5600 MB Eindhoven, Netherlands
[320] Department of Physics and Astronomy, Sejong University, 209 Neungdong-ro, Gwangjin-gu, Seoul 143-747, Republic of Korea
[321] Concordia University Wisconsin, Mequon, WI 53097, USA
[322] School of Physics and Technology, Wuhan University, Bayi Road 299, Wuchang District, Wuhan, Hubei, 430072, China

ABSTRACT

1. INTRODUCTION

The discovery of gravitational waves (GWs) from coalescing binary black holes (BBH) by the Laser Interferometer Gravitational-Wave Observatory (LIGO) opened a new window to the Universe (Abbott et al. 2016a). In addition to GWs, compact binary mergers with at least one neutron star (NS) component are likely to generate electromagnetic (EM) radiation (e.g., Nakar 2020a; Kyutoku et al. 2021). Coincident detection of EM emission from compact binary mergers provides a complete picture of the merger process and can have huge implications for our understanding of the Universe. Such coincidences play a crucial role in tracing the properties of the source host galaxy (Troja et al. 2017; Alexander et al. 2017), mitigating degeneracies in GW parameter estimation (Abbott et al. 2017a; Hughes & Holz 2003; Wang & Giannios 2021), placing constraints on the NS equation of state (Bauswein et al. 2017; Radice et al. 2018), and investigating the expansion rate of the Universe, thereby testing cosmological models (Abbott et al. 2017a,b; Hotokezaka et al. 2019; Nissanke et al. 2013; Schutz 1986). Additionally, they allow for the measurement of arrival time differences between photons and gravitons, providing limits to the mass of a graviton, exploring potential violations to the equivalence principle and Lorentz invariance (Abbott et al. 2017e).

The joint detection of the first GW event consistent with a binary NS (BNS) coalescence GW170817 (Abbott et al. 2017a), and a coincident short gamma-ray burst GRB 170817A (Goldstein et al. 2017a; Savchenko et al. 2017), accompanied by the optical/infrared *kilonova* counterpart AT 2017gfo (Arcavi et al. 2017; Coulter et al. 2017; Tanvir et al. 2017; Evans et al. 2017; Pian et al. 2017; Smartt et al. 2017; Drout et al. 2017; Cowperthwaite et al. 2017) and the GRB afterglow (in the X-rays: Troja et al. 2017; Margutti et al. 2017 and radio: Hallinan et al. 2017), together ushered in a new era in the field of multi-messenger astrophysics and for-

---

[*] Deceased, November 2022.

[†] Deceased, July 2023.

ever impacted our comprehension of compact binary coalescences (CBC) involving an EM counterpart. Massive coordinated EM follow-up efforts were dedicated to deeply monitor the error regions derived from the joint sky localization of GW detectors and high-energy satellites, helping to reduce the initial three detector network sky localization from 28 deg^2 to within a few arcseconds of the host galaxy NGC 4993 (Abbott et al. 2017d,a). The spectacular spectral and light curve evolution of this transient (Abbott et al. 2017d; Villar et al. 2017) suggested that this explosive event was an active site for r-process nucleosynthesis (Pian et al. 2017; Smartt et al. 2017; Coulter et al. 2017; Drout et al. 2017) (for a detailed review of the multimessenger observations of GW170817, see, e.g., Nakar 2020b; Margutti & Chornock 2021).

The expected EM counterpart emission from BNS or neutron star–black hole (NSBH) mergers can potentially be weak due to various factors such as considerable source distances, an off-axis viewing angle, or limited amount of ejected mass. For the specific case of GW170817, despite a coincident GRB detection, it took nearly half a day to localize the host galaxy and begin observations of the kilonova (Abbott et al. 2017a). Prompt targeted searches around the GW trigger times, leveraging facilities with enhanced localization capabilities, can refine search strategies and assist optical or infrared (IR) facilities in correctly identifying and pursuing transient candidates for subsequent follow-up studies. In addition to prompt searches, *Fermi*-GBM analysis of triggers from the first and second LIGO–Virgo observing runs showed that targeted *offline* searches are capable of recovering additional candidate joint events that may be of astrophysical relevance (Hamburg et al. 2020; Pillas et al. 2023). Temporal and spatial coincidence information can be used to derive the joint false alarm rate (FAR). These estimates have the potential to elevate subthreshold triggers in either the GW or GRB domains to the status of an above-threshold candidate detection (Nitz et al. 2019).

Unlike *Fermi*, *Swift* has been for a long time incapable of relaying a continuous stream of event mode data to the ground in real time. Such a capability was enabled through GUANO (Gamma-ray Urgent Archiver for Novel Opportunities, described in Section 2) (Tohuvavohu et al. 2020), which recovers event data from the *Swift* Burst Alert Telescope (BAT, Barthelmy et al. 2005), that then get processed by the Non-Imaging Transient Reconstruction And TEmporal Search (NITRATES, DeLaunay & Tohuvavohu 2022) pipeline (see Section 4) to search for subthreshold transient candidates.[1] In addition to other astronomical transients, such as GRBs, fast radio bursts (FRBs), and high-energy neutrinos, the GUANO-NITRATES infrastructure performs targeted searches on GW events communicated by the LVK Collaboration, to detect possible GRBs associated with CBCs.

The impact and potential of *Swift*-BAT subthreshold searches are crucial for multi-messenger related goals. Indeed, deeper targeted searches increase the joint detection horizon, thus enhancing the probability of finding weak EM counterparts of CBCs in the hard X-ray domain. Moreover, thanks to the high spatial accuracy enabled by the BAT coded mask, subthreshold searches open the possibility of recovering the position of the candidate EM event at the precision level of a few arcminutes, fundamental to drive the subsequent follow-up with ground and space-based EM facilities.

Currently, the targeted search analysis carried out thanks to GUANO, has enabled the discovery of more than 35 GRBs with arcminute localization. A total of 7 of the detected GRBs have a duration < 2 s (e.g., DeLaunay et al. 2020; Tohuvavohu et al. 2022a), hence they are potentially associated with CBCs containing at least one NS. GUANO data have also been used for the localization of 29 long GRBs through imaging (e.g., DeLaunay et al. 2021a) and non-imaging analysis techniques (e.g., DeLaunay et al. 2021b; Tohuvavohu et al. 2022b). GRB 220107A, detected during BAT slew and localized with arcminute precision, enabled the first optical redshift measured using GUANO data (DeLaunay et al. 2022a). The arcminute localization of GRB 211106A enabled prompt multiband follow up and led to the discovery of the first afterglow in the millimeter band from a short GRB (Tohuvavohu et al. 2021a). With GUANO, one can additionally recover coarse localization information on GRB-like transients that originate from outside the BAT field of view (FOV; e.g., DeLaunay et al. 2023).

In addition to the application to real-time analysis, the availability of BAT data enables us to perform a systematic, deeper targeted search focused on archival LVK triggers. The goal of this study is to perform such an analysis on all the LVK triggers received during the third LIGO–Virgo observing run, during which the GUANO pipeline started to be fully operational. The run duration was comprised of two segments: O3a, which operated from April 1, 2019, 15:00 UTC to October 1, 2019, 15:00, and O3b which operated from

[1] Live reporting of the status of the real time *Swift*-BAT subthreshold analysis can be found at https://guano.swift.psu.edu, where the user can monitor all the triggers ingested by GUANO and visualize the main results of the NITRATES analysis.

November 1, 2019, 15:00 UTC, to March 27, 2020, 17:00 UTC. The alerts distributed during O3 were reporting the following parameters: FAR, the signal classification (CBC or unmodeled Burst), and the associated astrophysical probabilities. The results of O3 are summarized in Gravitational-Wave Transient Catalog data releases GWTC-2 (Abbott et al. 2021), GWTC-2.1 (Abbott et al. 2024), and GWTC-3 (Abbott et al. 2023).

In this work, we use *Swift*-BAT observations to carry out offline targeted subthreshold searches for EM counterparts of the GW triggers obtained during O3. The rest of the paper is organized as follows: In Section 2, we describe the *Swift*-BAT instrument and its new capabilities, and in Section 3, we provide details about the GW trigger sample used for the analysis. In Section 4 we summarize the targeted search method adopted for the analysis. We present the results from our targeted search analysis on the various subcategories of triggers in Section 5, and discuss the scientific interpretation in Section 6.

2. *Swift*-BAT

The Neil Gehrels *Swift* Observatory (henceforth, *Swift*) is a GRB-focused mission launched in 2004, with three onboard payloads – the Burst Alert Telescope (BAT), the X-ray Telescope (XRT), and the UltraViolet/Optical Telescope (UVOT) – covering the EM spectrum from hard X-rays and gamma-rays all the way to the optical (Gehrels et al. 2004). The BAT instrument (Barthelmy et al. 2005) is a hard X-ray coded mask imager with a wide FOV that operates in the broad energy band of 15–350 keV. It is the primary instrument that detects GRBs and performs an onboard imaging analysis via a cross-correlation between the spatial pattern of the counts across the detector array and the pattern of the coded mask. The sensitivity of BAT is capable of providing arcminute localizations of GRBs triggered onboard (Gehrels et al. 2004). Due to the lack of continuous downlinking of timing, spatial, and energy information for each detector count (event mode data), carrying out targeted searches offline has not been possible in the past. A new infrastructure, called GUANO, was incorporated into the *Swift*-BAT operations in 2019. Details of the GUANO operations can be found in Tohuvavohu et al. (2020). From the outset, GUANO has demonstrated that recovering event mode data from astrophysically compelling time windows can enhance the overall transient detection rate and sensitivity of BAT (Tohuvavohu et al. 2020).

3. GRAVITATIONAL-WAVE TRIGGER SAMPLE

This paper focuses on the *Swift*-BAT subthreshold analysis of a sample of GW triggers with a FAR<2 per day, distributed by the LVK Collaboration during O3. The subthreshold GW alerts were received by the EM follow-up groups that were part of a Memorandum of Understanding with the LVK Collaboration. For candidates found with CBC search pipelines (Dal Canton et al. 2021; Sachdev et al. 2019; Messick et al. 2017; Aubin et al. 2021; Nitz et al. 2018; Hooper et al. 2012) and Burst search pipelines (Klimenko et al. 2005, 2016), the alerts contain basic information about the GW FAR, the probability of the candidate being astrophysical ($p_{\rm astro}$) and trigger time. In the case of CBC candidates, the alerts received in low latency report the $p_{\rm astro}$ split in the four CBC classes: BBH, BNS, NSBH, and Mass Gap. The Mass Gap category includes CBC candidates in which at least one component has a mass in the range [3–5] $M_{\odot}$. Using the GW trigger information received in low latency, we can further perform a search for associations in BAT data.

From the list of 1552 alerts that were communicated via low latency channels, we obtained successful GUANO data dumps for 636 triggers. The GW information of the candidates received in low latency are reported in Table 1. The FAR and the $p_{\rm astro}$ classification reported here correspond to the preferred event, namely the one with the highest SNR. *Swift*-BAT event mode data coincident with the GW trigger time were made available for these triggers in real time via the GUANO data dumps. Post-processing on the data was carried out on this sample from O3 using the NITRATES analysis pipeline (see Section 4).

Out of the 636 low-latency alerts, a total of 86 GW candidates have been confirmed by the offline analysis and included in the GWTC-2.1 and GWTC-3 data releases (Abbott et al. 2024; Abbott et al. 2023). Among the 86 confirmed candidates, 14 triggers have $p_{\rm astro} > 0.5$ and 72 triggers have $p_{\rm astro} < 0.5$. We indicate the details of the confirmed candidates with $p_{\rm astro} > 0.5$ and $p_{\rm astro} < 0.5$ in Table 2 and Table 3, respectively. The values of FAR, $p_{\rm astro}$ and CBC Class given in Table 2 and Table 3 are derived from offline analyses, as reported in GWTC-2.1 and GWTC-3 data releases, hence are considered more reliable than the values obtained in low latency, reported in Table 1. The FAR and the $p_{\rm astro}$ classification reported in Tables 2 and 3 come from the pipeline that gives the highest value of $p_{\rm astro}$. For high significance events, if multiple pipelines derive a $p_{\rm astro} \simeq 1$, we select the one with highest SNR. According to these rules, in the case of S200225q, reported in Table 2, the selected pipeline is cWB, but the event is classified as CBC. The CBC class is determined by the highest among $p_{\rm BBH}$, $p_{\rm NSBH}$ and $p_{\rm BNS}$. In Tables 2 and 3 we report the value of $p_{\rm Class}$ defined as

$\max[p_{\rm BBH}, p_{\rm NSBH}, p_{\rm BNS}]$. It is possible that some candidates marked as "Burst" in Table 1 are then re-classified as "CBC" by the offline analysis. Therefore, for each catalog event the most updated group is the one reported in Tables 2 and 3.

In Figure 1 we show the histograms of the $p_{\rm astro}$ probabilities for all the low-latency CBC candidates processed by GUANO, for a total of 424 candidates, divided into 67 BBH, 130 BNS, 148 NSBH, and 79 Mass Gap events (Fig. 2, left panel). In the offline post-processing of GW candidates, the Mass Gap classification was removed, classifying an object with $M > 3M_{\odot}$ as a black hole. This implies that all the CBC events with at least one component mass in the range $[3-5]M_{\odot}$ are re-distributed into the BBH and NSBH classes. The distribution of the updated $p_{\rm astro}$ classification released by LVK is over-plotted in Figure 1, and the classes are divided in 39 BBH, 22 BNS and 17 NSBH candidates (Fig. 2, right panel).

3.1. *GW sky localization*

For the selection of the GW sky localization for each candidate we adopt the following scheme:

1. Above–threshold GW candidate: The GW candidate is contained in the list of high-probability ($p_{\rm astro} > 0.5$) candidates reported in Table 2 of GWTC-2.1 (Abbott et al. 2024) or Table 1 of GWTC-3 (Abbott et al. 2023). The GW sky localizations are downloaded from the parameter estimation data releases of GWTC-2.1 and GWTC-3.[2] We use the results derived from a combination of IMRPhenomXPHM (Pratten et al. 2021) and SEOBNRv4PHM (Ossokine et al. 2020) waveforms (labeled as 'Mixed' in the release).

2. Subthreshold GW candidate: The GW candidate is classified as low-probability ($p_{\rm astro} < 0.5$) in the offline analysis. The GW sky localization is produced by BAYESTAR (Singer & Price 2016; Singer et al. 2016) and is taken from the GWTC-3 release, which contains both O3b events and updated O3a events. If multiple events are present for a single GW candidate, the pipeline with the highest $p_{\rm astro}$ is considered for the selection of the sky localization.

3. Non-confirmed low-latency GW candidate: The GW candidate has an associated low-latency alert, but the event has not been confirmed by the offline analysis. The GW sky localization is downloaded from GraceDB, selecting the preferred event.

4. TARGETED SEARCHES USING GUANO-NITRATES

Targeted searches are carried out in real time for all types of transients such as GRBs, FRBs, neutrino events as well as GW triggers, on the event mode data obtained using GUANO. The targeted search pipeline that is currently operational is NITRATES. This is a maximum–likelihood framework that forward models signals through the entire instrument response (DeLaunay & Tohuvavohu 2022). The BAT responses are created by simulating the photon paths through all detector segments using Geant4, which is a particle-interaction simulator software toolkit (Allison et al. 2016). Unlike the standard BAT responses, the NITRATES responses account for all the detectors on the focal plane, regardless of their coding by the mask. The responses also encode details on the gamma-ray interactions inside the instrument, which carry additional information. This approach enables substantial sensitivity gain compared to the conventional technique of cross-correlation imaging, which translates to a 50% increase in the detection horizon distance for a GRB 170817A-like burst compared to the onboard imaging. Details of the NITRATES response generation and the analysis pipeline are provided in DeLaunay & Tohuvavohu (2022).

A GRB-like transient signal is described using the sky localization and parameters that are specific to the assumed spectral model (the peak energy and spectral slope). This framework then computes the significance of each signal using a test statistic (TS) by maximizing the log-likelihood (LLH) as a function of signal parameters. The likelihood ratio test statistic Λ is used to compare the source signal+background model (described using a set of parameters, $\Theta^{\rm sig}$ that maximizes the LLH) to a background-only model (described by the set of parameters $\Theta^{\rm off}_{\rm bkg}$, that maximizes the LLH in the off-time window) and is defined as follows (DeLaunay & Tohuvavohu 2022):

$$\Lambda = -2[{\rm LLH}(\Theta^{\rm off}_{\rm bkg}|{\rm N}^{\rm on}) - {\rm LLH}(\Theta_{\rm sig}, \Theta^{\rm off}_{\rm bkg}|{\rm N}^{\rm on})], \quad (1)$$

where $N^{\rm on}$ is on-time data.

The search pipeline workflow can be summarized as follows:

1. The event mode data is cleaned and filtered to discard potential glitches and artifacts from cosmic rays, and to flag poorly behaving detectors. Good time intervals (GTIs) are determined, where there is quality data for the analysis.

---

[2] GWTC-2.1 release https://doi.org/10.5281/zenodo.6513631, GWTC-3 release https://doi.org/10.5281/zenodo.8177023

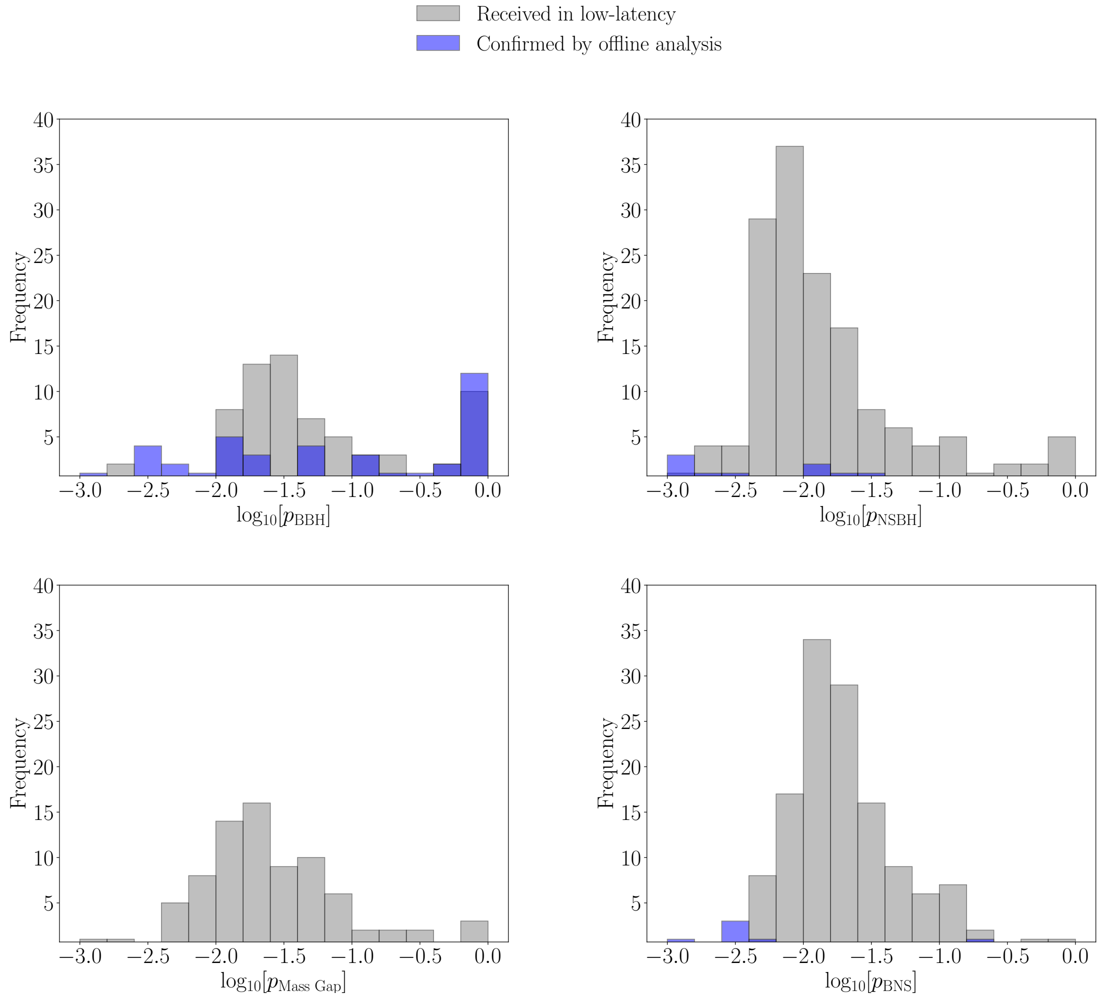

Figure 1. Distribution of the p_{astro} values for the CBC triggers detected during O3, with available GUANO data dumps. We distinguish with different colors the triggers received in low latency and the ones confirmed by offline analysis.

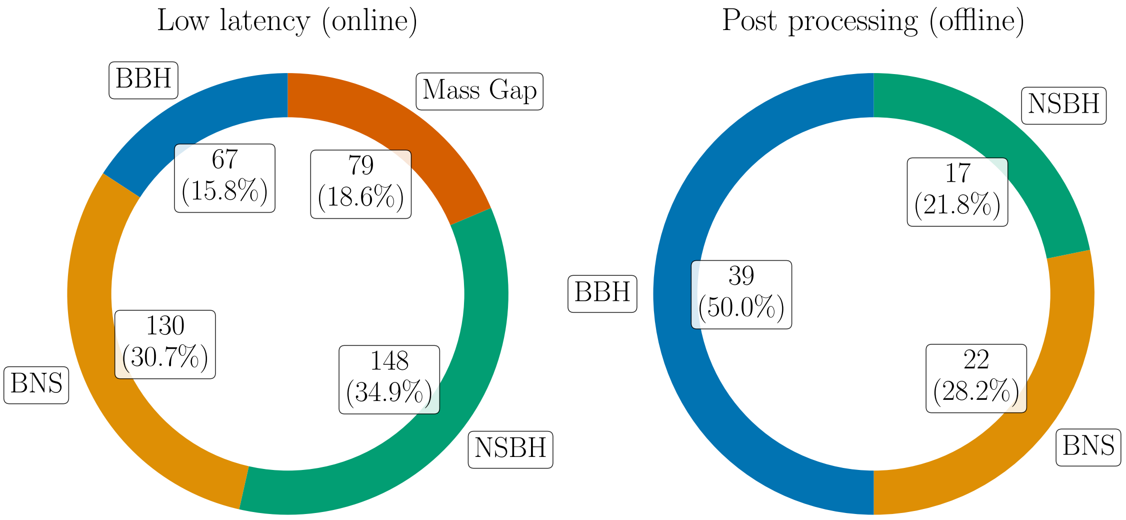

Figure 2. Left: distribution of the CBC triggers from O3 received in low latency, which had successful GUANO data dumps, divided in the BBH, NSBH, BNS, and Mass Gap classes. Right: analogous distribution for the CBC candidates confirmed by the offline analysis. In the post-processing, the Mass Gap classification has been subsumed into BBH and NSBH.

2. A time window of 50 s (from the pre- and post-trigger intervals) is identified as the background interval. It is then utilized to model contributions to the background from known bright sources and diffuse sources.
3. To narrow down the search parameter space, a set of simple analyses are performed to select a list of interesting start times and durations (hereafter referred to as time seeds) as well as portions of the BAT FOV (position seeds).
4. Finally, the log-likelihoods are computed for all parameters corresponding to the shortlisted time and position seeds.

In essence, the set of signal parameters that maximizes the log-likelihood is the most preferred set of parameters.

The NITRATES likelihood analysis outperforms the onboard mask-weighted imaging analysis by delivering superior sensitivity, given the increased effective area (see Fig. 2 in DeLaunay & Tohuvavohu 2022). At the cost of a significantly increased computational time, this method is capable of delivering arcminute scale localization for events that fall inside the BAT FOV, even when the transient event does not trigger *Swift*-BAT onboard (Tohuvavohu et al. 2021b; Tohuvavohu 2023; DeLaunay et al. 2022b). The NITRATES pipeline has the ability to distinguish between bursts that come from in and outside the BAT FOV. NITRATES has also accurately localized sufficiently bright bursts outside the FOV (DeLaunay & Tohuvavohu 2022).

Swift-BAT GUANO was operating during the O3 and was successfully procuring event mode information in response to GW subthreshold triggers (Tohuvavohu et al. 2020). We describe the targeted search analysis that has been carried out using the NITRATES version 0.0.1 which was available in early 2022.[3] The targeted search analysis that was operational in O3 corresponded to a preliminary version of the NITRATES code, that has since undergone several stages of development. The most updated version is publicly available on GitHub.[4]

During O3, for a total of 636 GW triggers, GUANO dumped either 200 s or 90 s of event mode data, for public triggers and for privately communicated triggers, respectively. The choice of the width of the temporal window is made to avoid an overload of downlink data in the process of GUANO data dump. The targeted search pipeline was run in a time window of ±20 s centered around the trigger time. The search was carried out on 8 time bins (0.128 s, 0.256 s, 0.512 s, 1.024 s, 2.048 s, 4.096 s, 8.192 s and 16.384 s) and 9 energy bins (between 15–350 keV). The results from the search are reported using the following set of parameters: 1) the maximum $\sqrt{\mathrm{TS}}$ describes the statistical significance of a potential detection (see Section 5); 2) $\Delta\mathrm{LLH}_{\mathrm{out}}$ indicates the preference of the search to a location inside or outside the BAT FOV, and 3) $\Delta\mathrm{LLH}_{\mathrm{peak}}$ indicates the confidence of the search in localizing the source to arcminute scales.

The NITRATES search was performed on the ROAR supercomputing cluster on a set of 200 virtual cores for a total of $\sim 600 \times 800$ CPU hours for the entire GW sample.

5. RESULTS FROM NITRATES

The targeted search analysis provides a list of top candidates whose spatial, temporal, and spectral parameters maximize the log-likelihood. In order for a candidate to be qualified as a confident detection, we require that the resulting detection significance parameter $\sqrt{\mathrm{TS}}$ must exceed the threshold value of 8, corresponding to a FAR $\sim 4 \times 10^{-5}$ Hz. Being a targeted search, the NITRATES analysis can give a false positive with $\sqrt{\mathrm{TS}} > 8$ with a probability which follows a Poissionian distribution:

$$P(N_{\mathrm{det}} \geq 1) = 1 - P(N_{\mathrm{det}} = 0) = 1 - e^{-\mathrm{FAR} \times \Delta t}, \quad (2)$$

with $\Delta t = 40$ s being the width of the search window. This leads to a pre-trial p-value of 1.6×10^{-3}. Since the NITRATES analysis is performed on all GW triggers with a FAR < 2 day^{-1}, and considering that there are $N_{\mathrm{GW-search}} = 5$ independent GW pipelines, the rate of expected false positive candidates with $\sqrt{\mathrm{TS}} > 8$ is $\sim 5 \times 2 \times 1.6 \times 10^{-3}$ /day $\sim 1/(60$ day$)$.[5]

For the entire sample of 636 low-latency triggers processed using NITRATES, we have no candidates that qualify as detection of a signal of astrophysical origin. None of the top candidates within the ±20 s search window are coincident with the GW triggers. A temporal coincidence with a GW trigger is claimed if the NITRATES search finds a candidate with $\sqrt{\mathrm{TS}} > 8$ and $|t_0 - t_{\mathrm{start}}| < 20$ s, where t_0 is the GW trigger time and t_{start} is the starting time of the temporal bin with highest ranking statistics. A detailed list of all the NITRATES results for the entire sample analyzed during

---

[3] https://github.com/Swift-BAT/NITRATES/tree/py2

[4] https://github.com/Swift-BAT/NITRATES

[5] Since the GW pipelines are not totally independent, a realistic value of $N_{\mathrm{GW-search}}$ is likely below 5, leading to an overall rate of false NITRATES candidate below 1/(60 day).

O3 is provided in Table 1. We discuss specific false positive candidates in Section 5.1.

If the GW trigger time is included in the time window corresponding to slew mode of BAT, the analysis cannot be performed using NITRATES since the targeted search requires stable attitude information to compute the background. Similarly, some triggers have insufficient exposure time, preventing the NITRATES analysis. In this case neither TS results nor flux upper limits can be computed. As a cut to narrow down the parameter space, the targeted search selects time seeds as described in Section 4. If there are no time seeds that pass the preliminary cuts then there will be no final likelihood computations. Results for these types of triggers are indicated as NFL (No Final Likelihood) in Table 1. In the case of NFL triggers, though, the flux upper limit can be computed, since a full likelihood analysis is not required.

5.1. *False positives*

We did not find any candidate associations from any of the triggers with BAT. However, the targeted search pipeline did result in the detection of six candidates with a significance above the NITRATES detection threshold of $\sqrt{\mathrm{TS}} = 8$. These candidates were examined to understand our false positive population. S200327j ($\sqrt{\mathrm{TS}} \sim 22$), S200324ax ($\sqrt{\mathrm{TS}} \sim 11$), and S200225af ($\sqrt{\mathrm{TS}} \sim 10.5$) are triggers that occurred during the passage of *Swift* in the proximity of the South Atlantic Anomaly (SAA). The background characterization becomes unreliable when the spacecraft is either entering or leaving the SAA on account of increased background contamination. In S190919au, a peculiar dip ($\sim$20 s) in the background may have contributed to a false elevation in the signal detection statistic, by causing an under representation of the background rate. For S190919u, we obtain a $\sqrt{\mathrm{TS}} \sim 8.0$, which corresponds to a FAR of $\sim 4 \times 10^{-5}$ Hz. The presence of such a detection, in a total sample of 636 triggers that were analyzed, is compatible with the expected number of false positives, which corresponds to $(4 \times 10^{-5}\ \mathrm{Hz}) \times (40\ \mathrm{s}) \times 636 \sim 1$.

S200130ai corresponds to a subthreshold GW trigger at T_0 = 2020-01-30T09:59:58 that was identified by the CBC search as a NSBH candidate with a $p_{\mathrm{astro}} = 0.008$ and a GW FAR $\sim 1.8\times10^{-5}$ Hz. It was detected using NITRATES at a significance of $\sqrt{\mathrm{TS}} \sim 16.3$ with a $\Delta\mathrm{LLH}_{\mathrm{out}} = -19.68$ and $\Delta\mathrm{LLH}_{\mathrm{peak}} = 2.14$, consistent with a sky localization outside the BAT-FOV. The highest log-likelihood candidate, was identified to arise 1.5 s prior to the GW trigger time. Due to the low value of $\Delta\mathrm{LLH}_{\mathrm{peak}}$, we do not have an arcminute-level precision on the sky localization. The candidate was associated with a *Fermi* trigger 602071201 (GCN 26944, Fermi GBM Team 2020) and was classified as a long GRB. The Fermi localization is RA = 137.5 deg, Dec = −51.3 deg, with a statistical uncertainty of 3.5 degrees. The Interplanetary Gamma-Ray Burst Timing Network (IPN) further localized the event in a 3-sigma error box with an area of 1487 arcmin^2 and centered at an RA = 134.742 deg and Dec = −49.627 deg (Hurley et al. 2020). Although this event presents a temporal coincidence with the GW trigger, on account of the lack of spatial coincidence with the GW location, this event is discarded from being associated with the GW subthreshold trigger. Additionally, this low-latency GW candidate has not been confirmed by offline analyses.

5.2. *Computation of flux upper limits*

Since each GW trigger processed in this analysis resulted in a non-detection in *Swift*-BAT, we estimate the flux upper limits in the following manner. The NITRATES analysis generates rates curves in the 15–350 keV energy band from the GTIs of the filtered event list. The number of active detectors corresponding to each trigger is read out from its respective detector mask file. A linear fit is carried out to the background window of duration 50 s. We then estimate the 5σ count rate and the corresponding uncertainty over the full signal window which has a ±20 s duration. This is computed for all the 8 time bins (see Section 4). We further convert the 5σ count rates to flux upper limits, as a function of sky position, in the 15–350 keV band, by convolving different spectral models with the NITRATES responses for each time bin iteration. We select 929 grid points on the sky and interpolate upper limit values for locations in between. We assume the following different spectral templates:

1. Band function (Band et al. 1993) with a soft template ($E_{\mathrm{peak}} = 70$ keV, $\alpha = -1.9$, $\beta = -3.7$)
2. Band function with a normal template ($E_{\mathrm{peak}} = 230$ keV, $\alpha = -1.0$, $\beta = -2.3$)
3. Cutoff power law function with a hard template ($E_{\mathrm{peak}} = 1500$ keV, $\alpha = 1.5$)
4. Cutoff power law function that has been used to describe GRB 170817A ($E_{\mathrm{peak}} = 185$ keV, $\alpha = 0.62$) (Goldstein et al. 2017b)

The parameters α and β correspond to the low-energy and high-energy photon indices of the spectrum, respectively. The first three spectral templates are identical to the ones that are routinely adopted by *Fermi*-GBM (Goldstein et al. 2016a). In the rest of the paper, all the

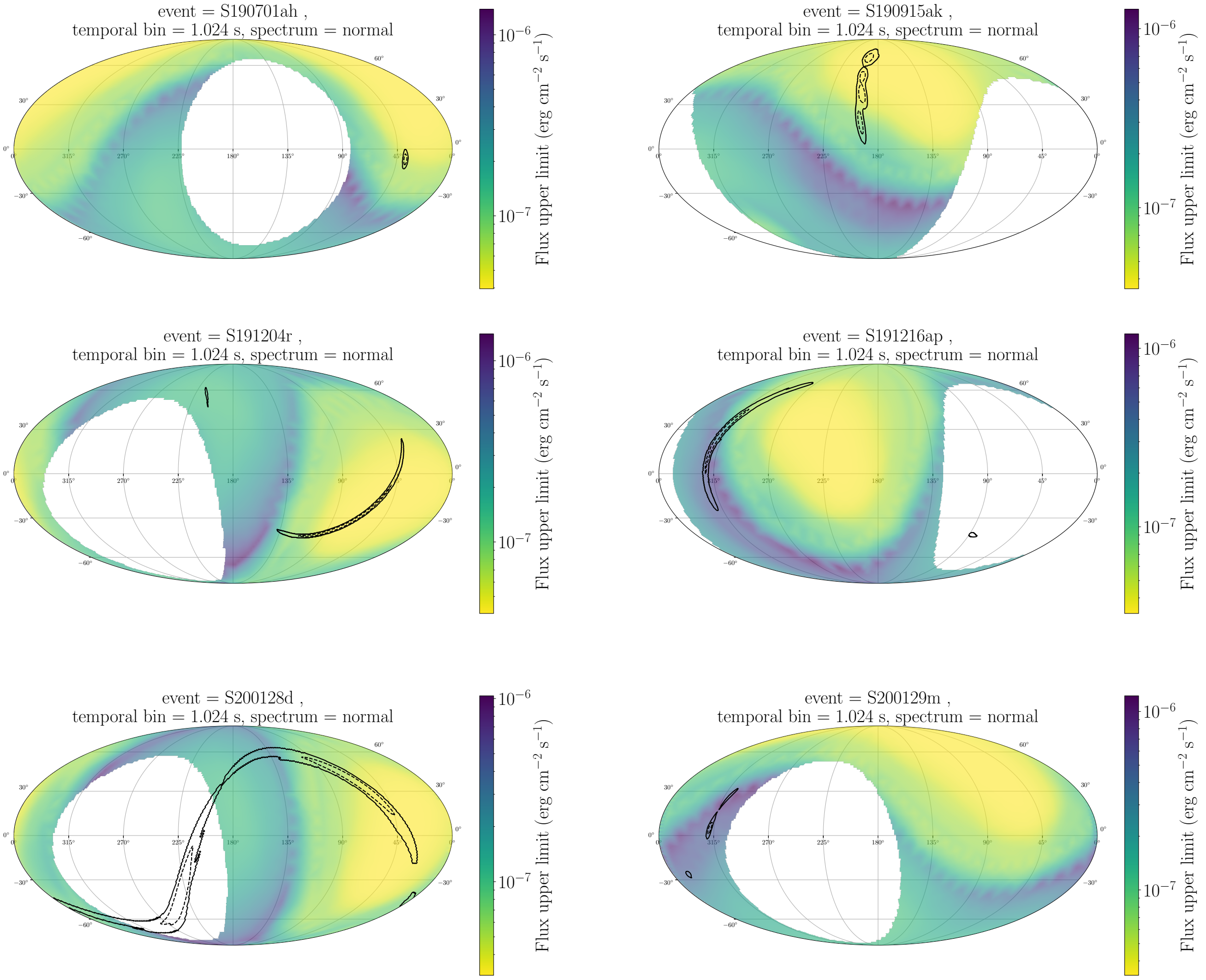
event = S190701ah , temporal bin = 1.024 s, spectrum = normal

event = S190915ak , temporal bin = 1.024 s, spectrum = normal

event = S191204r , temporal bin = 1.024 s, spectrum = normal

event = S191216ap , temporal bin = 1.024 s, spectrum = normal

event = S200128d , temporal bin = 1.024 s, spectrum = normal

event = S200129m , temporal bin = 1.024 s, spectrum = normal

Figure 3. Flux upper limit maps are shown for all the O3 catalog events with a $p_{\rm astro} > 0.5$ that were processed successfully using NITRATES. The color bar indicates the upper limit in the 15–350 keV *Swift*-BAT band as a function of the sky position. The part of the sky in white corresponds to the area covered by the Earth. The solid and dashed contours are the GW 90% and 50% credible levels, respectively.

results are reported assuming a Normal spectral template.

Calling $\Omega = ({\rm RA}, {\rm Dec})$ the coordinates variable, for each temporal bin and spectral template we convert the upper limit map $\phi_{\rm UL}(\Omega)$ into a unique marginalized upper limit value:

$$\phi_{\rm UL} = \int_{\Omega \notin \Omega_\oplus} \phi_{\rm UL}(\Omega) P_{\rm GW}(\Omega) {\rm d}\Omega, \qquad (3)$$

where $P_{\rm GW}(\Omega)$ is the posterior probability distribution of the GW sky position. The notation $\Omega \notin \Omega_\oplus$ means that the integral is limited to the region of the sky not occulted by the Earth. We report in Table 1 the marginalized flux upper limits for a 1 s time bin, assuming the normal spectral template. In Fig. 3, we provide the sky maps reporting both the flux upper limits as a function of sky position and the GW contours (50% and 90% credible levels) for the GW candidates with $p_{\rm astro} > 0.5$.

As additional information, we also report the quantity $\varepsilon_{\rm in\,BAT}$, which quantifies the probability that the GW source is inside the BAT coded FOV and corresponds to

$$\varepsilon_{\rm in\,BAT} = \int_{\Omega \in \Omega_{\rm in}} P_{\rm GW}(\Omega) {\rm d}\Omega, \qquad (4)$$

where the integral is limited to the solid angle $\Omega_{\rm in}$, namely the portion of the sky where the BAT partial coding fraction is larger than 0.01. The location of $\Omega_{\rm in}$, i.e., the BAT FOV, is identified by the yellow region in the sky maps of Figure 3. The higher the $\varepsilon_{\rm in\,BAT}$, the better the BAT covering of the GW error region, and the more constraining the derived upper limit. The flux

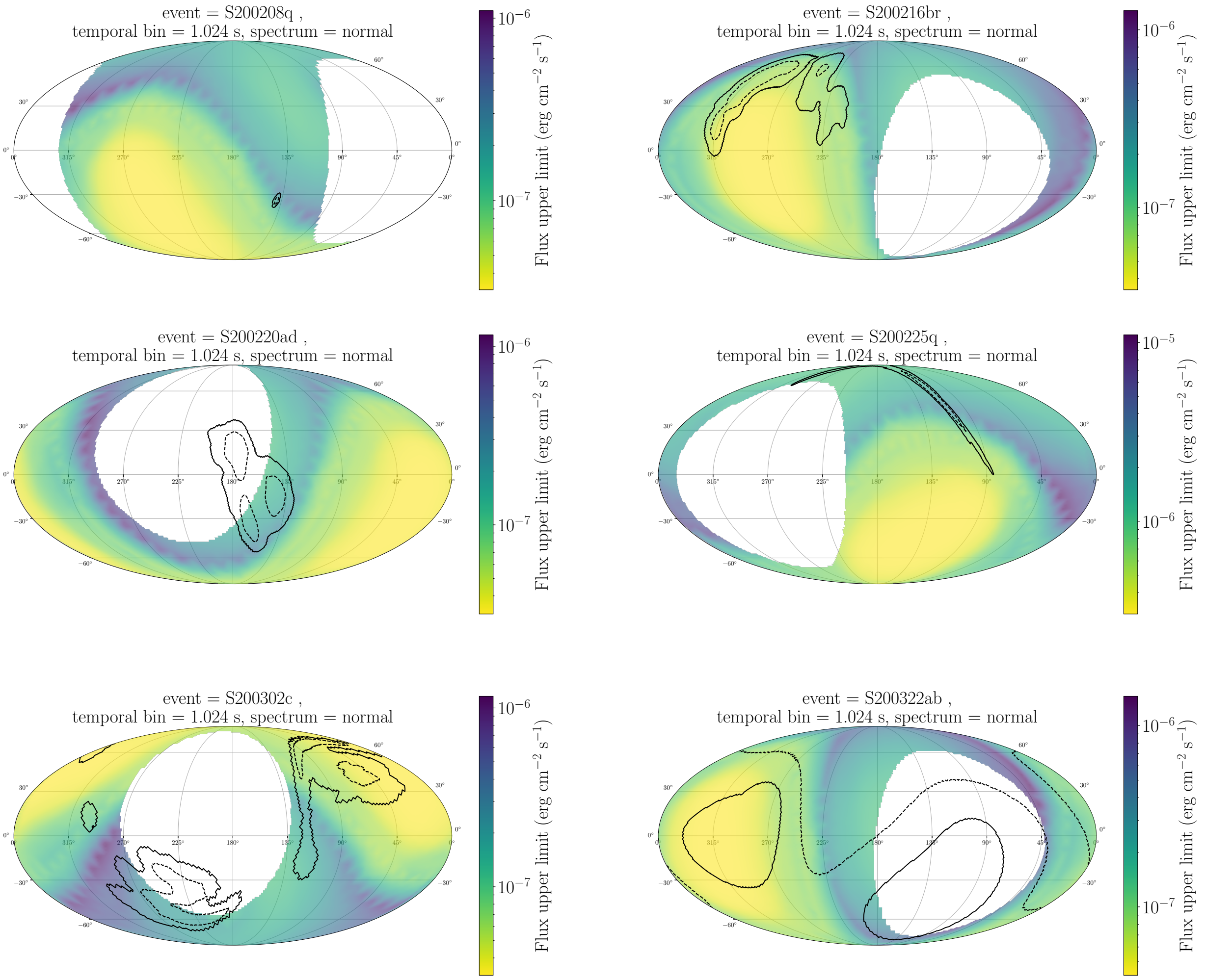

Figure 3. (continued)

upper limits as a function of $\varepsilon_{\text{in BAT}}$ for all GW trigger candidates is shown in Fig. 4. We also indicate with different markers the sample of low-latency triggers, the confirmed list of subthreshold candidates ($p_{\text{astro}} < 0.5$), and the above-threshold candidates ($p_{\text{astro}} > 0.5$). In Table 1 we also report the probability that the GW source is occulted by the Earth, defined as:

$$\varepsilon_{\oplus} = \int_{\Omega \in \Omega_{\oplus}} P_{\text{GW}}(\Omega) \mathrm{d}\Omega, \tag{5}$$

where $\Omega_{\oplus}$ is the solid angle subtended by the Earth from the *Swift* reference system.

5.3. *Computation of luminosity upper limits*

We further convert the flux upper limits into luminosity upper limits for all the GW triggers with available information about the distance posterior distribution, namely only triggers identified by CBC searches. The luminosity upper limit in the rest frame band 1 keV–10 MeV is estimated as

$$L_{\text{UL}} = \langle 4\pi D_{\text{L}}^2 k \phi_{\text{UL}} \rangle, \tag{6}$$

where D_{L} is extracted from the posterior probability $P(D_{\text{L}})$ reported in the GW sky localization files, while k is the k-correction and corresponds to

$$k = \frac{I[1\,\text{keV}/(1+z), 10\,\text{MeV}/(1+z)]}{I[15\,\text{keV}, 350\,\text{keV}]}, \tag{7}$$

where

$$I[a, b] = \int_a^b E \frac{\mathrm{d}N}{\mathrm{d}E}(E) \mathrm{d}E, \tag{8}$$

and $\mathrm{d}N/\mathrm{d}E$ is the assumed photon spectrum. The band 1 keV–10 MeV is chosen since it is usually adopted to report the bolometric luminosity of GRBs.

The luminosity upper limits as a function of the mean value of the luminosity distance is reported in Figure 5. Similar to what was shown previously, we demarcate the

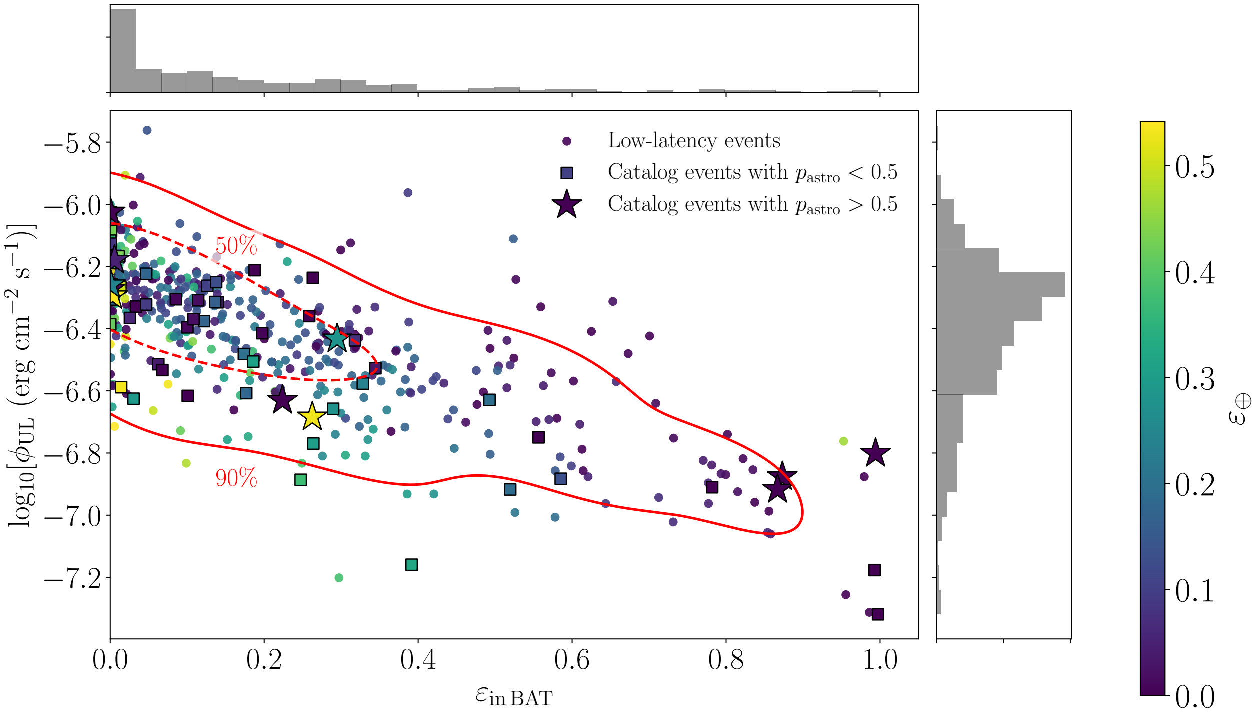

Figure 4. The 15–350 keV flux upper limit $\phi_{\rm UL}$ derived with NITRATES as a function of $\varepsilon_{\rm in\,BAT}$, namely the probability that the GW candidate is contained inside the BAT FOV. The plot includes all the GW candidates received during O3, including both Burst and CBC events. With different symbols we distinguish the GW candidates received in low latency and the ones confirmed and included in the O3 catalog, separated in $p_{\rm astro} > 0.5$ and $p_{\rm astro} < 0.5$. The dashed and solid red lines are the 50% and 90% containment regions of the scatter plot, respectively. The one-dimensional histograms of $\phi_{\rm UL}$ and $\varepsilon_{\rm in\,BAT}$ are reported on the sides. The color bar indicates the value of $\varepsilon_{\oplus}$, the probability that the GW candidate is occulted by the Earth.

various samples. Candidates with a low latency classification of Mass Gap were later re-distributed to other categories as part of post-processing, which is evident from the Mass Gap panel in Figure 5. As expected and as evident already from Figure 4, we see a clear correlation between the luminosity upper limit and $\varepsilon_{\rm in\,BAT}$ in Figure 5, indicating that the inferred constraints on the EM counterpart are more stringent when the GW probability integrated inside the BAT FOV is higher. Since $\phi_{\rm UL}$ is an upper limit and not a measure coming from a detection, Eq. (6) is an approximated method to convert $\phi_{\rm UL}$ in a luminosity upper limit, averaging over the $P(D_{\rm L})$ distribution provided by the GW analysis. In Appendix A we show a more accurate way to estimate the luminosity upper limit, but we find no relevant differences with respect to the method reported in this section. The Eq. (6) is used only to produce the plots of Fig. 5, but this approximation is not used in Section 6 to perform inference about the EM model parameters. Instead, in Section 6 a reverse process is followed, namely the EM model is used to predict the luminosity, which is then convolved with $P(D_{\rm L})$ to obtain a probability distribution of the flux in the BAT energy band.

5.4. *Computation of joint FAR*

To calculate the joint GW–BAT FARs for each GW trigger, we elaborate on the methods used to compute the individual FARs and subsequently combine them. To derive the sensitivity of the NITRATES search, time-tagged event data assembled from intervals corresponding to calibration runs and data from before and after known GRB signal times (total exposure time of ∼51 ks) were analyzed. The behavior of the background population and its associated FAR were then identified (see Section 7.6 and Fig. 16 in DeLaunay & Tohuvavohu 2022). We further compute the joint *Swift*-BAT–GW FAR by combining the BAT FAR (calculated using the method described above) with the GW FAR. A targeted joint FAR threshold routine is constructed as part of the Rapid, on-source VOEvent Coincident Monitor (RAVEN; Abbott et al. 2017c; Urban 2016), which combines the FARs obtained from GWs along with those from BAT and computes the joint temporal as well as the joint spatial FAR. We also specify details of the search pipeline used in the process, Burst or CBC. The joint FAR prescription as reported in the RAVEN doc-

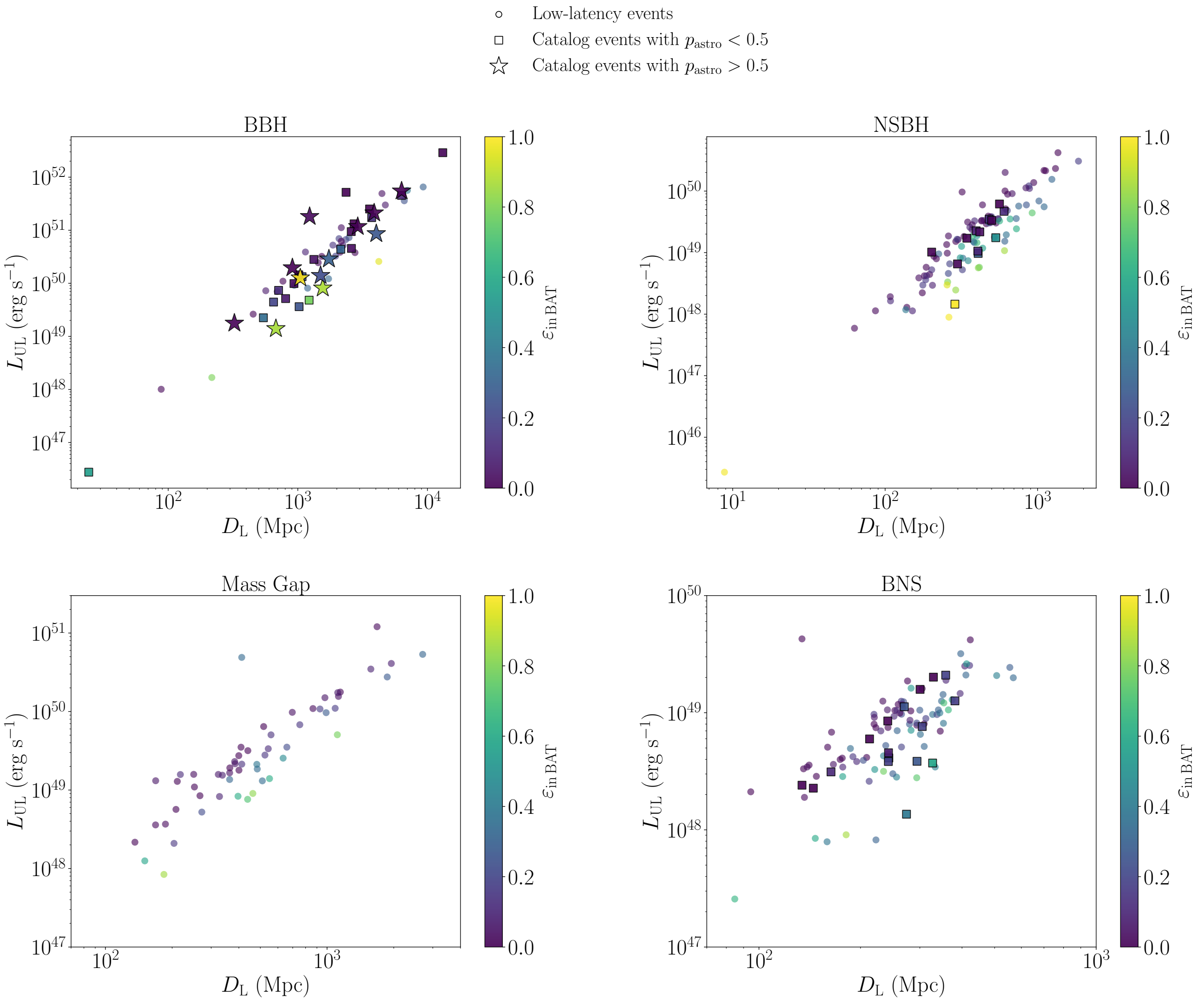

Figure 5. Upper limits on the luminosity computed in the rest frame 1 keV–10 MeV energy band, as a function of the mean luminosity distance extracted from the sky localization map of each GW candidate. The color bar indicates the quantity $\varepsilon_{\rm in\,BAT}$, namely the probability that the GW candidate is located inside the BAT coded FOV. With different symbols, we distinguish the GW candidates received in low latency and the ones confirmed and included in the O3 catalog, separated in $p_{\rm astro} > 0.5$ and $p_{\rm astro} < 0.5$.

umentation,[6] is computed as

$$\mathrm{FAR}_{\rm GRB+GW} = \frac{Z}{I_\Omega}\left[1+\ln\left(\frac{Z_{\rm max}}{Z}\right)\right] \tag{9}$$

where Z is the joint ranking statistic given by,

$$Z = \mathrm{FAR}_{\rm GW}\mathrm{FAR}_{\rm GRB}\Delta t, \tag{10}$$

$$Z_{\rm max} = \mathrm{FAR}_{\rm GW,max}\mathrm{FAR}_{\rm GRB,max}\Delta t, \tag{11}$$

and we adopt $\Delta t = 30$ s, $\mathrm{FAR}_{\rm GW,max} = 2$ day^{-1} and $\mathrm{FAR}_{\rm GRB,max} = 10^{-3}$ Hz. I_Ω is an integral that quantifies the spatial overlap between the GW localization and the GRB localization (Ashton et al. 2018). Even if the search of subthreshold candidates in NITRATES is done in a temporal window $[t_0 - 20$ s, $t_0 + 20$ s$]$ around the trigger time t_0, for the RAVEN joint alert the adopted temporal window is $[t_0 - 10$ s, $t_0 + 20$ s$]$. Since none of the BAT candidates analyzed in this work has a confident estimation of the sky localization, we adopt a uniform posterior probability on the full sky for the EM candidate. Hence, by definition, we set $I_\Omega = 1$. The candidate triggers a RAVEN alert when the $\mathrm{FAR}_{\rm GRB+GW} \times N_t < \mathrm{FAR}_{\rm max}$, with N_t being the trials factor of the joint search and $\mathrm{FAR}_{\rm max} = (1/30)$ day^{-1} for CBC events and $\mathrm{FAR}_{\rm max} = 1$ yr^{-1} for Burst events. The trials factor corresponds to $N_t = S_{\rm GW}(S_{\rm GW} - 1)$, where $S_{\rm GW}$ is the number of search GW pipelines, 4

---

[6] https://lscsoft.docs.ligo.org/raven/joint_far.html

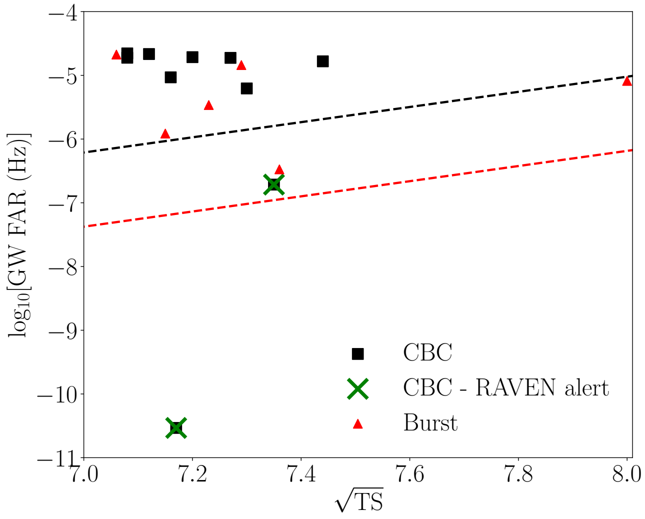

Figure 6. Distribution in the GW FAR–$\sqrt{\mathrm{TS}}$ plane of all the triggers which passed the threshold $\mathrm{FAR_{GRB}} < 10^{-3}$ Hz. Triggers in the regions below the black and red dashed lines (marked with a green cross) would have triggered the RAVEN alert system, for CBC and Burst events, respectively. The plot does not include all the triggers that have a $\sqrt{\mathrm{TS}} > 8$ which turned out to be spurious artifacts.

for CBC events and 3 for Burst events. Since the GW pipelines are not fully independent, a realistic value of the trials factor is smaller than the one adopted here, therefore the RAVEN threshold can be considered as a conservative estimate for the significance of a joint detection.

We quote the derived joint FARs along with other trigger-specific details only for those triggers with a $\mathrm{FAR_{GRB,max}} < 10^{-3}$ Hz in Table 4. We find that, after rejecting false positives, 2 CBC events pass the joint FAR detection threshold to trigger a RAVEN alert. Specifically, S191110x ($\sqrt{\mathrm{TS}} = 7.2$) and S200108p ($\sqrt{\mathrm{TS}} = 7.4$) have a joint FAR of 3.02×10^{-4} yr^{-1} and 21.3 yr^{-1}, respectively. These values are obtained considering the GW FAR received with the low-latency alert. In the offline analysis of the GW candidates, neither S191110x or S200108p have been confirmed. We therefore conclude that, considering the offline joint analysis of GW and *Swift*-BAT data, none of the candidates is eligible to claim a significant joint detection.

In Fig. 6 we report the location in the GW FAR - $\sqrt{\mathrm{TS}}$ plane of all the candidates that pass the condition $\mathrm{FAR_{GW,max}}$ <2 day^{-1} and $\mathrm{FAR_{GRB,max}} < 10^{-3}$ Hz (i.e., $\sqrt{\mathrm{TS}} \gtrsim 7$), to be considered for a potential joint alert. The astrophysical origin of all the candidates with $\sqrt{\mathrm{TS}} > 8$ has been rejected as discussed in Section 5.1, and therefore they are not reported in Fig. 6. The dashed black and red lines mark the separation line for the event to pass the RAVEN alert threshold, for CBC and Burst candidates, respectively. Candidates below those lines would have triggered a RAVEN alert.

6. SCIENCE DISCUSSION

In this section, we describe how the upper limits derived from the joint subthreshold search can be used to infer constraints about possible EM emission from the GW candidates. Starting from a model of the EM emission, the luminosity in the BAT band can be estimated, whose value will depend on some internal parameters of the model $(\lambda_1, ..., \lambda_k)$. The goal is to explore the model parameter space and test if the estimated flux is in agreement with the upper limit constraints derived in this paper.

For this purpose, a knowledge of the distance of the GW candidate is needed, and the GW sky localization is used to extract the posterior distribution $P(D_\mathrm{L})$. Since only CBC events have such information, Burst events are not considered in this discussion. For the CBC events, we consider a phenomenological model which describes the probability distribution of the luminosity L (in the 15–350 keV rest-frame)

$$P(L) = (1 - f)\delta(L = 0) + f\Pi(L). \tag{12}$$

Here, the f parameter is a proxy for the EM-bright nature of the event, i.e., given a CBC source described by a set of GW parameters $\vec{\theta}_\mathrm{GW}$, $f(\vec{\theta}_\mathrm{GW})$ corresponds to the probability that the EM luminosity of the source is nonzero. On the other hand, $\Pi(L)$ is the intrinsic luminosity function of the EM transient associated with the specific CBC class. In the case of BNS and NSBH candidates, the assumption on $\Pi(L)$ should be informed by our prior knowledge of the luminosity function of merger-driven GRBs. A detailed study of the impact of this work on our knowledge of merger-driven GRBs luminosity function will be reported in a follow-up paper. In this section, instead, we focus only on the BBH class, for which no strong prior exists for $\Pi(L)$. For simplicity and in order to show the constraining power of our joint subthreshold search, we assume that the EM process associated with BBH, if present, produces a universal, viewing angle-independent luminosity L_0. Therefore, in the scenario specified above, we have $(\lambda_1, ..., \lambda_k) = (f, L_0)$ and

$$P(L) = (1 - f)\delta(L = 0) + f\delta(L - L_0) = P(L; f, L_0). \tag{13}$$

Once the model for the EM emission is specified, the probability distribution of the predicted flux is

$$P(\phi) = (1 - f)\delta(\phi = 0) + fP_\mathrm{EM}(\phi), \tag{14}$$

where $P_{\rm EM}(\phi) = P(L_0/4\pi k D_{\rm L}^2)$ is the flux probability distribution in the assumption that the source is EM bright. Hence, for the i-th candidate, the probability that the predicted flux is below the estimated upper limit $\phi_{0,i}$ corresponds to

$$P_i(\phi < \phi_{0,i}) = (1-f) + f\int_0^{\phi_{0,i}} P_i(\phi){\rm d}\phi, \qquad (15)$$

valid in the limit in which the GW candidate is assumed to be real. Therefore, given a candidate GW with a probability of being astrophysical $p_{{\rm astro},i} = \pi_i$, there are only three possibilities to have a non-detection in BAT:

1. The source is not astrophysical, with a probability $1-\pi_i$;

2. The source is astrophysical, but it is occulted by the Earth, with a probability $\pi_i\varepsilon_\oplus$;

3. The source is astrophysical, it is not occulted by the Earth and the predicted flux by the EM model is below the BAT upper limit, with a probability $\pi_i(1-\varepsilon_\oplus)P_i(\phi < \phi_{0,i})$.

This allows us to define a non-detection likelihood corresponding to

$$\mathcal{L}_i = (1-\pi_i) + \pi_i[\varepsilon_\oplus + (1-\varepsilon_\oplus)P_i(\phi < \phi_{0,i})]. \qquad (16)$$

In the case of $L_0 \to 0$, $P_i(\phi < \phi_{0,i}) \to 1$, so $\mathcal{L}_i \to 1$. For very large values of L_0, instead, $P_i(\phi < \phi_{0,i}) \to 0$ and therefore $\mathcal{L}_i \to (1-\pi_i) + \pi_i\varepsilon_\oplus$. This last result shows how, even if the luminosity predicted by the model is exceedingly large, a non-detection can occur if the GW source is not real $(1-\pi_i)$, or if it is real but occulted by the Earth $(\pi_i\varepsilon_\oplus)$. Since the analysis is focused only on BBH events, we consider only those candidates that have $p_{\rm BBH} > p_{\rm NSBH}, p_{\rm BNS}$. By definition, $p_{\rm BBH} + p_{\rm NSBH} + p_{\rm BNS} = p_{\rm astro}$ and typically for the candidates classified as BBH we have that $p_{\rm BBH} \gg p_{\rm NSBH}, p_{\rm BNS}$. The last condition allows us to consider Eq. (16) still valid if we replace π_i with $p_{{\rm BBH},i}$, since the contribution of $p_{{\rm NSBH},i}$ and $p_{{\rm BNS},i}$ to the non-detection probability is negligible.

Given the definition of Eq. (16), $\mathcal{L}_i$ indicates the probability, given a set of $(\lambda_1, ..., \lambda_k)$ EM parameters, that the BAT upper limit is not violated, taking into account the possible non-astrophysical origin of the candidate and also the probability that, even if astrophysical, the source is occulted by the Earth and therefore not detectable by *Swift*. Having a collection of $E_1, ..., E_N$ GW candidates, the posterior distribution of the model parameters can be obtained following the Bayes theorem

$$\begin{aligned} &P(L_0, f|E_1, ..., E_N) \qquad (17)\\ &= \prod_{i=1}^{N}\mathcal{L}_i\pi(L_0)\pi(f)\Big/\int\prod_{i=1}^{N}\mathcal{L}_i\pi(L_0)\pi(f){\rm d}L_0{\rm d}f, \end{aligned}$$

where $\pi(L_0)$ and $\pi(f)$ are the prior distributions of L_0 and f. We assume a log-uniform prior for both L_0 and f in the respective intervals $46 < \log_{10}[L_0({\rm erg\ s^{-1}})] < 53$ and $-3 < \log_{10}(f) < 0$. The choice of the prior boundaries are poorly informed by theoretical expectations, which are still affected by large uncertainties. Instead, the priors are chosen on the basis of the typical range of upper limit luminosity derived in this work for BBH events and the total number of candidates considered in this analysis. The constraints reported in the following may strongly depend on the choice of the prior boundaries. Therefore, the final goal of this simulation, more than deriving strong limits on the putative EM model, is to show the predictive power of the present analysis in the context of model inference and how this analysis can improve with the addition of more GW events in the future.

In the specific case of our simulation, we consider all the GW candidates released in GWTC-3 (Abbott et al. 2023), including both the above threshold ($p_{\rm astro} > 0.5$) and the subthreshold ($p_{\rm astro} < 0.5$) candidates. For the latter, we emphasize that the classification of the CBC candidate as BBH merger is valid under the condition that the subthreshold GW event is of astrophysical origin. The simulation described in this section is set up in such a way that this assumption is taken into account for the final constraints of the physical parameters. All the low-latency candidates not confirmed by the offline analysis are not included in the simulation. The considered BBH sample with full NITRATES results and available flux upper limits consists of 32 events, 12 of which with $p_{\rm astro} > 0.5$.

In order to compute numerically the functional behavior of the likelihood, we set up a simulation to evaluate $P(L_0, f|E_1, ..., E_N)$ in the full $[L_0, f]$ plane defined by the prior boundaries. The details of the simulation setup are reported in Appendix B. The results of the simulation for the sample of above threshold BBH candidates are reported in Fig. 7, where the color map indicates the value of $\mathcal{L} = \prod\mathcal{L}_i$, normalized by the maximum $\max(\mathcal{L})$ over the full domain. The contour levels defining the 50% and 90% exclusion regions are reported as well. For comparison, in Fig. 7 we include also the same contour levels obtained with an analysis that considers all the BBH candidates without imposing any cut on the $p_{\rm astro}$. The level of constraining power of the anal-

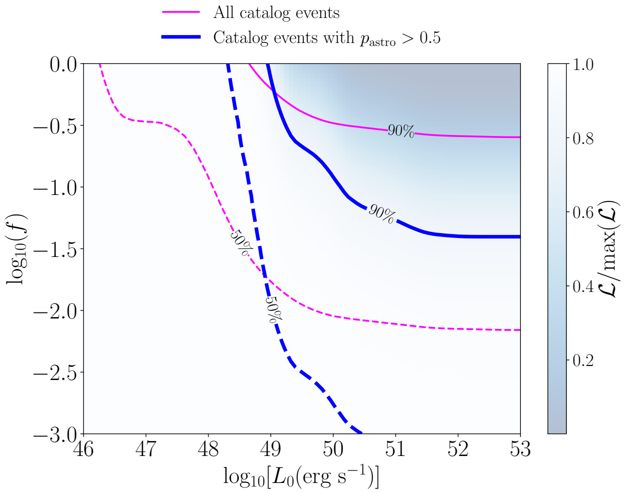

Figure 7. Constraints on the two parameters L_0 and f of the model for the putative EM counterpart of BBH mergers. The color map reports the likelihood $\mathcal{L}$, for the full analysis including all the O3 catalog events with $p_{\rm astro} > 0.5$. L_0 is in units of erg s^{-1}. The thick blue solid and dashed contours indicate the exclusion regions in the $[L_0, f]$ plane at 90% and 50% credibility levels, respectively. The magenta solid and dashed lines report the same contours, but for an analysis that includes all O3 catalog events, with no cut in $p_{\rm astro}$.

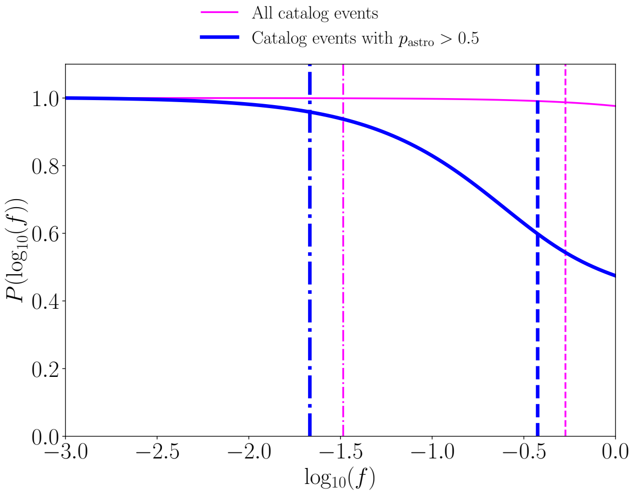

Figure 8. Posterior distribution of $\log_{10}(f)$, including the 50% and 90% upper limits with dot-dashed and dashed lines, respectively. The function is derived from Fig. 7, marginalizing over L_0.

ysis can be quantified by defining the fraction of the full parameter space excluded with a credibility level η, corresponding to:

$$R_\eta = I_\eta / I_{\rm tot}, \tag{18}$$

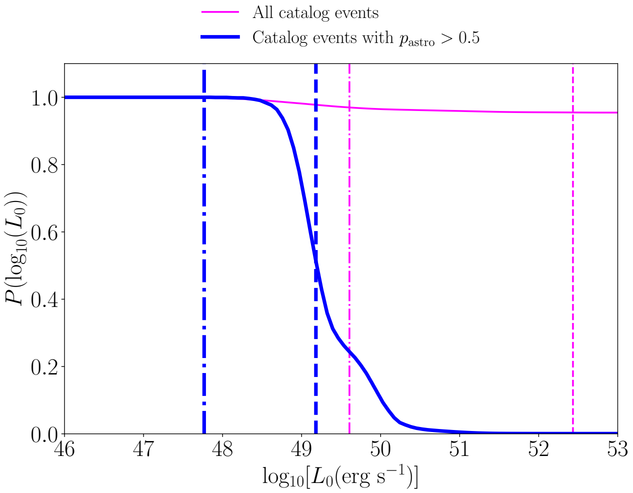

Figure 9. Posterior distribution of $\log_{10}(L_0)$, including the 50% and 90% upper limits with the dot-dashed and dashed lines, respectively. The function is derived from Fig. 7, marginalizing over f.

where $I_{\rm tot} = \int {\rm d}f{\rm d}L_0$, being the integral extended to the full parameters domain, and with

$$I_\eta = \int_S {\rm d}f{\rm d}L_0, \tag{19}$$

corresponding to the dimension of the region S of the parameter space excluded with a credibility level η. The analysis performed using only BBH with $p_{\rm astro} > 0.5$ gives a $R_{90\%} = 22\%$, while the analysis performed with the inclusion of subthreshold BBH candidates gives $R_{90\%} = 10\%$. This result indicates that with the inclusion of GW subthreshold events the analysis allows us to exclude a smaller portion of the parameter space, with respect to an analysis carried out using only events with high $p_{\rm astro}$. Therefore, even adding further information with the inclusion of more GW events, if these last are likely originated by noise, the full Bayesian analysis is affected by more uncertainty, resulting in an overall less constraining power of the analysis.

Figs. 8 and 9 report the posterior distribution of $P(f)$ and $P(L_0)$, respectively, obtained as:

$$P(f) = \int P(L_0, f|E_1, ..., E_N){\rm d}L_0 \tag{20}$$

and

$$P(L_0) = \int P(L_0, f|E_1, ..., E_N){\rm d}f. \tag{21}$$

Both $P(L_0)$ and $P(f)$ are normalized such that $\max[P(L_0)] = \max[P(f)] = 1$. The posterior is reported in magenta and blue for both samples, with and without cut in $p_{\rm astro}$, respectively. The 50% and 90% upper limits are reported as well. From the shape of the posteriors and the values of the 50% and 90% upper limits, it is evident that both the L_0 and f posteriors only slightly differ from the flat priors, if no cut in $p_{\rm astro}$ is applied. On the other hand, for the above threshold sample, the analysis is more informative and more stringent constraints on the parameters can be obtained, especially for L_0. For the sample with $p_{\rm astro} > 0.5$, the 50% and 90% upper limits for f are $\log_{10}(f_{50\%}) = -1.67$ and $\log_{10}(f_{90\%}) = -0.42$, while for L_0 are $\log_{10}[L_{0,50\%}({\rm erg\ s^{-1}})] = 47.8$ and $\log_{10}[L_{0,90\%}({\rm erg\ s^{-1}})] = 49.2$, respectively.

In the limit of a collection of triggers which correspond only to non-astrophysical events, i.e., all with $\pi_i = 0$, the likelihood is constant in the full parameter space, not allowing to infer any constraints on the EM model parameters. On the other hand, if we increase the fraction of confident GW events and we keep fixed the total number N, their distance distribution $P(D_{\rm L})$ and the derived upper limits, then we obtain that $\mathcal{L}$ decreases accordingly. This implies that increasing the number of events with π_i close to 1, the overall exclusion region in the $(\lambda_1, ..., \lambda_k)$ parameter space increases as well. This demonstrates that with the collection of more data, in the limit of a GW detector horizon constant in time, this method allows us to improve incrementally our constraints on the EM models of CBC events. Although, realistically the GW detection horizon will increase with time (Abbott et al. 2020), implying an overall increase of the median values of $D_{\rm L}$ of the candidate events. Such an effect increases in turn the values of the luminosity upper limits, increasing as well the values of $P_i(\phi < \phi_0)$ and hence of $\mathcal{L}$. This effect tends to decrease the dimension of the exclusion region of the $(\lambda_1, ..., \lambda_k)$ parameter space. Overall, the final outcome of the inclusion of additional GW data, in terms of the constraining power of this analysis, will depend on the simultaneous combined effect of increasing the number of confident events and of increasing the detection horizon.

In order to show how the inclusion of more significant GW candidates can improve the constraining power of the present analysis, we carried out the following simulation. We repeated the same procedure adopted to produce the exclusion regions of Fig. 7, but replacing the real π_i with $\pi_i = 1$ for all the confirmed BBH candidates, hence imposing that they are all significant events. All the values of $\phi_{\rm UL}$, $\varepsilon_\oplus$ and $P(D_{\rm L})$ of each candidate are left unchanged. The resulting 50% and 90% exclusion regions are reported in Fig. 10, with black dashed and solid lines, respectively. The fraction of the 90% excluded region increases to a value of $R_{90\%} = 17\%$, clearly demonstrating that, even if the BAT flux upper limit are the same, the increase of confidence about the astrophysical nature of the GW improves our final constraints on the model parameter space. Furthermore, Fig. 10 reports also the 50% and 90% exclusion regions (with red dashed and solid lines, respectively), obtained as before, but imposing both $\pi_i = 1$ and $\varepsilon_\oplus = 0$ for each candidate. This combination corresponds to simulate all real BBH candidates, whose sky localization does not overlap with the sky region covered by the Earth. In this case $R_{90\%} = 35\%$, showing that also the fraction of GW sky posterior occulted by Earth has a significant impact on our final results.

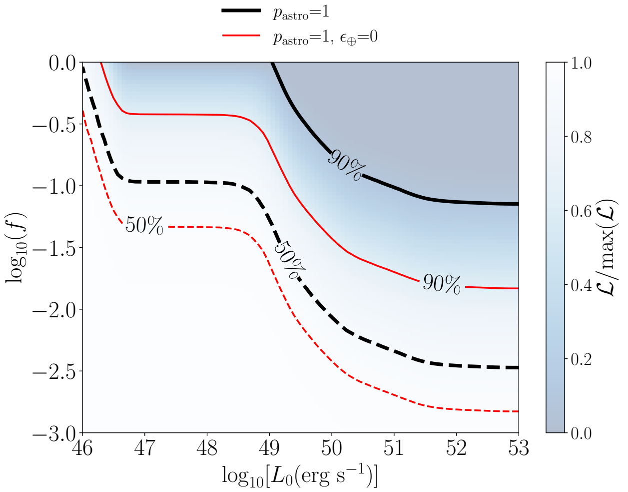

Figure 10. Same as Fig. 7, but simulating all the O3 catalog candidates with an associated $p_{\rm astro} = \pi_i = 1$. The black dashed and solid lines identify the 50% and 90% exclusion regions, respectively. The red dashed and solid lines have the same meaning, but derived imposing both $\pi_i = 1$ and $\varepsilon_\oplus = 0$.

7. CONCLUSIONS

In this work we report the systematic search of signals jointly detected by the LIGO–Virgo interferometers and the *Swift*-BAT telescope, during the third LVK observing run. Thanks to the prompt availability of BAT data using GUANO and the sensitive targeted search capabilities of the NITRATES pipeline, we conducted deep follow-up searches for EM signals on a sample of 636 GW triggers. The search results did not yield any confident joint detection, allowing us to derive upper limits in the 15–350 keV band. We provide comprehensive details on all analyzed GW triggers along with their NITRATES search statistics. This information can be valuable for calibrating and comparing with other offline targeted search pipelines that are currently operational or may be developed in the future.

In the specific case of the BBH class, the BAT flux upper limits have been used to perform a stacking analysis and to derive constraints on the possible nature of an associated EM emission. As illustrated in Section 6, the presence of several BBH candidates with large values of $p_{\rm astro}$ in our sample, enhances our ability to better constrain the parameter space for EM emission from BH mergers, with minimal assumptions on our prior knowledge of the nature of the emission. The prospect of detecting EM emission from BBH mergers has been debated and discussed in detail in recent times. Particularly, the GBM trigger that accompanied the first BBH merger event, GW150914, has served as a case study to test possible association and potential implications (Abbott et al. 2016b; Connaughton et al. 2016; Goldstein et al. 2016b). Though not likely, there are a number of physical models that have been proposed that could give rise to detectable emission in the gamma-ray band. A summary of the various different models has been discussed in Fletcher et al. (2023) and Veres et al. (2019). The models involve parameters pertaining to potential remnant accretion effects, magnetic field strength, black hole charge and spin, among others (e.g., Loeb 2016; Dai et al. 2017; Woosley 2016; Zhang 2016). The method described in Section 6 can be easily extended to any of these models, provided that the luminosity function $\Pi(L)$ of the putative BBH EM emission is known. Additionally, effects possibly related to the viewing angle dependency of the EM emission can be easily included in this approach. Regarding CBCs containing at least one NS (BNS and NSBH), it was not possible to conduct a similar stacking analysis as the one described for BBH in Section 6, due to the paucity of such events with a large enough value of $p_{\rm astro}$. Further observations, including the fourth LVK observing run (O4), could lead to the collection of a larger number of BNS and NSBH candidates with moderate values of $p_{\rm astro}$, giving the possibility to repeat the analysis performed in this paper and to derive informative constraints on the EM emission of these classes and the properties of the associated GRB populations. Data products associated with the present analysis are reported in a separate data release.[7]

O4 commenced on the 24th of May, 2023. The number of significant detections is expected to increase by several times during the entire duration of O4 (Abbott et al. 2018; Petrov et al. 2022). Targeted search results using the GUANO-NITRATES infrastructure are publicly available in real-time[8]. In the case of non-detection of an EM counterpart, the GUANO team reports the 15–350 keV flux upper limit for all the GW triggers classified as *significant*, via GCN Circulars. Additional enhancements to the likelihood search code have reduced the search latency by a factor of 2, with respect to O3.

Thanks to its sensitivity in the hard X-ray band and the possibility to localize EM transients down to a precision of an arcminute, *Swift* represents one of the main discovery machines for the detection of EM counterparts of GW transients. This paper shows how the GUANO infrastructure has a deep impact on the multi-messenger science case, in particular for optimally exploiting the sensitivity of the *Swift*-BAT instrument for the detection of EM counterparts of CBCs detected by the LVK Collaboration. The deep subthreshold search enabled by the NITRATES pipeline sensibly increases the detection horizon of *Swift*, giving the chance to detect transients also outside the BAT FOV and allowing us to possibly detect faint X-ray/gamma-ray transients associated to relativistic jets observed off-axis, as in the case of GW170817. In the case of a confident joint *Swift*-GW detection, the GUANO team will promptly disseminate all the information about the EM candidate via GCN Circulars, providing an estimate of the sky localization when available. Moreover, also in the case of non-detection, this paper shows how the upper limits derived from the NITRATES analysis can be combined to have the most sensitive constraints on the EM emission from all the CBC classes. The cumulative collection of non-detection will gradually improve our knowledge of the EM nature of CBCs.

ACKNOWLEDGMENTS

Gayathri Raman, Samuele Ronchini, and Jamie Kennea acknowledge the support of NASA grants 80NSSC19K0408 and 80NSSC22K1498 awarded as part of the NASA Neil Gehrels Swift Observatory Guest Investigator program. Jamie Kennea and James Delaunay acknowledge the support of NASA contract NAS5-0136.

This material is based upon work supported by NSF's LIGO Laboratory which is a major facility fully funded by the National Science Foundation. The authors also gratefully acknowledge the support of the Science and Technology Facilities Council (STFC) of the United Kingdom, the Max-Planck-Society (MPS), and the State of Niedersachsen/Germany for support of the construction of Advanced LIGO and construction and operation of the GEO 600 detector. Additional support for Advanced LIGO was provided by the Australian Research Council. The authors gratefully acknowledge the Italian Istituto Nazionale di Fisica Nucleare (INFN), the French Centre National de la Recherche Scientifique (CNRS) and the Netherlands Organization for Scientific Research (NWO), for the construction and operation of the Virgo detector and the creation and sup-

---

[7] https://doi.org/10.5281/zenodo.10600302

[8] https://guano.swift.psu.edu

port of the EGO consortium. The authors also gratefully acknowledge research support from these agencies as well as by the Council of Scientific and Industrial Research of India, the Department of Science and Technology, India, the Science & Engineering Research Board (SERB), India, the Ministry of Human Resource Development, India, the Spanish Agencia Estatal de Investigación (AEI), the Spanish Ministerio de Ciencia, Innovación y Universidades, the European Union NextGenerationEU/PRTR (PRTR-C17.I1), the ICSC - CentroNazionale di Ricerca in High Performance Computing, Big Data and Quantum Computing, funded by the European Union NextGenerationEU, the Comunitat Autonòma de les Illes Balears through the Direcció General de Recerca, Innovació i Transformació Digital with funds from the Tourist Stay Tax Law ITS 2017-006, the Conselleria d'Economia, Hisenda i Innovació, the FEDER Operational Program 2021-2027 of the Balearic Islands, the Conselleria d'Innovació, Universitats, Ciència i Societat Digital de la Generalitat Valenciana and the CERCA Programme Generalitat de Catalunya, Spain, the National Science Centre of Poland and the European Union – European Regional Development Fund; Foundation for Polish Science (FNP), the Polish Ministry of Science and Higher Education, the Swiss National Science Foundation (SNSF), the Russian Science Foundation, the European Commission, the European Social Funds (ESF), the European Regional Development Funds (ERDF), the Royal Society, the Scottish Funding Council, the Scottish Universities Physics Alliance, the Hungarian Scientific Research Fund (OTKA), the French Lyon Institute of Origins (LIO), the Belgian Fonds de la Recherche Scientifique (FRS-FNRS), Actions de Recherche Concertées (ARC) and Fonds Wetenschappelijk Onderzoek – Vlaanderen (FWO), Belgium, the Paris Île-de-France Region, the National Research, Development and Innovation Office Hungary (NKFIH), the National Research Foundation of Korea, the Natural Science and Engineering Research Council Canada, Canadian Foundation for Innovation (CFI), the Brazilian Ministry of Science, Technology, and Innovations, the International Center for Theoretical Physics South American Institute for Fundamental Research (ICTP-SAIFR), the Research Grants Council of Hong Kong, the National Natural Science Foundation of China (NSFC), the Leverhulme Trust, the Research Corporation, the National Science and Technology Council (NSTC), Taiwan, the United States Department of Energy, and the Kavli Foundation. The authors gratefully acknowledge the support of the NSF, STFC, INFN and CNRS for provision of computational resources.

This work was supported by MEXT, JSPS Leading-edge Research Infrastructure Program, JSPS Grant-in-Aid for Specially Promoted Research 26000005, JSPS Grant-in-Aid for Scientific Research on Innovative Areas 2905: JP17H06358, JP17H06361 and JP17H06364, JSPS Core-to-Core Program A. Advanced Research Networks, JSPS Grant-in-Aid for Scientific Research (S) 17H06133 and 20H05639 , JSPS Grant-in-Aid for Transformative Research Areas (A) 20A203: JP20H05854, the joint research program of the Institute for Cosmic Ray Research, University of Tokyo, National Research Foundation (NRF), Computing Infrastructure Project of Global Science experimental Data hub Center (GSDC) at KISTI, Korea Astronomy and Space Science Institute (KASI), and Ministry of Science and ICT (MSIT) in Korea, Academia Sinica (AS), AS Grid Center (ASGC) and the National Science and Technology Council (NSTC) in Taiwan under grants including the Rising Star Program and Science Vanguard Research Program, Advanced Technology Center (ATC) of NAOJ, and Mechanical Engineering Center of KEK.

Additional acknowledgements for support of individual authors may be found in the following document: `https://dcc.ligo.org/LIGO-M2300033/public`. For the purpose of open access, the authors have applied a Creative Commons Attribution (CC BY) license to any Author Accepted Manuscript version arising. We request that citations to this article use 'A. G. Abac *et al.* (LIGO-Virgo-KAGRA Collaboration), ...' or similar phrasing, depending on journal convention.

Matplotlib (Hunter 2007), SEABORN (Waskom 2021), NumPy (Harris et al. 2020) and SciPy (Virtanen et al. 2020) were used in the preparation of the manuscript.

REFERENCES

Abbott B. P., et al., 2016a, Physical Review X, 6, 041015

Abbott B. P., et al., 2016b, PhRvL, 116, 061102

Abbott B. P., et al., 2017a, PhRvL, 119, 161101

Abbott B. P., et al., 2017b, Nature, 551, 85

Abbott B. P., et al., 2017c, ApJ, 841, 89

Abbott B. P., et al., 2017d, ApJL, 848, L12

Abbott B. P., et al., 2017e, ApJL, 848, L13

Abbott B. P., et al., 2018, Living Reviews in Relativity, 21, 3

Abbott B. P., et al., 2020, Living Reviews in Relativity, 23, 3

Abbott R., et al., 2021, PhRvX, 11, 021053

Abbott R., et al., 2023, PhRvX, 13, 041039

Abbott R., et al., 2024, PhRvD, 109, 022001

Alexander K. D., et al., 2017, ApJL, 848, L21

Allison J., et al., 2016, Nuclear Instruments and Methods in Physics Research A, 835, 186

Arcavi I., et al., 2017, Nature, 551, 64

Ashton G., et al., 2018, ApJ, 860, 6

Aubin F., et al., 2021, Classical and Quantum Gravity, 38, 095004

Band D., et al., 1993, ApJ, 413, 281

Barthelmy S. D., et al., 2005, SSRv, 120, 143

Bauswein A., Just O., Janka H.-T., Stergioulas N., 2017, ApJL, 850, L34

Connaughton V., et al., 2016, ApJL, 826, L6

Coulter D. A., et al., 2017, Science, 358, 1556

Cowperthwaite P. S., et al., 2017, ApJL, 848, L17

Dai L., McKinney J. C., Miller M. C., 2017, MNRAS, 470, L92

Dal Canton T., Nitz A. H., Gadre B., Cabourn Davies G. S., Villa-Ortega V., Dent T., Harry I., Xiao L., 2021, ApJ, 923, 254

DeLaunay J., Tohuvavohu A., 2022, ApJ, 941, 169

DeLaunay J., Tohuvavohu A., Kennea J., 2020, General Coordinates Network, 27444, 1

DeLaunay J., Tohuvavohu A., Kennea J. A., Raman G., 2021a, General Coordinates Network, 30130, 1

DeLaunay J., Tohuvavohu A., Kennea J. A., Raman G., 2021b, General Coordinates Network, 30302, 1

DeLaunay J., Tohuvavohu A., Raman G., Kennea J. A., 2022a, General Coordinates Network, 31402, 1

DeLaunay J., Tohuvavohu A., Raman G., Kennea J. A., 2022b, General Coordinates Network, 31402, 1

DeLaunay J., Tohuvavohu A., Ronchini S., Raman G., Kennea J. A., Parsotan T., 2023, General Coordinates Network, 34747, 1

Drout M. R., et al., 2017, Science, 358, 1570

Evans P. A., et al., 2017, Science, 358, 1565

Fermi GBM Team 2020, General Coordinates Network, 26944, 1

Fletcher C., et al., 2023, arXiv e-prints, p. arXiv:2308.13666

Gehrels N., et al., 2004, ApJ, 611, 1005

Goldstein A., Burns E., Hamburg R., Connaughton V., Veres P., Briggs M. S., Hui C. M., The GBM-LIGO Collaboration 2016a, arXiv e-prints, p. arXiv:1612.02395

Goldstein A., Burns E., Hamburg R., Connaughton V., Veres P., Briggs M. S., Hui C. M., The GBM-LIGO Collaboration 2016b, arXiv e-prints, p. arXiv:1612.02395

Goldstein A., et al., 2017a, ApJL, 848, L14

Goldstein A., et al., 2017b, ApJL, 848, L14

Hallinan G., et al., 2017, Science, 358, 1579

Hamburg R., et al., 2020, ApJ, 893, 100

Harris C. R., et al., 2020, Nature, 585, 357

Hooper S., Chung S. K., Luan J., Blair D., Chen Y., Wen L., 2012, PhRvD, 86, 024012

Hotokezaka K., Nakar E., Gottlieb O., Nissanke S., Masuda K., Hallinan G., Mooley K. P., Deller A. T., 2019, Nature Astronomy, 3, 940

Hughes S. A., Holz D. E., 2003, Classical and Quantum Gravity, 20, S65

Hunter J. D., 2007, Computing in Science & Engineering, 9, 90

Hurley K., et al., 2020, General Coordinates Network, 26949, 1

Klimenko S., Mohanty S., Rakhmanov M., Mitselmakher G., 2005, PhRvD, 72, 122002

Klimenko S., et al., 2016, PhRvD, 93, 042004

Kyutoku K., Shibata M., Taniguchi K., 2021, Living Reviews in Relativity, 24, 5

Loeb A., 2016, ApJL, 819, L21

Margutti R., Chornock R., 2021, ARA&A, 59, 155

Margutti R., et al., 2017, ApJL, 848, L20

Messick C., et al., 2017, PhRvD, 95, 042001

Nakar E., 2020a, PhR, 886, 1

Nakar E., 2020b, PhR, 886, 1

Nissanke S., Holz D. E., Dalal N., Hughes S. A., Sievers J. L., Hirata C. M., 2013, arXiv e-prints, p. arXiv:1307.2638

Nitz A. H., Dal Canton T., Davis D., Reyes S., 2018, PhRvD, 98, 024050

Nitz A. H., Nielsen A. B., Capano C. D., 2019, ApJL, 876, L4

Ossokine S., et al., 2020, PhRvD, 102, 044055

Petrov P., et al., 2022, ApJ, 924, 54

Pian E., et al., 2017, Nature, 551, 67

Pillas M., et al., 2023, arXiv e-prints, p. arXiv:2306.04373

Pratten G., et al., 2021, PhRvD, 103, 104056

Radice D., Perego A., Zappa F., Bernuzzi S., 2018, ApJL, 852, L29

Sachdev S., et al., 2019, arXiv e-prints, p. arXiv:1901.08580

Salafia O. S., Ravasio M. E., Ghirlanda G., Mandel I., 2023, A&A, 680, A45

Savchenko V., et al., 2017, ApJL, 848, L15

Schutz B. F., 1986, Nature, 323, 310

Singer L. P., Price L. R., 2016, PhRvD, 93, 024013

Singer L. P., et al., 2016, ApJL, 829, L15

Smartt S. J., et al., 2017, Nature, 551, 75

Tanvir N. R., et al., 2017, ApJL, 848, L27

Tohuvavohu A., 2023, General Coordinates Network, 33132, 1

Tohuvavohu A., Kennea J. A., DeLaunay J., Palmer D. M., Cenko S. B., Barthelmy S., 2020, ApJ, 900, 35

Tohuvavohu A., Raman G., DeLaunay J., Kennea J. A., 2021a, General Coordinates Network, 31049, 1

Tohuvavohu A., Raman G., DeLaunay J., Kennea J. A., 2021b, General Coordinates Network, 31049, 1

Tohuvavohu A., DeLaunay J., Raman G., Kennea J. A., 2022a, General Coordinates Network, 32167, 1

Tohuvavohu A., DeLaunay J., Raman G., Kennea J. A., 2022b, General Coordinates Network, 32375, 1

Troja E., et al., 2017, Nature, 551, 71

Urban A. L., 2016, PhD thesis, University of Wisconsin, Milwaukee

Veres P., Dal Canton T., Burns E., Goldstein A., Littenberg T. B., Christensen N., Preece R. D., 2019, ApJ, 882, 53

Villar V. A., et al., 2017, ApJL, 851, L21

Virtanen P., et al., 2020, Nature Methods, 17, 261

Wang H., Giannios D., 2021, ApJ, 908, 200

Waskom M. L., 2021, Journal of Open Source Software, 6, 3021

Woosley S. E., 2016, ApJL, 824, L10

Zhang B., 2016, ApJL, 827, L31

APPENDIX

A. LUMINOSITY UPPER LIMIT

A more accurate method to derive the luminosity upper limit should be based on the knowledge of $P(D_{\rm L})$ and $P(\phi)$, where ϕ is the flux measured in the BAT energy band. Having only an upper limit, $P(\phi)$ can be approximated as

$$P(\phi) \propto \begin{cases} \Pi(\phi), & \phi < \phi_{\rm UL} \\ 0, & \phi > \phi_{\rm UL} \end{cases}, \tag{A1}$$

where $\Pi(\phi)$ is our prior distribution for the flux. Using the conversion from flux to luminosity $L = 4\pi D_{\rm L}^2\phi$, the probability distribution of the luminosity can be computed as

$$P(L) = P(4\pi D_{\rm L}^2\phi) \propto \int \frac{1}{\phi} P_\phi(\phi) P_{D_{\rm L}^2}\left(\frac{L}{4\pi\phi}\right) {\rm d}\phi, \tag{A2}$$

where P_ϕ is the flux probability distribution and $P_{D_{\rm L}^2}$ is the probability distribution of $D_{\rm L}^2$. In the conversion from flux to luminosity, the k-correction has been omitted, since it introduces a mild dependence on the redshift, which is not relevant for the purposes of this section. The 5σ luminosity upper limit $L_{\rm UL}$ can be found imposing that

$$\int_0^{L_{\rm UL}} P(L){\rm d}L = 1 - \varepsilon_{5\sigma}, \tag{A3}$$

with $\varepsilon_{5\sigma} = 3 \times 10^{-7}$. The value of $L_{\rm UL}$ has been computed adopting two different assumptions for the flux prior, corresponding to $\Pi(\phi) \propto$ const. and $\Pi(\phi) \propto \phi^{-3/2}$, with the latter being inspired by the usual trend followed by GRBs (e.g., Salafia et al. 2023). In both cases, we find that $L_{\rm UL} \sim 3 \times 4\pi\langle D_{\rm L}^2\rangle\phi_{\rm UL}$.

B. SIMULATION SETUP

In this section we specify the details of the simulation used to compute numerically the $\mathcal{L}(L_0, f|E_1, ..., E_N)$ function. For each simulated GW candidate, the single $\mathcal{L}_i$ is computed for each pairs of values $(L_{0,n}, f_m)$. The flux predicted by the EM model is predicted injecting 1000 sources whose luminosity distance is distributed according to $P(D_{\rm L})$, derived from the GW localization. The probability $P_i(\phi < \phi_{0,i})$ is derived computing the fraction of cases that have a flux below the sky-averaged BAT upper limit, defined by Eq. (3). The computation of $\mathcal{L}$ is performed on a 100×100 grid of $(L_{0,n}, f_m)$. Once the previous steps are performed for all the GW candidates, the final combined likelihood is computed as

$$\mathcal{L}(L_0, f|E_1, ..., E_N) = \prod_i \mathcal{L}_i(L_0, f). \tag{B4}$$

In order to produce the credibility contours in the $[L_{0,n}, f_m]$ plane, we adopt the following steps:

1. $\mathcal{L}$ is normalized such that
$$\sum_{n,m} \mathcal{L}(L_{0,n}, f_m) = 1. \tag{B5}$$
2. A one-dimensional array $\mathcal{L}[x_n]$ is created flattening the two-dimensional grid $\mathcal{L}(L_{0,n}, f_m)$, then $\mathcal{L}[x_n]$ is sorted in ascending order.
3. We find the element $[\hat{L}_0, \hat{f}] = [x_{n^*}]$ such that
$$\sum_{n=0}^{n^*} \mathcal{L}[x_n] = \lambda, \tag{B6}$$
where λ is the credibility level of the contour.
4. The contour is drawn imposing $\mathcal{L} = \mathcal{L}(\hat{L}_0, \hat{f})$.

C. FLUX UPPER LIMIT DERIVATION

In this appendix we show an alternative method to compute the non-detection likelihood presented in Section 6. The NITRATES analysis allows us to derive a flux upper limit at a given confidence level for each pixel of the GW sky localization, corresponding to the function $\phi_{\rm UL}({\rm RA}, {\rm Dec})$ defined in Eq. (3). Then combined probability of being located in the pixel x_i and to have a non-detectable EM emission is

$$P(\text{non-det}, x_i) \propto P_{\rm GW}(x_i) P[\phi < \phi_{\rm UL}(x_i)] \Delta\Omega_i, \tag{C7}$$

where

$$P[\phi < \phi_{\rm UL}(x_i)] = (1-f) + f \int_0^{\phi_{\rm UL}(x_i)} P(\phi|x_i) {\rm d}\phi, \tag{C8}$$

and $\Delta\Omega_i$ is the area of the pixel. Here we express $P(\phi|x_i)$ as the conditional flux probability distribution, namely the flux probability distribution assuming that the GW source is contained in the pixel x_i. To compute the $P(\phi|x_i)$, for a fixed luminosity L, the luminosity distance is extracted from the the conditional probability distribution $P(D_{\rm L}|x_i)$, which is derived from the GW sky localization. Finally the overall non-detection probability is obtained integrating Eq. (C7) over the full sky:

$$P(\text{non-det}|f, L_0) = \sum_{x_i} P_{\rm GW}(x_i) P[\phi < \phi_{\rm UL}(x_i)] \Delta\Omega_i = (1-f) + f \left[\varepsilon_\oplus + \sum_{x_i \notin \Omega_\oplus} P_{\rm GW}(x_i) \Delta\Omega_i \int_0^{\phi_{\rm UL}(x_i)} P(\phi|x_i) {\rm d}\phi\right], \tag{C9}$$

where we have used that

$$\int_0^{\phi_{\rm UL}(x_i)} P(\phi|x_i) {\rm d}\phi = 1 \text{ if } x_i \in \oplus, \quad \text{and} \sum_{x_i \in \Omega_\oplus} P_{\rm GW}(x_i) \Delta\Omega_i = \varepsilon_\oplus. \tag{C10}$$

The resulting probability of non-detecting any EM emission in correspondence to a GW trigger with a given $p_{\rm astro} = \pi_i$ is

$$P(\text{non-det}|f, L_0, \pi_i) = (1-\pi_i) + \pi_i P(\text{non-det}|f, L_0). \tag{C11}$$

Eq. (C9) has to be compared with the method used in Section 6, where instead we used the approximation:

$$P(\text{non-det}|f, L_0) = (1-f) + f \int_0^{\phi_{\rm UL}} P(\phi) {\rm d}\phi, \tag{C12}$$

with

$$\phi_{\rm UL} = \int_{\Omega \notin \Omega_\oplus} \phi_{\rm UL}(\Omega) P_{\rm GW}(\Omega) {\rm d}\Omega, \tag{C13}$$

and $P(\phi)$ is obtained extracting $D_{\rm L}$ from the full sky marginalized distribution $P(D_{\rm L})$, corresponding to

$$P(D_{\rm L}) = \sum_{x_i} P_{\rm GW}(x_i) P(D_{\rm L}|x_i) \Delta\Omega_i. \tag{C14}$$

The two methods give comparable results in the assumption that the following approximation is valid:

$$\int_0^{\phi_{\rm UL}} P(\phi) {\rm d}\phi \approx \varepsilon_\oplus + \sum_{x_i \notin \Omega_\oplus} P_{\rm GW}(x_i) \Delta\Omega_i \int_0^{\phi_{\rm UL}(x_i)} P(\phi|x_i) {\rm d}\phi. \tag{C15}$$

For completeness, we clarify here the main differences in the two methods.

METHOD 1:

This is the method used in Section 6 and is based on the following steps:

1. The marginalized upper limit $\phi_{\rm UL}$ is computed over the full sky, weighting by the GW sky localization.
2. Once L_0 is fixed, the flux probability distribution $P(\phi)$ is computed extracting randomly $D_{\rm L}$ from the $P(D_{\rm L})$, the latter corresponding to the posterior distribution of the GW luminosity distance, marginalized over the full sky (excluding the part occulted by the Earth).
3. The integral $\int_0^{\phi_{\rm UL}} P(\phi) {\rm d}\phi$ which appears in Eq. (C12) is evaluated counting the fraction of simulated events that have a predicted flux below the sky-averaged upper limit $\phi_{\rm UL}$.

METHOD 2:

This is the method presented in this appendix and summarized by Eqs. (C9) and (C11), consisting in the following procedure:

1. A set of sources is injected in space and the distribution follows the volumetric probability distribution of the GW candidate. First the coordinates of the injected source are extracted from the sky localization $P_{\rm GW}({\rm RA},{\rm Dec})$, then for each position the distance is extracted according to the conditional probability $P(D_{\rm L}|{\rm RA},{\rm Dec})$.

2. For each injected source, once the luminosity L_0 is fixed, the predicted flux is compared with the coordinates-dependent BAT upper limit map $\phi_{\rm UL}({\rm RA},{\rm Dec})$.

3. We define $\rho_{\notin\oplus}$ the fraction of all the sources injected which are not occulted by the Earth and also have a predicted flux below $\phi_{\rm UL}({\rm RA},{\rm Dec})$. Given this definition, we have:

$$\sum_{x_i\notin\Omega_\oplus} P_{\rm GW}(x_i)\Delta\Omega_i \int_0^{\phi_{\rm UL}(x_i)} P(\phi|x_i){\rm d}\phi = (1-\varepsilon_\oplus)\rho_{\notin\oplus}. \tag{C16}$$

The last equality can be justified considering that, if for each pixel i we inject $N_{{\rm tot},i}$ sources, we can define $\rho_i = N_{{\rm ND},i}/N_{\rm tot,i}$, where $N_{{\rm ND},i}$ is the fraction of injected sources that are not detected, i.e., with a predicted flux below $\phi_{\rm UL}(x_i)$. Therefore:

$$\int_0^{\phi_{\rm UL}(x_i)} P(\phi|x_i){\rm d}\phi = \rho_i. \tag{C17}$$

Let us call $N_{\rm tot}$ the total number of sources injected on the full sky. Then we have

$$N_{\rm tot,i} = N_{\rm tot} P_{\rm GW}(x_i)\Delta\Omega_i, \tag{C18}$$

and therefore

$$\sum_{x_i\notin\Omega_\oplus} P_{\rm GW}(x_i)\Delta\Omega_i \int_0^{\phi_{\rm UL}(x_i)} P(\phi|x_i){\rm d}\phi = \sum_{x_i\notin\Omega_\oplus} \frac{N_{{\rm tot},i}}{N_{\rm tot}}\rho_i = \frac{1}{N_{\rm tot}} \sum_{x_i\notin\Omega_\oplus} N_{{\rm ND},i}. \tag{C19}$$

Since the total number of injected sources not occulted by Earth are $N_{{\rm tot},\notin\oplus} = (1-\varepsilon_\oplus)N_{\rm tot}$, and using that

$$\rho_{\notin\oplus} = \frac{1}{N_{{\rm tot},\notin\oplus}} \sum_{x_i\notin\Omega_\oplus} N_{{\rm ND},i}, \tag{C20}$$

we finally recover Eq. (C16).

In order to quantify the difference between the two methods, the following test is performed. Having fixed the two parameters f and L_0, we compute the likelihood $\mathcal{L}$ for the two methods and we derive the quantity

$$\varepsilon_\mathcal{L} = 2\frac{{\rm abs}(\mathcal{L}_1-\mathcal{L}_2)}{\mathcal{L}_1+\mathcal{L}_2}. \tag{C21}$$

Here we use the subscripts 1 and 2 for the respective methods. Both likelihoods are computed considering only BBH candidates with $p_{\rm astro} > 0.5$. In both cases, the total number of injected sources for each BBH candidate is $N_{\rm tot} = 1000$. The distribution of $\varepsilon_\mathcal{L}$ is evaluated sampling randomly f and L_0, for a total of 100 sampled pairs (f, L_0). We obtain that the median value of $\varepsilon_\mathcal{L}$ is 0.04 and that in $\sim 80\%$ of the sampled cases $\varepsilon_\mathcal{L} < 0.2$. Since the difference between the two methods is limited and since the Method 2 is more computationally expensive, all the results are used adopting Method 1.

Table 1. List of 636 low latency GW triggers analyzed using NITRATES is shown along with their respective $p_{\rm astro}$ values and 15–350 keV band flux upper limits. The maximum $\sqrt{\rm TS}$ is indicated for all the triggers with successful NITRATES results. Observations corresponding to triggers with insufficient exposure time during the BAT pointing mode do not have valid NITRATES results or flux upper limits. For those triggers that do have NITRATES results but fail to meet the criterion for a full likelihood analysis, the max $\sqrt{\rm TS}$ is indicated as NFL (No Final Likelihood). The GW triggers from the *Burst* pipeline do not have associated $p_{\rm astro}$ values and are therefore left blank. The fraction of the GW sky posterior distribution inside the BAT coded FOV and the fraction of the GW posterior occulted by the Earth are denoted by $\varepsilon_{\rm in\,BAT}$ and $\varepsilon_{\oplus}$, respectively.

SID	Time (UTC)	GW FAR (Hz)	group	$p_{\rm astro}$	Class	$\sqrt{\rm TS}$	Flux UL (erg cm^{-2} s^{-1})	$\varepsilon_{\rm in\,BAT}$ (%)	$\varepsilon_{\oplus}$ (%)
S190701ah	2019-07-01T20:33:07	1.92×10^{-8}	CBC	0.934	BBH	6.4	1.58×10^{-7}	99.42	0
S190816i	2019-08-16T13:04:31	1.44×10^{-8}	CBC	0.833	NSBH	-	-	-	-
S190828af	2019-08-28T17:51:02	1.83×10^{-5}	CBC	0.012	BNS	-	-	-	-
S190829p	2019-08-29T13:49:01	2.59×10^{-6}	CBC	0.062	Mass Gap	5.8	2.05×10^{-7}	58.03	0.94
S190830y	2019-08-30T15:07:04	7.70×10^{-8}	CBC	0.382	Mass Gap	5.7	1.45×10^{-7}	78.14	5.94
S190831ai	2019-08-31T18:31:02	8.85×10^{-6}	CBC	0.064	NSBH	5.7	8.38×10^{-7}	1.46	41.91
S190901al	2019-09-01T21:01:03	8.78×10^{-6}	CBC	0.015	NSBH	6.6	1.82×10^{-7}	80.18	1.08
S190901d	2019-09-01T02:56:47	1.01×10^{-5}	CBC	0.018	BNS	6.5	5.33×10^{-7}	13.86	43.34
S190901h	2019-09-01T04:38:54	5.26×10^{-6}	Burst	-	-	6.3	4.14×10^{-7}	24.56	43.03
S190902ao	2019-09-02T20:56:00	7.21×10^{-6}	CBC	0.016	NSBH	6.1	5.41×10^{-7}	9.78	24.09
S190904c	2019-09-04T02:59:52	3.64×10^{-6}	CBC	0.037	Mass Gap	5.2	5.35×10^{-7}	11.35	17.04
S190904p	2019-09-04T12:32:03	3.75×10^{-6}	CBC	0.026	NSBH	-	-	-	-
S190904w	2019-09-04T17:49:01	1.56×10^{-6}	Burst	-	-	5.8	4.53×10^{-7}	27.01	0
S190906ad	2019-09-06T18:33:04	1.41×10^{-5}	CBC	0.010	BNS	5.9	5.43×10^{-7}	15.61	46.69
S190906ag	2019-09-06T19:35:03	3.22×10^{-6}	Burst	-	-	5.5	5.73×10^{-7}	24.48	28.62
S190906ah	2019-09-06T20:05:00	8.90×10^{-7}	CBC	0.101	NSBH	5.7	5.47×10^{-7}	12.62	19.27
S190906s	2019-09-06T15:20:02	4.71×10^{-6}	Burst	-	-	6.4	3.65×10^{-7}	51.54	6.26
S190907n	2019-09-07T14:29:05	2.71×10^{-6}	Burst	-	-	NFL	5.91×10^{-7}	16.71	10.63
S190908az	2019-09-08T21:34:01	4.26×10^{-7}	Burst	-	-	5.7	7.04×10^{-7}	8.59	23.3
S190908e	2019-09-08T02:34:06	4.52×10^{-6}	Burst	-	-	5.5	2.50×10^{-7}	21.39	77.13
S190909ac	2019-09-09T14:13:01	4.54×10^{-6}	Burst	-	-	5.9	3.43×10^{-7}	16.23	21.97
S190909aw	2019-09-09T19:41:05	1.07×10^{-6}	Burst	-	-	5.8	2.29×10^{-7}	70.87	2.4
S190909bd	2019-09-09T21:26:03	8.85×10^{-6}	CBC	0.023	Mass Gap	-	-	-	-
S190909y	2019-09-09T12:49:01	1.66×10^{-6}	CBC	0.134	NSBH	-	-	-	-
S190915ak	2019-09-15T23:57:02	9.74×10^{-10}	CBC	0.990	BBH	5.4	1.33×10^{-7}	87.31	0.17
S190915q	2019-09-15T16:03:01	2.66×10^{-6}	Burst	-	-	5.8	4.81×10^{-7}	11.92	13.01
S190916y	2019-09-16T15:55:01	9.70×10^{-7}	CBC	0.143	BNS	6.9	5.58×10^{-7}	10.2	27.57
S190917ad	2019-09-17T19:14:00	1.47×10^{-5}	CBC	0.013	Mass Gap	6.4	4.47×10^{-7}	4.18	3.5
S190918aa	2019-09-18T19:38:04	6.68×10^{-7}	CBC	0.023	BNS	7.2	1.09×10^{-7}	64.36	16.27
S190919ag	2019-09-19T17:58:02	3.42×10^{-6}	Burst	-	-	7.2	2.77×10^{-7}	14.79	56.16
S190919ak	2019-09-19T18:34:03	1.06×10^{-5}	CBC	0.089	BNS	5.8	3.11×10^{-7}	28.36	35.45
S190919au	2019-09-19T20:39:00	3.24×10^{-6}	Burst	-	-	9.4	6.34×10^{-7}	0.04	42.88
S190919u	2019-09-19T12:13:02	8.18×10^{-6}	Burst	-	-	8.0	3.84×10^{-7}	20.56	23.68
S190920an	2019-09-20T19:09:05	2.77×10^{-7}	Burst	-	-	5.7	3.16×10^{-7}	15.6	36.74
S190920ap	2019-09-20T19:27:04	5.51×10^{-6}	Burst	-	-	5.8	2.95×10^{-7}	11.49	46.04
S190920z	2019-09-20T12:55:04	6.08×10^{-6}	Burst	-	-	6.1	1.02×10^{-7}	52.58	38.59
S190922ag	2019-09-22T15:22:01	2.89×10^{-6}	Burst	-	-	5.4	3.02×10^{-7}	50.45	9.47
S190922aq	2019-09-22T18:08:05	1.63×10^{-5}	CBC	0.013	Mass Gap	6.2	-	-	-
S190923aj	2019-09-23T17:04:04	1.91×10^{-7}	Burst	-	-	-	-	-	-
S190923ak	2019-09-23T17:06:03	2.70×10^{-6}	CBC	0.216	BBH	-	-	-	-
S190923x	2019-09-23T12:19:00	2.10×10^{-6}	CBC	0.036	BNS	-	-	-	-

S190923y	2019-09-23T12:55:59	4.78×10^{-8}	CBC	0.670	NSBH	-	-	-	-
S190926z	2019-09-26T16:47:02	1.27×10^{-6}	Burst	-	-	6.2	3.37×10^{-7}	1.81	72.24
S190927an	2019-09-27T14:58:00	3.60×10^{-6}	CBC	0.038	BNS	6.6	4.59×10^{-7}	0.02	58.85
S190928c	2019-09-28T02:11:45	6.73×10^{-9}	Burst	-	-	6.9	2.84×10^{-7}	0.04	1.53
S190928j	2019-09-28T06:30:16	2.51×10^{-6}	CBC	0.092	BNS	6.4	5.64×10^{-7}	8.9	27.8
S190930s	2019-09-30T13:35:41	3.00×10^{-9}	CBC	0.950	Mass Gap	-	-	-	-
S190930t	2019-09-30T14:34:07	1.54×10^{-8}	CBC	0.74	NSBH	5.9	5.15×10^{-7}	11.69	21.15
S191105d	2019-11-05T13:40:51	6.63×10^{-6}	Burst	-	-	-	-	-	-
S191106r	2019-11-06T18:41:51	3.31×10^{-6}	Burst	-	-	-	-	-	-
S191107o	2019-11-07T16:05:23	5.62×10^{-6}	Burst	-	-	5.6	6.00×10^{-7}	3.02	17.27
S191107t	2019-11-07T18:03:55	4.14×10^{-6}	CBC	0.020	NSBH	6.0	4.35×10^{-7}	0.06	17.98
S191110w	2019-11-10T16:48:32	4.43×10^{-6}	Burst	-	-	6.6	1.55×10^{-7}	27.57	47.27
S191110x	2019-11-10T18:08:42	2.93×10^{-11}	CBC	0.999	Mass Gap	7.2	1.75×10^{-7}	15.22	56.88
S191112n	2019-11-12T04:43:25	1.76×10^{-5}	Burst	-	-	5.3	1.09×10^{-6}	38.68	17.28
S191113aj	2019-11-13T14:28:49	2.31×10^{-5}	CBC	0.005	BNS	6.5	2.18×10^{-7}	16.07	0.01
S191114ad	2019-11-14T12:58:04	1.36×10^{-5}	CBC	0.065	BBH	6.0	2.05×10^{-7}	30.58	22
S191114am	2019-11-14T15:39:15	1.57×10^{-5}	CBC	0.021	BBH	6.3	5.12×10^{-7}	0	1.97
S191114at	2019-11-14T16:16:17	8.13×10^{-6}	CBC	0.008	NSBH	6.7	3.66×10^{-7}	15.85	50.49
S191115be	2019-11-15T23:07:27	1.05×10^{-5}	CBC	0.010	NSBH	6.0	9.94×10^{-7}	3	0.64
S191116ac	2019-11-16T14:21:55	9.04×10^{-6}	CBC	0.015	NSBH	NFL	4.95×10^{-7}	8.53	1.28
S191118n	2019-11-18T07:59:05	5.88×10^{-6}	CBC	0.018	NSBH	6.8	8.70×10^{-8}	85.8	6.04
S191118z	2019-11-18T16:49:55	7.31×10^{-7}	CBC	0.164	BNS	6.2	1.17×10^{-7}	38.57	54.47
S191121bf	2019-11-21T13:13:24	3.70×10^{-6}	Burst	-	-	-	-	-	-
S191121bq	2019-11-21T15:54:12	2.72×10^{-6}	Burst	-	-	5.7	2.73×10^{-7}	38.34	29.35
S191121bt	2019-11-21T16:45:42	2.03×10^{-5}	CBC	0.004	NSBH	5.5	3.06×10^{-7}	6.25	7.14
S191123q	2019-11-23T09:01:14	1.07×10^{-5}	Burst	-	-	5.4	5.84×10^{-7}	2.04	14.18
S191127p	2019-11-27T05:02:27	2.63×10^{-6}	CBC	0.037	Mass Gap	-	-	-	-
S191130q	2019-11-30T07:52:23	8.69×10^{-6}	CBC	0.005	NSBH	5.0	5.55×10^{-7}	1.24	28.9
S191202af	2019-12-02T18:42:26	2.36×10^{-6}	Burst	-	-	-	-	-	-
S191204o	2019-12-04T14:17:13	1.16×10^{-5}	CBC	0.009	NSBH	-	-	-	-
S191204r	2019-12-04T17:15:26	3.06×10^{-25}	CBC	1.000	BBH	NFL	1.21×10^{-7}	86.69	0
S191204t	2019-12-04T18:34:16	1.67×10^{-6}	Burst	-	-	5.1	3.73×10^{-7}	15.06	24.91
S191205ae	2019-12-05T20:56:37	2.83×10^{-7}	Burst	-	-	5.7	6.07×10^{-7}	7.73	3.8
S191205ah	2019-12-05T21:52:08	1.25×10^{-8}	CBC	0.932	NSBH	5.2	3.43×10^{-7}	31.7	7.85
S191206ab	2019-12-06T14:05:21	6.19×10^{-6}	CBC	0.024	Mass Gap	6.2	2.82×10^{-7}	34.03	8.59
S191206an	2019-12-06T17:38:57	1.01×10^{-6}	Burst	-	-	5.7	3.14×10^{-7}	5.28	7.69
S191207o	2019-12-07T10:16:32	1.42×10^{-5}	Burst	-	-	-	-	-	-
S191207u	2019-12-07T12:29:56	1.00×10^{-5}	Burst	-	-	6.1	3.61×10^{-7}	28.24	32.09
S191208b	2019-12-08T02:02:15	9.14×10^{-6}	CBC	0.017	BNS	5.0	4.92×10^{-7}	0.03	41.23
S191209ao	2019-12-09T13:58:21	1.02×10^{-6}	CBC	0.097	Mass Gap	5.6	4.34×10^{-7}	0.37	39.42
S191209ar	2019-12-09T14:32:42	1.08×10^{-6}	Burst	-	-	6.2	2.61×10^{-7}	56.27	8.52
S191212ad	2019-12-12T16:57:39	2.55×10^{-6}	Burst	-	-	7.0	5.43×10^{-6}	0.17	17.49
S191212ap	2019-12-12T19:59:21	1.31×10^{-6}	CBC	0.080	BNS	6.0	4.98×10^{-7}	0.67	4.94
S191212b	2019-12-12T00:31:07	9.49×10^{-6}	Burst	-	-	4.9	4.94×10^{-7}	7.29	39.35
S191212l	2019-12-12T07:57:05	9.31×10^{-6}	CBC	0.021	Mass Gap	7.2	4.24×10^{-7}	11.14	69.95
S191213al	2019-12-13T16:09:04	1.27×10^{-7}	CBC	0.518	NSBH	6.3	3.61×10^{-7}	16.31	35.94
S191213an	2019-12-13T16:58:32	8.60×10^{-7}	Burst	-	-	6.2	2.92×10^{-7}	50.3	30.27
S191213au	2019-12-13T18:44:42	7.84×10^{-7}	Burst	-	-	6.0	1.47×10^{-7}	9.88	87.84
S191213ay	2019-12-13T19:16:25	2.93×10^{-6}	Burst	-	-	6.3	5.88×10^{-7}	0.26	11.37
S191213be	2019-12-13T19:54:22	1.72×10^{-6}	Burst	-	-	5.6	6.80×10^{-7}	1.1	79.01

S191213c	2019-12-13T01:17:45	6.71×10^{-8}	CBC	0.395	NSBH	5.9	4.87×10^{-8}	98.61	0
S191215r	2019-12-15T19:57:29	5.46×10^{-6}	CBC	0.023	BNS	6.3	9.51×10^{-8}	73.13	12.09
S191216ap	2019-12-16T21:33:38	1.13×10^{-23}	CBC	1.000	Mass Gap	6.6	6.61×10^{-7}	0.56	4.99
S191219ak	2019-12-19T17:49:47	1.22×10^{-6}	Burst	-	-	7.2	1.40×10^{-7}	83.49	3.23
S191219an	2019-12-19T18:36:24	2.26×10^{-6}	Burst	-	-	6.0	4.64×10^{-7}	0.01	38.33
S191219ap	2019-12-19T19:52:52	3.14×10^{-6}	CBC	0.067	Mass Gap	6.3	3.05×10^{-7}	21.87	42.93
S191220af	2019-12-20T12:24:14	3.96×10^{-10}	CBC	0.996	BNS	6.4	4.93×10^{-7}	4.63	41.78
S191220al	2019-12-20T14:46:02	1.92×10^{-6}	CBC	0.026	BNS	-	-	-	-
S191220aw	2019-12-20T17:49:42	9.31×10^{-8}	CBC	0.522	NSBH	-	-	-	-
S191221aa	2019-12-21T10:31:37	1.02×10^{-5}	CBC	0.018	BNS	5.6	5.73×10^{-7}	52.7	1.74
S191221al	2019-12-21T14:41:21	2.92×10^{-6}	Burst	-	-	5.8	4.53×10^{-7}	5.41	24.69
S191221ar	2019-12-21T17:12:28	1.22×10^{-5}	CBC	0.011	NSBH	6.7	7.21×10^{-7}	0.72	7.38
S191221v	2019-12-21T08:51:06	1.43×10^{-6}	CBC	0.003	NSBH	6.3	1.33×10^{-7}	97.95	0
S191221w	2019-12-21T09:02:03	1.76×10^{-5}	CBC	0.055	Mass Gap	4.6	5.28×10^{-7}	8.91	6.08
S191222a	2019-12-22T01:34:42	8.95×10^{-6}	CBC	0.020	BNS	6.6	9.11×10^{-7}	0.03	13.45
S191222af	2019-12-22T13:57:46	1.94×10^{-5}	CBC	0.006	NSBH	-	-	-	-
S191222an	2019-12-22T16:30:03	1.79×10^{-5}	CBC	0.037	Mass Gap	-	-	-	-
S191223aj	2019-12-23T15:55:41	2.23×10^{-5}	CBC	0.006	BNS	5.9	2.57×10^{-7}	51.53	7.48
S191223p	2019-12-23T08:22:49	1.54×10^{-5}	CBC	0.008	NSBH	5.7	1.22×10^{-6}	3.89	6.33
S191224p	2019-12-24T05:03:59	8.31×10^{-6}	Burst	-	-	6.1	5.61×10^{-7}	10.96	17.7
S191224x	2019-12-24T11:23:11	1.98×10^{-5}	CBC	0.011	BNS	6.3	5.16×10^{-7}	22.09	8.42
S191225aq	2019-12-25T21:57:15	1.27×10^{-8}	CBC	0.390	Mass Gap	5.7	1.78×10^{-7}	55.64	0.05
S191225e	2019-12-25T02:11:26	9.64×10^{-6}	CBC	0.017	BNS	6.0	2.49×10^{-7}	37.71	36.13
S191225q	2019-12-25T10:30:40	1.69×10^{-5}	CBC	0.006	NSBH	6.0	4.39×10^{-7}	19.53	13.61
S191226ad	2019-12-26T13:31:05	1.19×10^{-5}	CBC	0.011	BNS	5.8	3.58×10^{-7}	9.16	13.79
S191226ae	2019-12-26T14:39:20	1.99×10^{-6}	CBC	0.026	NSBH	5.6	2.49×10^{-7}	21.45	4.19
S191226ai	2019-12-26T17:35:27	2.96×10^{-7}	CBC	0.602	BBH	-	-	-	-
S191226aj	2019-12-26T18:10:18	2.46×10^{-6}	CBC	0.073	Mass Gap	6.6	4.71×10^{-7}	0.26	65.36
S191226ap	2019-12-26T20:33:18	5.04×10^{-6}	Burst	-	-	6.0	4.36×10^{-7}	14.53	51.45
S191226d	2019-12-26T01:40:51	2.24×10^{-6}	Burst	-	-	5.7	4.80×10^{-7}	0.01	43.14
S191226u	2019-12-26T10:24:57	9.17×10^{-6}	Burst	-	-	-	-	-	-
S191227aa	2019-12-27T11:47:25	1.60×10^{-5}	CBC	0.006	NSBH	-	-	-	-
S191227af	2019-12-27T13:06:49	2.79×10^{-6}	Burst	-	-	6.6	9.85×10^{-8}	57.79	35.03
S191227aj	2019-12-27T14:54:31	5.45×10^{-6}	CBC	0.030	Mass Gap	5.9	2.56×10^{-7}	22.12	13.71
S191227al	2019-12-27T15:49:54	1.62×10^{-5}	CBC	0.010	BNS	6.2	2.71×10^{-7}	41.93	20.28
S191227am	2019-12-27T15:51:27	6.04×10^{-6}	Burst	-	-	-	-	-	-
S191227an	2019-12-27T16:10:45	8.60×10^{-6}	CBC	0.014	NSBH	6.3	7.13×10^{-7}	29.95	0.15
S191227ap	2019-12-27T16:35:12	1.68×10^{-5}	Burst	-	-	5.9	2.18×10^{-7}	44.6	27.51
S191227as	2019-12-27T17:29:03	1.32×10^{-5}	Burst	-	-	6.1	2.87×10^{-7}	21.77	35.26
S191227az	2019-12-27T21:55:49	1.21×10^{-5}	CBC	0.008	NSBH	6.9	5.10×10^{-7}	4.48	0.34
S191227bb	2019-12-27T23:04:40	3.86×10^{-7}	Burst	-	-	-	-	-	-
S191227h	2019-12-27T02:58:36	1.94×10^{-5}	CBC	0.034	BBH	6.5	8.67×10^{-7}	9.06	26.08
S191227o	2019-12-27T04:55:18	1.17×10^{-5}	Burst	-	-	6.8	5.77×10^{-7}	14.35	1.91
S191228ac	2019-12-28T13:17:16	1.44×10^{-5}	CBC	0.007	NSBH	7.0	2.43×10^{-7}	16.91	65.16
S191228am	2019-12-28T18:51:01	7.20×10^{-6}	Burst	-	-	-	-	-	-
S191228an	2019-12-28T20:07:11	1.83×10^{-6}	Burst	-	-	6.4	2.49×10^{-7}	48.48	0.41
S191228at	2019-12-28T23:57:39	8.92×10^{-6}	Burst	-	-	4.6	2.99×10^{-7}	36.08	31.05
S191228i	2019-12-28T05:44:50	2.27×10^{-5}	CBC	0.008	Mass Gap	6.5	3.47×10^{-7}	38.65	34.86
S191228q	2019-12-28T08:14:37	5.18×10^{-6}	Burst	-	-	5.8	4.05×10^{-7}	27.39	34.8
S191228u	2019-12-28T09:08:39	9.00×10^{-6}	Burst	-	-	5.4	4.01×10^{-7}	10.1	41.03

S191228w	2019-12-28T09:49:35	1.01×10^{-5}	Burst	-	-	6.4	4.10×10^{-7}	20.77	26.8
S191229ah	2019-12-29T21:50:21	1.23×10^{-6}	Burst	-	-	8.9	7.45×10^{-7}	22.06	23.56
S191229ai	2019-12-29T22:11:21	7.60×10^{-6}	CBC	0.015	NSBH	6.4	1.56×10^{-7}	30.56	60.52
S191229ak	2019-12-29T23:16:09	9.76×10^{-6}	Burst	-	-	5.7	5.81×10^{-7}	7.89	40.58
S191229o	2019-12-29T12:02:34	1.07×10^{-5}	CBC	0.011	NSBH	-	-	-	-
S191230aa	2019-12-30T13:51:30	1.07×10^{-5}	CBC	0.011	NSBH	6.6	4.68×10^{-7}	55.93	0.06
S191230ae	2019-12-30T14:19:12	1.44×10^{-5}	CBC	0.011	Mass Gap	5.8	1.89×10^{-7}	34.17	54.3
S191230at	2019-12-30T21:24:48	1.64×10^{-5}	CBC	0.011	BNS	6.1	5.52×10^{-7}	0.09	48.46
S191230au	2019-12-30T22:04:37	2.12×10^{-6}	Burst	-	-	7.0	2.54×10^{-7}	40.47	20.44
S191230e	2019-12-30T02:40:45	1.09×10^{-5}	Burst	-	-	-	-	-	-
S191230k	2019-12-30T04:10:08	3.17×10^{-7}	Burst	-	-	-	-	-	-
S191230v	2019-12-30T11:19:08	8.75×10^{-6}	CBC	0.013	NSBH	6.8	5.44×10^{-7}	0.36	1.48
S191230y	2019-12-30T13:08:19	1.01×10^{-5}	Burst	-	-	5.7	4.53×10^{-7}	2.13	52.59
S191231ad	2019-12-31T11:45:12	1.33×10^{-6}	Burst	-	-	6.9	1.21×10^{-7}	51.96	34.52
S191231an	2019-12-31T16:59:30	1.67×10^{-5}	CBC	0.009	NSBH	6.2	5.52×10^{-7}	11.42	7.79
S200101o	2020-01-01T14:18:13	1.66×10^{-5}	CBC	0.012	BNS	7.4	5.29×10^{-7}	1.52	61.15
S200102ah	2020-01-02T15:04:48	1.70×10^{-5}	CBC	0.007	NSBH	5.3	5.99×10^{-7}	0	38.48
S200102an	2020-01-02T18:05:23	1.45×10^{-5}	Burst	-	-	6.5	5.94×10^{-7}	1.94	32.62
S200102ar	2020-01-02T19:39:36	2.24×10^{-5}	CBC	0.005	NSBH	6.4	1.77×10^{-7}	73.19	2.04
S200102au	2020-01-02T21:01:56	1.77×10^{-5}	CBC	0.009	Mass Gap	5.6	5.10×10^{-7}	6.1	8.29
S200102k	2020-01-02T06:17:35	5.93×10^{-6}	CBC	0.016	NSBH	-	-	-	-
S200102y	2020-01-02T11:15:25	8.42×10^{-6}	Burst	-	-	-	-	-	-
S200103aa	2020-01-03T12:32:22	6.00×10^{-6}	Burst	-	-	5.7	9.42×10^{-7}	1.26	26.1
S200103am	2020-01-03T16:46:33	1.68×10^{-5}	CBC	0.007	NSBH	-	-	-	-
S200103ao	2020-01-03T18:29:37	1.12×10^{-5}	CBC	0.013	NSBH	7.0	3.23×10^{-6}	1.05	67.67
S200103aw	2020-01-03T22:34:12	2.00×10^{-5}	CBC	0.002	BBH	5.2	5.28×10^{-7}	0.22	25.17
S200103az	2020-01-03T23:31:11	1.32×10^{-6}	CBC	0.078	NSBH	6.6	2.58×10^{-7}	1.42	97.64
S200103r	2020-01-03T09:42:24	1.57×10^{-6}	Burst	-	-	6.4	2.60×10^{-7}	27.35	36.86
S200103t	2020-01-03T10:31:18	4.10×10^{-6}	Burst	-	-	5.9	7.13×10^{-7}	10.63	21.96
S200103v	2020-01-03T10:55:34	1.18×10^{-5}	Burst	-	-	6.4	3.68×10^{-7}	24.33	31.88
S200103z	2020-01-03T11:55:03	1.49×10^{-5}	Burst	-	-	-	-	-	-
S200104aa	2020-01-04T10:04:38	9.99×10^{-6}	Burst	-	-	6.1	4.74×10^{-7}	6.58	43.27
S200104ar	2020-01-04T19:50:42	3.13×10^{-6}	CBC	0.024	NSBH	6.7	5.16×10^{-7}	0.4	26.15
S200104d	2020-01-04T04:13:54	2.99×10^{-6}	Burst	-	-	6.2	3.78×10^{-7}	8.92	44.22
S200104r	2020-01-04T08:05:48	1.70×10^{-5}	CBC	0.010	BNS	6.0	4.83×10^{-7}	0.03	12.34
S200105aj	2020-01-05T18:00:59	1.43×10^{-5}	CBC	0.010	BNS	-	-	-	-
S200105p	2020-01-05T09:03:23	9.27×10^{-6}	CBC	0.019	BNS	6.0	2.87×10^{-7}	18.21	77.63
S200105u	2020-01-05T12:01:59	2.26×10^{-5}	CBC	0.005	NSBH	6.8	8.27×10^{-7}	1.99	41.47
S200105w	2020-01-05T12:48:13	6.15×10^{-6}	CBC	0.012	NSBH	5.6	5.22×10^{-7}	1.4	69.28
S200106ar	2020-01-06T17:48:06	3.03×10^{-6}	Burst	-	-	6.4	1.54×10^{-7}	58.45	21.4
S200106az	2020-01-06T18:50:35	1.39×10^{-5}	Burst	-	-	6.5	3.42×10^{-7}	13.15	69.28
S200106bd	2020-01-06T22:24:59	1.76×10^{-5}	CBC	0.005	BNS	5.8	8.99×10^{-7}	0.02	99.56
S200106f	2020-01-06T01:36:45	1.76×10^{-6}	Burst	-	-	6.0	6.32×10^{-7}	4.58	18.82
S200106i	2020-01-06T03:07:57	1.82×10^{-5}	CBC	0.015	Mass Gap	5.5	4.44×10^{-7}	14.62	28.82
S200106k	2020-01-06T04:37:09	1.86×10^{-5}	CBC	0.009	Mass Gap	7.0	3.30×10^{-7}	17.36	36.7
S200106s	2020-01-06T08:37:45	8.19×10^{-6}	Burst	-	-	-	-	-	-
S200107i	2020-01-07T03:16:26	5.14×10^{-6}	Burst	-	-	5.4	5.52×10^{-7}	0.1	23.85
S200107j	2020-01-07T03:22:04	3.44×10^{-7}	Burst	-	-	6.5	6.19×10^{-7}	0	7.88
S200107m	2020-01-07T04:08:28	4.26×10^{-6}	CBC	0.022	NSBH	5.6	4.71×10^{-7}	13.51	34.62
S200107o	2020-01-07T05:11:52	1.05×10^{-5}	CBC	0.006	NSBH	5.3	6.16×10^{-7}	0.77	24.76

S200108ag	2020-01-08T18:30:05	2.24×10^{-5}	CBC	0.009	BNS	6.6	3.40×10^{-7}	37.19	28.06
S200108ah	2020-01-08T18:42:57	2.16×10^{-5}	CBC	0.008	NSBH	7.1	3.15×10^{-7}	25.82	29.67
S200108an	2020-01-08T23:51:51	1.66×10^{-5}	CBC	0.011	BNS	6.8	4.67×10^{-7}	34.39	12.38
S200108j	2020-01-08T03:42:27	2.24×10^{-5}	CBC	0.007	NSBH	5.7	5.72×10^{-7}	15.67	30.15
S200108l	2020-01-08T04:13:13	2.13×10^{-6}	CBC	0.092	BNS	6.4	3.53×10^{-7}	10.23	41.69
S200108p	2020-01-08T05:20:09	1.93×10^{-7}	CBC	0.470	BNS	7.4	7.83×10^{-7}	2.39	46.3
S200109m	2020-01-09T08:48:21	1.94×10^{-5}	CBC	0.006	NSBH	5.9	4.91×10^{-7}	11.43	3.39
S200109o	2020-01-09T13:51:35	1.44×10^{-5}	Burst	-	-	5.8	1.09×10^{-7}	77.72	9.11
S200109r	2020-01-09T15:30:31	3.14×10^{-6}	Burst	-	-	7.0	5.56×10^{-7}	0	99.4
S200109s	2020-01-09T15:44:38	4.34×10^{-6}	Burst	-	-	7.0	4.75×10^{-7}	22.85	20.23
S200110aa	2020-01-10T11:01:48	2.12×10^{-5}	Burst	-	-	7.1	2.92×10^{-7}	47.55	21.69
S200110d	2020-01-10T01:23:11	1.45×10^{-5}	Burst	-	-	7.3	5.40×10^{-7}	7.42	39.3
S200110e	2020-01-10T02:01:40	6.32×10^{-6}	Burst	-	-	5.8	3.77×10^{-7}	0.77	14.67
S200110m	2020-01-10T05:25:05	1.21×10^{-6}	Burst	-	-	6.7	6.61×10^{-7}	1.48	5.31
S200110q	2020-01-10T05:46:19	4.45×10^{-6}	Burst	-	-	6.4	4.99×10^{-7}	0.76	61.25
S200110s	2020-01-10T06:46:45	1.51×10^{-5}	Burst	-	-	6.9	1.35×10^{-7}	79.96	3.4
S200110t	2020-01-10T07:50:59	1.79×10^{-5}	Burst	-	-	6.5	4.70×10^{-7}	11.22	28.08
S200110v	2020-01-10T08:40:52	1.56×10^{-5}	Burst	-	-	6.5	2.89×10^{-7}	25.33	9.06
S200110z	2020-01-10T10:33:06	6.50×10^{-6}	Burst	-	-	5.8	2.03×10^{-7}	56.99	10.49
S200111ae	2020-01-11T22:02:00	1.61×10^{-5}	CBC	0.009	NSBH	6.2	7.87×10^{-7}	11.26	25.72
S200111j	2020-01-11T06:51:45	2.70×10^{-6}	Burst	-	-	6.9	5.25×10^{-7}	12.19	27.34
S200111s	2020-01-11T15:23:44	1.04×10^{-5}	CBC	0.019	BNS	-	-	-	-
S200111w	2020-01-11T19:00:59	1.36×10^{-5}	CBC	0.011	NSBH	5.7	2.70×10^{-7}	60.18	0.99
S200112ac	2020-01-12T21:29:08	1.60×10^{-5}	CBC	0.004	NSBH	6.0	6.91×10^{-7}	1.12	79.05
S200112e	2020-01-12T09:44:25	1.61×10^{-5}	CBC	0.009	BNS	6.2	6.47×10^{-7}	0.01	58.06
S200113f	2020-01-13T02:14:20	1.79×10^{-5}	CBC	0.010	BNS	5.3	3.12×10^{-7}	18.59	56.9
S200113g	2020-01-13T02:20:40	1.81×10^{-5}	CBC	0.009	BNS	5.6	4.69×10^{-7}	3.35	0.16
S200113n	2020-01-13T09:59:40	1.57×10^{-5}	CBC	0.013	Mass Gap	6.4	6.05×10^{-7}	0.52	68.21
S200113u	2020-01-13T14:59:11	1.13×10^{-8}	Burst	-	-	6.4	5.70×10^{-7}	7.56	1.52
S200114e	2020-01-14T01:51:22	1.88×10^{-5}	CBC	0.006	NSBH	6.0	4.80×10^{-7}	0.19	95.25
S200114f	2020-01-14T02:08:18	1.23×10^{-9}	Burst			8.8	4.80×10^{-8}	99.74	0.0
S200114m	2020-01-14T05:47:08	1.94×10^{-5}	CBC	0.035	BBH	6.4	3.90×10^{-7}	30.04	0.06
S200114p	2020-01-14T06:50:05	1.27×10^{-5}	CBC	0.009	NSBH	-	-	-	-
S200114w	2020-01-14T13:17:40	2.76×10^{-6}	CBC	0.238	BBH	6.2	4.37×10^{-7}	25.85	0.22
S200115ab	2020-01-15T13:47:04	1.07×10^{-5}	Burst	-	-	6.7	4.82×10^{-7}	6.56	15.38
S200115ak	2020-01-15T21:00:55	1.14×10^{-5}	CBC	0.014	Mass Gap	4.3	8.80×10^{-8}	85.4	11.91
S200116ab	2020-01-16T10:11:59	1.67×10^{-5}	CBC	0.011	BNS	4.5	1.17×10^{-7}	42.05	49.47
S200116am	2020-01-16T13:27:34	3.02×10^{-6}	CBC	0.046	BNS	5.8	1.64×10^{-7}	44.69	36.94
S200116ay	2020-01-16T20:55:30	4.83×10^{-6}	CBC	0.028	BNS	6.4	1.50×10^{-7}	77.03	7.07
S200116b	2020-01-16T00:08:17	2.85×10^{-6}	Burst	-	-	-	-	-	-
S200116ba	2020-01-16T22:20:08	6.77×10^{-6}	CBC	0.059	BNS	5.7	7.51×10^{-7}	31.22	2.16
S200116d	2020-01-16T00:31:07	1.59×10^{-5}	CBC	0.019	BNS	6.8	4.59×10^{-7}	32.04	6.68
S200116k	2020-01-16T05:12:12	3.30×10^{-6}	Burst	-	-	5.2	2.91×10^{-7}	34.49	36.85
S200116o	2020-01-16T06:43:19	1.46×10^{-6}	Burst	-	-	6.5	3.25×10^{-7}	10.6	28.01
S200117ag	2020-01-17T15:45:58	1.55×10^{-6}	Burst	-	-	-	-	-	-
S200117ao	2020-01-17T19:43:02	1.05×10^{-5}	CBC	0.017	BNS	5.9	3.21×10^{-7}	0.08	38.99
S200117aq	2020-01-17T20:18:33	1.56×10^{-5}	CBC	0.007	NSBH	-	-	-	-
S200117as	2020-01-17T20:57:03	1.99×10^{-5}	Burst	-	-	6.3	5.93×10^{-7}	3.32	25.36
S200117j	2020-01-17T07:36:50	1.86×10^{-5}	Burst	-	-	6.2	4.51×10^{-7}	19	37.3
S200117z	2020-01-17T13:25:54	1.88×10^{-5}	CBC	0.005	NSBH	7.3	4.93×10^{-7}	18.54	30.53

S200118ap	2020-01-18T16:45:38	5.77×10^{-6}	CBC	0.020	NSBH	-	-	-	-
S200118as	2020-01-18T19:10:51	2.01×10^{-6}	CBC	0.060	NSBH	6.6	3.31×10^{-7}	67.28	0.84
S200118d	2020-01-18T01:15:36	1.56×10^{-5}	CBC	0.019	NSBH	-	-	-	-
S200118e	2020-01-18T01:14:04	1.76×10^{-6}	Burst	-	-	-	-	-	-
S200118k	2020-01-18T02:27:04	2.95×10^{-6}	Burst	-	-	6.3	2.78×10^{-7}	19.81	11.16
S200118p	2020-01-18T05:07:50	6.22×10^{-6}	CBC	0.027	BNS	5.7	2.65×10^{-7}	32.81	44.11
S200118z	2020-01-18T08:30:55	1.87×10^{-5}	CBC	0.011	BNS	6.0	4.27×10^{-7}	14.37	32.28
S200119g	2020-01-19T05:29:43	5.41×10^{-6}	CBC	0.026	BNS	5.7	5.73×10^{-7}	0.09	96
S200119h	2020-01-19T05:52:36	2.00×10^{-5}	CBC	0.009	BNS	6.5	1.44×10^{-7}	59.9	18.67
S200120e	2020-01-20T20:51:02	1.37×10^{-6}	Burst	-	-	6.5	4.84×10^{-7}	0	75.71
S200121h	2020-01-21T04:24:28	3.33×10^{-6}	CBC	0.026	NSBH	6.6	4.67×10^{-7}	2.84	10.67
S200121i	2020-01-21T06:14:01	9.81×10^{-6}	CBC	0.019	Mass Gap	6.2	2.85×10^{-7}	8.61	43.99
S200121q	2020-01-21T12:26:48	3.38×10^{-6}	CBC	0.036	BNS	6.5	4.09×10^{-7}	0.8	11.98
S200122a	2020-01-22T01:00:57	3.03×10^{-6}	Burst	-	-	5.5	5.80×10^{-7}	9.99	63.39
S200122d	2020-01-22T02:11:17	8.91×10^{-6}	Burst	-	-	-	-	-	-
S200122m	2020-01-22T06:15:00	1.59×10^{-5}	CBC	0.007	NSBH	5.6	2.49×10^{-7}	29.58	42.92
S200122n	2020-01-22T06:14:09	3.35×10^{-6}	Burst	-	-	5.8	3.99×10^{-7}	1.05	61.04
S200124n	2020-01-24T08:50:58	2.28×10^{-5}	CBC	0.006	BNS	-	-	-	-
S200124z	2020-01-24T15:18:12	2.20×10^{-5}	CBC	0.005	NSBH	7.0	8.27×10^{-7}	1.41	3.93
S200126ab	2020-01-26T21:05:59	9.92×10^{-6}	CBC	0.020	BNS	-	-	-	-
S200126ad	2020-01-26T22:58:49	4.32×10^{-6}	CBC	0.036	BNS	5.8	1.82×10^{-7}	29.24	43.96
S200126b	2020-01-26T01:03:12	1.55×10^{-5}	Burst	-	-	5.5	4.20×10^{-7}	13.58	8.72
S200126q	2020-01-26T12:12:11	2.11×10^{-5}	CBC	0.011	Mass Gap	-	-	-	-
S200126s	2020-01-26T12:44:32	6.16×10^{-6}	CBC	0.022	BNS	NFL	3.58×10^{-7}	27.08	4.78
S200127c	2020-01-27T00:49:50	5.48×10^{-7}	CBC	0.042	NSBH	5.8	2.64×10^{-7}	0.36	67.07
S200127o	2020-01-27T11:43:05	2.50×10^{-6}	CBC	0.058	BNS	-	-	-	-
S200127s	2020-01-27T15:27:19	1.89×10^{-5}	CBC	0.012	BNS	-	-	-	-
S200128d	2020-01-28T02:20:11	1.64×10^{-8}	CBC	0.968	BBH	7.0	2.07×10^{-7}	26.25	53
S200128f	2020-01-28T04:54:04	1.37×10^{-6}	Burst	-	-	5.8	4.76×10^{-7}	4.67	17.22
S200128p	2020-01-28T09:54:07	5.35×10^{-6}	CBC	0.024	NSBH	6.1	5.62×10^{-7}	13.76	23.17
S200129ab	2020-01-29T11:10:15	5.74×10^{-6}	CBC	0.026	BNS	6.3	4.95×10^{-7}	0.02	70.01
S200129ad	2020-01-29T11:57:52	1.87×10^{-6}	CBC	0.035	NSBH	5.3	6.48×10^{-7}	0.01	0.71
S200129ai	2020-01-29T13:01:06	1.99×10^{-5}	CBC	0.009	BNS	-	-	-	-
S200129ap	2020-01-29T15:39:24	1.95×10^{-5}	Burst	-	-	6.6	5.53×10^{-7}	0.20	37.41
S200129bb	2020-01-29T19:36:46	1.60×10^{-5}	CBC	0.006	NSBH	5.3	2.13×10^{-7}	29.97	45.18
S200129i	2020-01-29T05:07:00	6.89×10^{-6}	CBC	0.022	BNS	6.3	2.93×10^{-7}	6.78	0.01
S200129k	2020-01-29T06:26:01	1.57×10^{-5}	CBC	0.008	BNS	5.9	5.75×10^{-7}	5.58	2.87
S200129m	2020-01-29T06:54:58	6.70×10^{-32}	CBC	1.000	BBH	5.8	9.44×10^{-7}	0	0
S200129q	2020-01-29T08:50:16	2.20×10^{-6}	CBC	0.040	NSBH	5.8	5.38×10^{-7}	1.52	83.06
S200129v	2020-01-29T10:18:47	8.13×10^{-7}	CBC	0.109	NSBH	5.7	6.64×10^{-7}	0	41.39
S200130ac	2020-01-30T07:40:34	3.08×10^{-6}	CBC	0.056	Mass Gap	5.4	1.73×10^{-6}	4.79	25.29
S200130ai	2020-01-30T09:59:58	1.78×10^{-5}	CBC	0.008	NSBH	16.4	1.86×10^{-7}	36.48	0.01
S200130aq	2020-01-30T13:16:21	2.19×10^{-5}	Burst	-	-	5.1	4.24×10^{-7}	8.56	32.34
S200130at	2020-01-30T14:33:37	2.65×10^{-6}	CBC	0.052	BNS	5.7	6.78×10^{-7}	13.85	0.5
S200130j	2020-01-30T04:27:50	3.69×10^{-6}	Burst	-	-	6.0	3.04×10^{-7}	35.45	31.31
S200130z	2020-01-30T07:10:21	1.48×10^{-5}	CBC	0.009	NSBH	5.9	4.44×10^{-7}	0.29	39.17
S200131ap	2020-01-31T19:39:35	1.39×10^{-5}	CBC	0.013	BNS	6.4	6.54×10^{-7}	23	57.25
S200131c	2020-01-31T01:15:08	2.14×10^{-5}	CBC	0.020	BNS	5.4	3.11×10^{-7}	21.02	1.03
S200201b	2020-02-01T01:35:45	4.03×10^{-6}	CBC	0.036	Mass Gap	5.8	5.20×10^{-7}	5.04	29.4
S200201c	2020-02-01T01:39:17	9.88×10^{-6}	CBC	0.017	BNS	5.7	2.23×10^{-7}	0.26	56.09

S200204ak	2020-02-04T21:52:56	1.86×10^{-5}	CBC	0.006	NSBH	6.8	3.76×10^{-7}	1.98	94.09
S200205ab	2020-02-05T07:30:51	3.45×10^{-6}	CBC	0.040	Mass Gap	5.9	6.29×10^{-7}	0.04	1.56
S200205ag	2020-02-05T09:43:05	1.64×10^{-6}	CBC	0.042	NSBH	-	-	-	-
S200205as	2020-02-05T17:02:05	1.15×10^{-5}	Burst	-	-	6.4	5.83×10^{-7}	5.46	4.09
S200205ax	2020-02-05T22:44:49	1.58×10^{-5}	Burst	-	-	5.8	1.92×10^{-7}	38.29	30.69
S200205e	2020-02-05T01:59:16	1.59×10^{-5}	CBC	0.007	NSBH	5.7	2.00×10^{-7}	55.33	8.32
S200206ao	2020-02-06T11:38:22	5.32×10^{-6}	CBC	0.024	BNS	-	-	-	-
S200206at	2020-02-06T17:45:55	1.91×10^{-5}	CBC	0.010	BNS	6.2	6.37×10^{-7}	1.16	64.96
S200206bc	2020-02-06T21:24:22	8.73×10^{-7}	CBC	0.124	NSBH	6.8	2.27×10^{-7}	47.65	0.05
S200206bg	2020-02-06T23:07:15	5.99×10^{-7}	Burst	-	-	6.0	2.49×10^{-7}	38.9	29.45
S200206r	2020-02-06T05:16:09	6.24×10^{-6}	Burst	-	-	6.5	9.68×10^{-7}	0.19	79.89
S200206v	2020-02-06T05:40:04	5.90×10^{-6}	Burst	-	-	6.3	3.51×10^{-7}	10.08	55.9
S200207aq	2020-02-07T16:46:26	3.38×10^{-6}	CBC	0.001	Mass Gap	-	-	-	-
S200207t	2020-02-07T07:53:06	2.21×10^{-5}	CBC	0.005	NSBH	5.5	3.37×10^{-7}	37.1	2.7
S200208ac	2020-02-08T18:57:11	2.70×10^{-6}	Burst	-	-	5.7	2.03×10^{-7}	33.49	40.16
S200208l	2020-02-08T09:01:03	1.76×10^{-5}	Burst	-	-	-	-	-	-
S200208q	2020-02-08T13:01:17	2.52×10^{-9}	CBC	0.993	BBH	6.2	5.33×10^{-7}	0	0.76
S200208v	2020-02-08T15:32:25	2.40×10^{-6}	CBC	0.045	NSBH	5.0	3.36×10^{-7}	18.52	67.4
S200209al	2020-02-09T12:55:21	1.25×10^{-6}	Burst	-	-	5.6	3.53×10^{-7}	23.45	26.32
S200209am	2020-02-09T13:14:49	8.41×10^{-6}	CBC	0.021	BNS	-	-	-	-
S200209au	2020-02-09T16:44:05	1.21×10^{-5}	Burst	-	-	-	-	-	-
S200209aw	2020-02-09T17:00:21	1.40×10^{-6}	Burst	-	-	6.6	4.63×10^{-7}	0.1	0.61
S200209az	2020-02-09T17:56:15	6.13×10^{-6}	CBC	0.020	BNS	NFL	3.45×10^{-7}	1.95	36.71
S200209ba	2020-02-09T17:58:01	1.58×10^{-5}	CBC	0.009	BNS	5.3	3.71×10^{-7}	7.77	80.29
S200209bc	2020-02-09T18:16:45	1.14×10^{-5}	Burst	-	-	6.2	1.83×10^{-7}	49.17	29.45
S200209h	2020-02-09T02:11:42	2.10×10^{-5}	CBC	0.009	BNS	NFL	6.73×10^{-7}	0	0.01
S200209i	2020-02-09T02:17:13	1.16×10^{-5}	Burst	-	-	6.4	5.82×10^{-7}	5.95	10.37
S200209v	2020-02-09T07:08:38	8.58×10^{-7}	Burst	-	-	-	-	-	-
S200209w	2020-02-09T07:28:45	6.43×10^{-7}	Burst	-	-	-	-	-	-
S200210ab	2020-02-10T10:48:37	1.66×10^{-5}	Burst	-	-	-	-	-	-
S200210ah	2020-02-10T13:05:01	2.11×10^{-6}	Burst	-	-	6.9	5.10×10^{-7}	0.71	19.31
S200210an	2020-02-10T16:13:46	1.22×10^{-5}	CBC	0.040	BBH	6.7	4.31×10^{-7}	2.56	10.46
S200210b	2020-02-10T00:55:44	8.04×10^{-6}	Burst	-	-	4.5	2.54×10^{-7}	13.89	11.39
S200211k	2020-02-11T03:15:00	5.56×10^{-6}	CBC	0.036	BNS	-	-	-	-
S200212aa	2020-02-12T10:18:23	3.52×10^{-6}	CBC	0.157	BBH	5.6	3.85×10^{-7}	19.75	0.88
S200212ai	2020-02-12T12:09:01	8.97×10^{-6}	CBC	0.018	NSBH	5.3	5.81×10^{-7}	1.33	45.09
S200212s	2020-02-12T08:36:40	8.70×10^{-6}	Burst	-	-	-	-	-	-
S200213p	2020-02-13T03:31:54	1.37×10^{-5}	CBC	0.007	NSBH	5.7	3.93×10^{-7}	49.08	3.09
S200213q	2020-02-13T03:43:44	2.18×10^{-5}	CBC	0.008	BNS	6.5	6.14×10^{-7}	18.76	0.02
S200213z	2020-02-13T06:07:16	6.36×10^{-6}	CBC	0.052	BBH	6.2	5.15×10^{-7}	13.91	10.38
S200214ah	2020-02-14T10:24:52	2.26×10^{-6}	Burst	-	-	4.7	6.11×10^{-7}	1.18	13.1
S200214av	2020-02-14T14:04:55	2.50×10^{-7}	Burst	-	-	5.9	6.70×10^{-7}	0.11	56.56
S200214bd	2020-02-14T16:49:01	2.08×10^{-5}	CBC	0.006	BNS	5.8	2.87×10^{-7}	57.29	1.98
S200214bn	2020-02-14T19:56:24	9.25×10^{-7}	Burst	-	-	-	-	-	-
S200214bo	2020-02-14T20:35:29	1.93×10^{-5}	CBC	0.011	BNS	7.2	4.64×10^{-7}	10.09	17.62
S200214bp	2020-02-14T22:14:40	8.48×10^{-6}	CBC	0.021	NSBH	5.3	1.79×10^{-7}	17.92	60.62
S200214bq	2020-02-14T22:33:07	3.08×10^{-6}	CBC	0.005	Mass Gap	5.4	2.37×10^{-7}	3.03	53.35
S200214br	2020-02-14T22:45:26	7.01×10^{-8}	Burst	-	-	5.2	8.21×10^{-7}	0.12	78.46
S200214m	2020-02-14T04:36:51	1.03×10^{-5}	CBC	0.033	BBH	5.3	8.45×10^{-7}	3.54	3.01
S200214p	2020-02-14T05:11:32	1.17×10^{-5}	CBC	0.015	BNS	5.4	5.44×10^{-7}	0.02	28.5

S200215ah	2020-02-15T19:59:56	1.02×10^{-6}	CBC	0.126	BNS	-	-	-	-
S200215t	2020-02-15T12:23:33	8.20×10^{-6}	CBC	0.021	BNS	-	-	-	-
S200215z	2020-02-15T16:38:59	1.86×10^{-5}	CBC	0.010	BNS	-	-	-	-
S200216ae	2020-02-16T10:33:58	7.56×10^{-7}	Burst	-	-	5.5	4.85×10^{-7}	10.17	19.3
S200216aj	2020-02-16T11:51:34	9.95×10^{-6}	CBC	0.015	BNS	5.9	5.46×10^{-7}	0.9	21.46
S200216be	2020-02-16T18:39:33	5.80×10^{-7}	Burst	-	-	-	-	-	-
S200216br	2020-02-16T22:08:05	1.68×10^{-5}	CBC	0.021	BBH	6.6	2.34×10^{-7}	22.38	0.03
S200216h	2020-02-16T03:24:11	4.34×10^{-6}	Burst	-	-	5.2	5.73×10^{-7}	1.3	31.24
S200217ar	2020-02-17T12:22:07	2.27×10^{-5}	CBC	0.002	Mass Gap	-	-	-	-
S200217bd	2020-02-17T16:05:11	1.80×10^{-5}	CBC	0.009	BNS	-	-	-	-
S200217bh	2020-02-17T16:46:46	1.20×10^{-5}	CBC	0.029	BBH	-	-	-	-
S200217c	2020-02-17T03:10:33	2.12×10^{-6}	Burst	-	-	6.4	1.57×10^{-7}	49.36	29.59
S200217cg	2020-02-17T22:52:12	7.45×10^{-6}	CBC	0.014	NSBH	4.9	2.61×10^{-7}	0.32	1.31
S200217k	2020-02-17T04:53:17	7.52×10^{-6}	CBC	0.020	Mass Gap	6.4	6.12×10^{-7}	0.56	1.74
S200217v	2020-02-17T07:30:47	1.53×10^{-5}	Burst	-	-	5.7	3.55×10^{-7}	26.82	18.2
S200217w	2020-02-17T07:37:44	3.05×10^{-7}	CBC	0.431	BBH	5.9	4.27×10^{-7}	9.19	28.12
S200218al	2020-02-18T10:05:22	6.19×10^{-8}	Burst	-	-	6.0	4.84×10^{-7}	13.96	10.77
S200218am	2020-02-18T10:39:25	1.28×10^{-6}	CBC	0.131	Mass Gap	6.3	5.47×10^{-7}	2.47	5.86
S200218ay	2020-02-18T14:03:56	8.63×10^{-6}	CBC	0.019	BNS	6.2	3.55×10^{-7}	0.02	97.23
S200218f	2020-02-18T00:39:55	1.01×10^{-5}	CBC	0.014	BNS	5.7	5.31×10^{-7}	3.5	14.09
S200218i	2020-02-18T01:25:25	2.61×10^{-6}	CBC	0.191	BBH	5.2	5.28×10^{-7}	0.01	29.17
S200218k	2020-02-18T01:28:26	2.23×10^{-5}	CBC	0.010	NSBH	-	-	-	-
S200218u	2020-02-18T04:17:54	7.26×10^{-7}	Burst	-	-	5.9	5.04×10^{-7}	8.13	19.83
S200219a	2020-02-19T00:05:16	8.84×10^{-6}	CBC	0.002	BBH	5.8	1.36×10^{-7}	79.35	5.25
S200219ao	2020-02-19T14:33:42	7.08×10^{-6}	CBC	0.027	BNS	-	-	-	-
S200219ap	2020-02-19T14:47:34	8.93×10^{-6}	CBC	0.025	Mass Gap	6.4	4.21×10^{-7}	0.15	1.07
S200219aq	2020-02-19T14:50:02	2.91×10^{-6}	CBC	0.081	BBH	5.9	5.52×10^{-7}	0	39.72
S200219az	2020-02-19T18:30:38	2.27×10^{-6}	CBC	0.022	NSBH	-	-	-	-
S200219ba	2020-02-19T18:42:03	7.65×10^{-6}	CBC	0.034	BBH	-	-	-	-
S200219bg	2020-02-19T19:45:29	7.09×10^{-6}	CBC	0.128	Mass Gap	5.3	3.87×10^{-7}	27.73	26.67
S200219f	2020-02-19T03:09:19	1.32×10^{-5}	CBC	0.021	BBH	NFL	1.23×10^{-7}	78.19	0.04
S200219q	2020-02-19T07:07:00	1.47×10^{-5}	CBC	0.023	BBH	-	-	-	-
S200220ac	2020-02-20T06:20:14	4.14×10^{-6}	CBC	0.061	BBH	5.8	3.28×10^{-7}	24.26	16.25
S200220ad	2020-02-20T06:19:28	4.86×10^{-7}	Burst	-	-	4.7	5.08×10^{-7}	0.32	54.14
S200220au	2020-02-20T11:04:01	4.01×10^{-6}	CBC	0.056	BNS	5.8	5.28×10^{-7}	9.19	25.92
S200220b	2020-02-20T00:24:32	1.86×10^{-5}	CBC	0.009	BNS	6.6	6.10×10^{-7}	0.04	96.77
S200220bt	2020-02-20T22:11:49	1.03×10^{-6}	CBC	0.155	BNS	4.8	3.44×10^{-7}	17.69	24
S200220bw	2020-02-20T22:55:31	1.14×10^{-5}	CBC	0.012	NSBH	NFL	4.53×10^{-7}	11.26	25.74
S200220k	2020-02-20T02:45:26	1.55×10^{-5}	CBC	0.011	BNS	-	-	-	-
S200220l	2020-02-20T02:48:31	7.95×10^{-6}	CBC	0.022	Mass Gap	5.4	5.49×10^{-7}	0	46.11
S200220u	2020-02-20T04:01:28	1.95×10^{-5}	CBC	0.007	NSBH	5.6	1.75×10^{-7}	33.48	50.49
S200220v	2020-02-20T04:25:03	1.20×10^{-5}	CBC	0.015	Mass Gap	6.2	1.31×10^{-7}	58.52	24.14
S200220w	2020-02-20T04:51:22	2.30×10^{-5}	CBC	0.008	BNS	6.3	2.47×10^{-7}	17.67	32.86
S200220x	2020-02-20T04:52:44	1.73×10^{-5}	CBC	0.006	NSBH	5.5	3.81×10^{-7}	28.03	1.27
S200221ai	2020-02-21T09:28:19	2.37×10^{-6}	CBC	0.036	NSBH	-	-	-	-
S200221ar	2020-02-21T11:08:44	1.86×10^{-5}	Burst	-	-	-	-	-	-
S200221at	2020-02-21T11:26:18	1.77×10^{-5}	Burst	-	-	6.5	4.27×10^{-7}	6.49	34.14
S200221ax	2020-02-21T13:19:12	1.83×10^{-5}	CBC	0.052	Mass Gap	5.6	3.76×10^{-7}	14.66	33.62
S200221b	2020-02-21T00:59:26	1.63×10^{-6}	Burst	-	-	-	-	-	-
S200221bc	2020-02-21T14:07:05	2.99×10^{-6}	Burst	-	-	-	-	-	-

S200221bh	2020-02-21T15:19:18	2.10×10^{-5}	CBC	0.008	Mass Gap	4.9	5.06×10^{-7}	0.00	31.34
S200221bl	2020-02-21T16:59:59	1.20×10^{-5}	Burst	-	-	5.3	3.15×10^{-7}	22.76	35.58
S200221bu	2020-02-21T20:14:38	9.12×10^{-6}	Burst	-	-	5.4	6.43×10^{-7}	5.72	33.06
S200221c	2020-02-21T01:13:57	6.13×10^{-6}	CBC	0.028	BNS	6.1	3.91×10^{-7}	33.59	6.07
S200221z	2020-02-21T06:41:32	8.29×10^{-7}	Burst	-	-	5.8	8.20×10^{-7}	0	44.14
S200222ax	2020-02-22T16:46:05	2.36×10^{-6}	CBC	0.072	Mass Gap	6.6	1.09×10^{-5}	33.39	51.13
S200222h	2020-02-22T02:29:19	2.84×10^{-6}	Burst	-	-	6.6	2.44×10^{-7}	26.95	39.1
S200222j	2020-02-22T02:42:18	7.70×10^{-6}	CBC	0.012	NSBH	6.2	1.27×10^{-7}	77.7	11.1
S200222u	2020-02-22T04:48:17	1.33×10^{-5}	CBC	0.004	Mass Gap	5.6	3.81×10^{-7}	12.98	6.12
S200223aj	2020-02-23T13:50:49	1.35×10^{-5}	CBC	0.005	BNS	5.4	7.01×10^{-7}	0.02	72.95
S200223ao	2020-02-23T14:28:21	6.04×10^{-6}	CBC	0.054	BBH	5.4	6.81×10^{-7}	0.02	0.04
S200223aw	2020-02-23T18:06:59	8.01×10^{-8}	CBC	0.647	BBH	6.7	2.97×10^{-7}	34.45	6.1
S200223az	2020-02-23T20:01:24	1.36×10^{-5}	CBC	0.004	NSBH	5.1	5.68×10^{-7}	3.36	18.7
S200223l	2020-02-23T05:17:44	1.77×10^{-5}	CBC	0.008	NSBH	-	-	-	-
S200223u	2020-02-23T08:09:27	5.54×10^{-6}	CBC	0.054	BBH	-	-	-	-
S200224ab	2020-02-24T05:45:46	2.12×10^{-5}	CBC	0.040	Mass Gap	5.8	5.95×10^{-7}	4.78	6.01
S200224ac	2020-02-24T05:52:07	2.64×10^{-6}	Burst	-	-	-	-	-	-
S200224ag	2020-02-24T06:30:15	1.61×10^{-5}	CBC	0.030	Mass Gap	-	-	-	-
S200224ak	2020-02-24T06:55:12	1.08×10^{-5}	CBC	0.009	NSBH	-	-	-	-
S200224as	2020-02-24T09:34:32	1.91×10^{-5}	CBC	0.003	NSBH	-	-	-	-
S200224cb	2020-02-24T22:32:38	1.36×10^{-5}	CBC	0.027	BBH	5.7	4.30×10^{-7}	0.59	78.05
S200224cd	2020-02-24T23:13:13	1.33×10^{-5}	CBC	0.010	NSBH	6.4	5.34×10^{-7}	0.09	99.28
S200224f	2020-02-24T01:45:03	7.47×10^{-6}	CBC	0.037	BBH	6.0	8.83×10^{-7}	3.55	63.38
S200224j	2020-02-24T02:01:47	1.93×10^{-5}	CBC	0.011	Mass Gap	5.2	4.77×10^{-7}	2.08	0.32
S200224o	2020-02-24T03:05:24	1.33×10^{-6}	Burst	-	-	-	-	-	-
S200225ac	2020-02-25T09:12:05	1.65×10^{-5}	CBC	0.015	BBH	5.4	3.89×10^{-7}	9.9	60.86
S200225af	2020-02-25T10:00:45	1.64×10^{-6}	CBC	0.104	BNS	10.6	3.94×10^{-7}	30.89	25.81
S200225ag	2020-02-25T11:02:37	2.21×10^{-5}	CBC	0.008	NSBH	5.8	3.82×10^{-7}	31.76	0.04
S200225an	2020-02-25T12:57:00	1.90×10^{-5}	CBC	0.002	NSBH	6.0	5.91×10^{-7}	15.64	26.36
S200225as	2020-02-25T14:28:07	6.23×10^{-6}	CBC	0.037	BBH	7.3	3.53×10^{-6}	0.33	58.56
S200225av	2020-02-25T21:11:26	1.44×10^{-5}	CBC	0.014	BNS	5.5	3.62×10^{-7}	10.72	81.55
S200225az	2020-02-25T21:59:37	9.58×10^{-6}	CBC	0.013	NSBH	-	-	-	-
S200225ba	2020-02-25T22:09:01	9.84×10^{-6}	CBC	0.018	BNS	5.9	6.72×10^{-7}	0.45	88.36
S200225k	2020-02-25T03:41:20	1.18×10^{-5}	CBC	0.008	NSBH	5.7	9.43×10^{-7}	0.12	90.13
S200225q	2020-02-25T06:04:21	9.19×10^{-9}	CBC	0.956	BBH	8.2	4.63×10^{-6}	2.2	1.44
S200225u	2020-02-25T08:22:49	1.47×10^{-5}	CBC	0.008	NSBH	-	-	-	-
S200226ac	2020-02-26T07:57:51	1.68×10^{-5}	CBC	0.014	NSBH	-	-	-	-
S200226ai	2020-02-26T09:22:07	2.02×10^{-5}	CBC	0.014	BBH	-	-	-	-
S200226bp	2020-02-26T18:09:01	1.73×10^{-5}	CBC	0.012	BNS	5.5	6.21×10^{-7}	8.22	12.38
S200226o	2020-02-26T03:25:47	2.21×10^{-5}	CBC	0.007	BNS	-	-	-	-
S200226z	2020-02-26T07:18:43	7.77×10^{-6}	CBC	0.017	NSBH	-	-	-	-
S200227d	2020-02-27T01:01:17	1.16×10^{-5}	CBC	0.009	NSBH	5.6	4.29×10^{-7}	4.75	41.94
S200227x	2020-02-27T06:49:08	1.12×10^{-5}	CBC	0.054	Mass Gap	6.0	5.80×10^{-7}	12.56	24.34
S200228ai	2020-02-28T12:49:29	1.65×10^{-5}	CBC	0.009	NSBH	-	-	-	-
S200228bi	2020-02-28T23:11:26	1.24×10^{-5}	CBC	0.026	BBH	6.8	4.64×10^{-7}	18.36	27.31
S200228bl	2020-02-28T23:44:54	9.17×10^{-6}	CBC	0.017	Mass Gap	5.9	5.99×10^{-7}	5.01	32.9
S200229ae	2020-02-29T08:04:03	1.26×10^{-5}	Burst	-	-	5.7	7.33×10^{-7}	1.37	66.16
S200229ag	2020-02-29T08:43:31	6.74×10^{-6}	CBC	0.003	NSBH	-	-	-	-
S200229al	2020-02-29T10:32:00	2.19×10^{-5}	CBC	0.005	NSBH	-	-	-	-
S200229bc	2020-02-29T15:40:15	7.92×10^{-6}	CBC	0.014	NSBH	5.7	3.72×10^{-7}	32.31	0

S200229x	2020-02-29T06:39:21	1.85×10^{-5}	CBC	0.024	BNS	6.4	8.77×10^{-7}	0.47	33.3
S200301ae	2020-03-01T09:42:26	7.67×10^{-6}	CBC	0.017	Mass Gap	6.8	1.52×10^{-7}	82.21	1.41
S200301an	2020-03-01T17:37:42	2.54×10^{-6}	Burst	-	-	7.0	5.07×10^{-7}	11.63	26.94
S200301ax	2020-03-01T21:57:02	5.68×10^{-6}	CBC	0.011	BNS	5.4	2.70×10^{-7}	35.19	32.86
S200301o	2020-03-01T06:54:34	9.21×10^{-8}	Burst	-	-	6.5	1.39×10^{-7}	57.81	27.38
S200301q	2020-03-01T07:45:14	1.09×10^{-5}	CBC	0.015	Mass Gap	5.7	1.63×10^{-7}	61.29	0.53
S200301u	2020-03-01T08:14:42	2.08×10^{-6}	Burst	-	-	6.3	2.52×10^{-7}	27.83	47.03
S200302b	2020-03-02T00:58:11	2.06×10^{-5}	CBC	0.006	NSBH	6.5	1.10×10^{-7}	83.73	0.06
S200302bg	2020-03-02T21:53:08	9.31×10^{-6}	CBC	0.021	BNS	-	-	-	-
S200302c	2020-03-02T01:58:11	9.35×10^{-9}	CBC	0.889	BBH	5.7	3.69×10^{-7}	29.48	27.98
S200302m	2020-03-02T06:14:02	1.61×10^{-5}	CBC	0.018	BBH	6.0	3.65×10^{-7}	31.8	14.56
S200303ad	2020-03-03T07:47:20	1.94×10^{-5}	CBC	0.008	NSBH	5.4	9.99×10^{-7}	0.01	52.01
S200303ae	2020-03-03T08:08:40	4.06×10^{-6}	CBC	0.181	BNS	-	-	-	-
S200303aj	2020-03-03T08:36:14	1.47×10^{-5}	CBC	0.016	Mass Gap	-	-	-	-
S200303ba	2020-03-03T12:15:48	1.32×10^{-8}	CBC	0.864	BBH	5.8	5.30×10^{-7}	4.42	16.8
S200303bf	2020-03-03T13:14:32	2.12×10^{-5}	CBC	0.014	BBH	-	-	-	-
S200303bl	2020-03-03T14:42:16	1.75×10^{-5}	CBC	0.016	BBH	6.6	3.27×10^{-7}	1.97	31.14
S200303f	2020-03-03T01:19:35	6.23×10^{-6}	CBC	0.015	NSBH	5.8	5.79×10^{-7}	1.01	0.19
S200303i	2020-03-03T01:44:47	1.48×10^{-5}	CBC	0.051	BBH	-	-	-	-
S200303p	2020-03-03T03:11:58	1.91×10^{-5}	CBC	0.002	NSBH	-	-	-	-
S200303r	2020-03-03T03:34:34	2.22×10^{-5}	CBC	0.013	BBH	-	-	-	-
S200304ao	2020-03-04T14:46:28	8.26×10^{-6}	CBC	0.029	BBH	5.0	4.85×10^{-7}	13.64	29.69
S200304ay	2020-03-04T18:04:42	1.89×10^{-5}	CBC	0.008	NSBH	7.1	-	-	-
S200304bg	2020-03-04T20:03:56	1.88×10^{-5}	CBC	0.005	NSBH	-	-	-	-
S200304bi	2020-03-04T20:03:19	1.30×10^{-5}	Burst	-	-	5.4	2.81×10^{-7}	33.15	37.91
S200304bj	2020-03-04T20:23:27	2.16×10^{-5}	CBC	0.053	Mass Gap	6.0	4.88×10^{-7}	16.78	30.41
S200304d	2020-03-04T02:36:34	2.21×10^{-5}	CBC	0.001	NSBH	7.1	2.47×10^{-7}	39.05	12.81
S200305f	2020-03-05T01:01:14	1.98×10^{-5}	CBC	0.008	Mass Gap	6.6	1.14×10^{-7}	71.25	13.45
S200305h	2020-03-05T01:05:29	2.68×10^{-6}	Burst	-	-	6.2	2.92×10^{-7}	25.95	39.5
S200305q	2020-03-05T03:00:17	2.24×10^{-5}	CBC	0.014	BBH	5.7	1.93×10^{-7}	0.57	99.23
S200305r	2020-03-05T03:09:11	2.26×10^{-5}	CBC	0.006	BNS	6.2	4.11×10^{-7}	31.05	16.42
S200306ar	2020-03-06T11:18:22	9.75×10^{-6}	Burst	-	-	6.9	7.59×10^{-7}	4.26	20.08
S200306aw	2020-03-06T12:03:00	1.97×10^{-5}	CBC	0.015	BNS	6.6	1.93×10^{-7}	32.37	31.1
S200306az	2020-03-06T12:37:37	3.53×10^{-6}	Burst	-	-	5.5	3.75×10^{-6}	13.1	26.61
S200306bj	2020-03-06T14:16:31	9.39×10^{-6}	CBC	0.009	NSBH	4.7	1.87×10^{-7}	9.13	76.94
S200306bq	2020-03-06T15:03:01	1.37×10^{-5}	CBC	0.011	BNS	6.1	2.46×10^{-7}	2.12	1.64
S200306by	2020-03-06T16:21:06	1.31×10^{-7}	Burst	-	-	5.4	6.74×10^{-7}	0.78	12.25
S200306cc	2020-03-06T16:58:29	1.42×10^{-6}	Burst	-	-	5.6	6.07×10^{-7}	11.21	7.81
S200306ci	2020-03-06T19:39:14	5.85×10^{-6}	CBC	0.021	BNS	6.2	3.61×10^{-7}	22.35	33.5
S200306cv	2020-03-06T21:15:25	2.48×10^{-6}	CBC	0.097	BBH	5.8	4.63×10^{-7}	6.64	21.1
S200306dc	2020-03-06T23:07:39	1.40×10^{-5}	CBC	0.024	BBH	-	-	-	-
S200307ac	2020-03-07T07:36:20	9.58×10^{-6}	CBC	0.027	BBH	7.0	3.04×10^{-7}	29.64	25.63
S200307ae	2020-03-07T08:33:25	1.59×10^{-5}	CBC	0.013	BNS	6.1	2.71×10^{-7}	18.12	50.75
S200307ak	2020-03-07T10:01:25	1.24×10^{-9}	Burst	-	-	5.2	3.69×10^{-7}	20.01	0.08
S200307ao	2020-03-07T11:07:37	2.02×10^{-5}	Burst	-	-	5.7	5.42×10^{-7}	10.88	63.59
S200307ap	2020-03-07T12:01:25	1.19×10^{-9}	Burst	-	-	6.5	6.53×10^{-7}	0	23.59
S200307aq	2020-03-07T12:44:02	1.96×10^{-5}	CBC	0.014	BBH	6.4	6.14×10^{-7}	18.03	28.33
S200307ar	2020-03-07T12:51:04	1.24×10^{-5}	Burst	-	-	6.3	4.82×10^{-7}	7.93	16.88
S200307aw	2020-03-07T15:25:33	9.31×10^{-7}	Burst	-	-	5.9	3.10×10^{-7}	29.13	21.97
S200307ay	2020-03-07T16:08:24	4.11×10^{-6}	CBC	0.021	NSBH	-	-	-	-

S200307ba	2020-03-07T17:53:38	1.90×10^{-6}	CBC	0.095	BBH	5.4	4.02×10^{-7}	10.03	1.74
S200307bc	2020-03-07T18:40:01	9.05×10^{-7}	CBC	0.090	BNS	5.6	3.40×10^{-7}	27.17	18.28
S200307bk	2020-03-07T23:36:32	2.20×10^{-5}	CBC	0.006	NSBH	6.4	7.47×10^{-7}	4.42	0.39
S200307c	2020-03-07T02:34:37	2.22×10^{-5}	CBC	0.013	BBH	6.6	7.64×10^{-7}	0.02	65.51
S200307r	2020-03-07T06:08:57	1.27×10^{-6}	Burst	-	-	-	-	-	-
S200307s	2020-03-07T06:10:11	2.60×10^{-6}	Burst	-	-	6.3	2.17×10^{-7}	5.58	91.2
S200307t	2020-03-07T06:39:12	1.20×10^{-5}	CBC	0.008	NSBH	6.3	5.87×10^{-7}	1.25	56.02
S200308af	2020-03-08T11:46:48	5.85×10^{-6}	CBC	0.016	NSBH	NFL	2.62×10^{-7}	31.77	36.97
S200308aj	2020-03-08T12:43:22	3.89×10^{-6}	Burst	-	-	6.0	6.00×10^{-7}	1.14	31.23
S200308au	2020-03-08T14:31:49	1.82×10^{-5}	CBC	0.016	BBH	6.0	6.93×10^{-7}	0.03	99.26
S200308av	2020-03-08T14:28:38	1.25×10^{-5}	Burst	-	-	5.3	3.86×10^{-7}	25.35	23.97
S200308bp	2020-03-08T17:54:08	7.08×10^{-6}	Burst	-	-	6.4	3.87×10^{-7}	8.65	31.83
S200308bz	2020-03-08T20:24:27	1.21×10^{-5}	CBC	0.009	NSBH	6.6	7.08×10^{-7}	1.94	74.72
S200308cc	2020-03-08T21:26:18	6.91×10^{-6}	CBC	0.019	Mass Gap	5.4	4.54×10^{-7}	0.3	0.64
S200308e	2020-03-08T01:19:27	3.62×10^{-9}	CBC	0.830	NSBH	6.2	4.97×10^{-7}	1.91	92.48
S200308g	2020-03-08T01:38:18	7.01×10^{-6}	CBC	0.005	NSBH	5.7	2.20×10^{-7}	28.96	50.22
S200308h	2020-03-08T01:45:05	7.82×10^{-6}	Burst	-	-	5.5	2.04×10^{-7}	43.87	19.8
S200308i	2020-03-08T02:19:35	1.46×10^{-5}	CBC	0.003	NSBH	5.6	1.33×10^{-7}	62.07	9.03
S200308z	2020-03-08T09:11:16	1.08×10^{-6}	CBC	0.087	NSBH	6.2	2.94×10^{-7}	36.66	46.02
S200309ag	2020-03-09T14:45:45	5.47×10^{-6}	CBC	0.031	BNS	5.4	2.96×10^{-7}	23.37	5.03
S200309ai	2020-03-09T15:35:45	1.18×10^{-5}	CBC	0.025	Mass Gap	-	-	-	-
S200309av	2020-03-09T17:57:10	2.15×10^{-5}	CBC	0.014	BBH	5.9	5.55×10^{-8}	95.56	0.07
S200309bh	2020-03-09T21:28:42	1.69×10^{-5}	CBC	0.006	NSBH	6.5	6.71×10^{-7}	0.02	29.24
S200309bj	2020-03-09T22:30:15	2.17×10^{-5}	CBC	0.036	Mass Gap	6.8	3.65×10^{-7}	16.3	26.46
S200309bk	2020-03-09T22:36:27	9.07×10^{-6}	CBC	0.015	BNS	6.1	5.75×10^{-7}	5.45	3.48
S200309bm	2020-03-09T23:14:58	2.29×10^{-5}	CBC	0.016	BBH	-	-	-	-
S200309bu	2020-03-09T23:59:07	4.84×10^{-6}	CBC	0.041	BBH	5.7	5.00×10^{-7}	0.5	1.53
S200309d	2020-03-09T01:26:51	2.18×10^{-5}	Burst	-	-	-	-	-	-
S200310ab	2020-03-10T07:58:59	2.30×10^{-6}	CBC	0.027	Mass Gap	6.8	3.02×10^{-7}	27.19	25.38
S200310az	2020-03-10T22:54:14	1.69×10^{-5}	CBC	0.014	Mass Gap	5.9	3.96×10^{-7}	2.08	1.34
S200310b	2020-03-10T00:20:05	2.02×10^{-5}	CBC	0.002	NSBH	6.4	7.47×10^{-7}	0.09	15.25
S200310f	2020-03-10T01:02:19	7.31×10^{-6}	CBC	0.051	Mass Gap	-	-	-	-
S200310s	2020-03-10T05:59:46	9.75×10^{-7}	Burst	-	-	6.0	8.05×10^{-7}	0.17	76.04
S200310t	2020-03-10T06:11:59	3.41×10^{-6}	CBC	0.053	BNS	5.9	1.03×10^{-7}	85.57	0.03
S200310u	2020-03-10T06:21:24	1.06×10^{-6}	CBC	0.115	BNS	5.6	4.94×10^{-7}	0	32.14
S200311ba	2020-03-11T10:31:22	6.56×10^{-6}	CBC	0.026	BNS	-	-	-	-
S200311bb	2020-03-11T10:34:04	1.41×10^{-6}	CBC	0.115	BNS	5.9	5.97×10^{-7}	11.26	32.65
S200311bp	2020-03-11T14:05:25	9.06×10^{-6}	CBC	0.015	BNS	6.4	3.19×10^{-7}	39.53	31.29
S200311h	2020-03-11T01:48:40	8.12×10^{-6}	Burst	-	-	5.7	3.49×10^{-7}	26.74	1.72
S200311r	2020-03-11T04:04:20	2.06×10^{-6}	CBC	0.049	NSBH	-	-	-	-
S200311v	2020-03-11T04:37:19	1.27×10^{-5}	CBC	0.042	Mass Gap	5.8	4.98×10^{-7}	0.42	53.43
S200311w	2020-03-11T04:50:30	1.40×10^{-5}	CBC	0.018	NSBH	-	-	-	-
S200311y	2020-03-11T04:53:03	7.61×10^{-6}	Burst	-	-	6.5	3.11×10^{-7}	20.96	34.03
S200312aa	2020-03-12T07:36:08	3.63×10^{-6}	CBC	0.023	NSBH	6.2	3.20×10^{-7}	52.44	0
S200312b	2020-03-12T00:34:15	1.93×10^{-5}	CBC	0.008	Mass Gap	-	-	-	-
S200312ba	2020-03-12T15:41:49	9.85×10^{-6}	Burst	-	-	6.8	3.93×10^{-7}	11.22	22.2
S200312br	2020-03-12T22:06:08	1.72×10^{-5}	CBC	0.008	NSBH	6.4	4.39×10^{-7}	16.91	19.47
S200312d	2020-03-12T01:16:51	1.09×10^{-5}	CBC	0.131	BBH	6.4	1.55×10^{-7}	33.13	56.29
S200312i	2020-03-12T01:43:29	2.29×10^{-7}	CBC	0.187	Mass Gap	5.6	3.77×10^{-7}	8.03	69.57
S200313aa	2020-03-13T06:54:23	8.17×10^{-6}	Burst	-	-	5.8	2.66×10^{-7}	43.35	9.32

S200313ag	2020-03-13T07:50:28	9.62×10^{-6}	Burst	-	-	4.2	1.47×10^{-7}	24.9	71.5
S200313aw	2020-03-13T12:33:04	2.11×10^{-5}	CBC	0.010	Mass Gap	-	-	-	-
S200313ba	2020-03-13T13:31:50	8.59×10^{-6}	CBC	0.007	BNS	5.8	3.77×10^{-7}	70.07	0
S200313bb	2020-03-13T13:32:17	1.84×10^{-6}	CBC	0.039	NSBH	5.8	5.09×10^{-7}	0.04	64.3
S200313be	2020-03-13T14:45:42	8.23×10^{-6}	CBC	0.015	NSBH	6.6	5.98×10^{-7}	5.5	43.16
S200313bf	2020-03-13T15:06:31	9.69×10^{-6}	CBC	0.020	Mass Gap	5.6	6.52×10^{-7}	0	42.72
S200313bs	2020-03-13T20:08:46	1.92×10^{-5}	CBC	0.006	BNS	-	-	-	-
S200313by	2020-03-13T21:40:33	2.39×10^{-6}	Burst	-	-	6.8	2.18×10^{-7}	35.94	42.59
S200313cd	2020-03-13T22:39:09	1.18×10^{-5}	CBC	0.009	NSBH	5.4	6.30×10^{-7}	8.44	44.62
S200313h	2020-03-13T01:46:59	4.04×10^{-6}	Burst	-	-	-	-	-	-
S200313j	2020-03-13T02:17:18	6.90×10^{-6}	Burst	-	-	-	-	-	-
S200313l	2020-03-13T02:32:04	2.14×10^{-5}	CBC	0.005	NSBH	6.4	3.90×10^{-7}	62.51	0.02
S200313n	2020-03-13T03:33:07	2.26×10^{-5}	CBC	0.006	Mass Gap	7.0	9.18×10^{-7}	0.35	7.04
S200314ay	2020-03-14T17:23:01	2.26×10^{-5}	CBC	0.005	NSBH	5.4	5.15×10^{-7}	0.01	26.18
S200314be	2020-03-14T19:47:18	8.92×10^{-6}	CBC	0.033	BBH	6.3	5.98×10^{-7}	4.68	31.97
S200314bg	2020-03-14T19:51:02	1.86×10^{-5}	CBC	0.007	NSBH	-	-	-	-
S200314bn	2020-03-14T21:12:48	7.14×10^{-7}	Burst	-	-	5.8	3.00×10^{-7}	39.1	8.05
S200314bt	2020-03-14T22:36:02	1.28×10^{-5}	CBC	0.074	Mass Gap	5.7	4.80×10^{-7}	3.78	41.95
S200314bx	2020-03-14T23:29:35	1.63×10^{-7}	CBC	0.189	NSBH	6.2	1.19×10^{-7}	81.51	3.68
S200314m	2020-03-14T04:21:10	1.04×10^{-5}	CBC	0.012	BNS	6.9	7.35×10^{-6}	0.11	0.29
S200314r	2020-03-14T06:10:33	1.34×10^{-5}	CBC	0.008	NSBH	5.5	4.47×10^{-7}	7.22	20.9
S200314x	2020-03-14T07:26:14	2.05×10^{-5}	CBC	0.005	NSBH	5.6	2.42×10^{-7}	10.07	0.01
S200315ac	2020-03-15T11:07:32	9.83×10^{-6}	CBC	0.002	NSBH	6.6	5.28×10^{-7}	2.8	19.02
S200315ba	2020-03-15T20:48:52	1.62×10^{-5}	CBC	0.022	BBH	5.8	3.05×10^{-7}	14.75	21.12
S200316ad	2020-03-16T10:26:06	1.24×10^{-5}	CBC	0.024	Mass Gap	6.5	3.47×10^{-7}	31.9	1.31
S200316aj	2020-03-16T11:39:17	3.69×10^{-6}	CBC	0.034	NSBH	6.3	6.66×10^{-8}	99.29	0.01
S200316bk	2020-03-16T22:16:22	9.73×10^{-6}	CBC	0.013	BNS	5.8	3.18×10^{-7}	28.02	33.66
S200316f	2020-03-16T01:37:07	6.27×10^{-6}	Burst	-	-	5.8	4.04×10^{-7}	18.78	39.79
S200316u	2020-03-16T06:28:34	1.56×10^{-5}	CBC	0.006	NSBH	5.5	1.73×10^{-7}	95.27	85.21
S200316w	2020-03-16T06:55:03	1.40×10^{-5}	Burst	-	-	-	-	-	-
S200317ad	2020-03-17T11:52:19	1.22×10^{-5}	CBC	0.014	NSBH	5.8	8.61×10^{-7}	0.01	32.78
S200317ag	2020-03-17T13:31:35	3.35×10^{-7}	Burst	-	-	7.4	4.95×10^{-7}	0.2	11.09
S200317ah	2020-03-17T14:00:01	9.02×10^{-6}	CBC	0.076	Mass Gap	6.5	5.40×10^{-7}	6.56	36.73
S200317ai	2020-03-17T14:14:06	9.12×10^{-6}	CBC	0.021	BNS	5.7	6.33×10^{-7}	2.88	76.18
S200317b	2020-03-17T00:19:00	4.79×10^{-6}	Burst	-	-	5.0	4.76×10^{-7}	15.23	11.1
S200317c	2020-03-17T02:24:40	7.27×10^{-6}	CBC	0.081	BNS	6.3	2.79×10^{-7}	42.36	20.62
S200317d	2020-03-17T02:33:58	1.34×10^{-5}	CBC	0.025	BBH	6.4	3.22×10^{-7}	19.1	5.8
S200318af	2020-03-18T08:02:54	1.43×10^{-5}	CBC	0.007	BNS	-	-	-	-
S200318ak	2020-03-18T10:21:25	1.31×10^{-5}	CBC	0.008	NSBH	5.2	2.64×10^{-7}	7.52	97.84
S200318av	2020-03-18T15:35:18	1.16×10^{-5}	Burst	-	-	6.7	5.22×10^{-7}	11.87	20.62
S200318be	2020-03-18T17:57:32	3.22×10^{-6}	CBC	0.048	BNS	6.7	4.11×10^{-7}	0.01	75.66
S200318bf	2020-03-18T18:04:09	4.75×10^{-6}	CBC	0.035	BNS	6.2	3.36×10^{-7}	29.71	27.94
S200318n	2020-03-18T03:20:11	1.06×10^{-5}	CBC	0.010	NSBH	5.9	5.68×10^{-7}	3.38	3.54
S200318s	2020-03-18T04:56:32	1.79×10^{-5}	Burst	-	-	6.6	3.93×10^{-7}	31.15	13.41
S200318z	2020-03-18T06:34:52	6.40×10^{-6}	Burst	-	-	5.9	5.94×10^{-7}	5.89	57.22
S200319aq	2020-03-19T13:50:32	1.21×10^{-5}	CBC	0.020	BBH	6.3	6.57×10^{-7}	6.6	67.54
S200319ax	2020-03-19T15:50:57	1.93×10^{-5}	CBC	0.011	BNS	5.6	4.90×10^{-7}	0.01	28.26
S200319bh	2020-03-19T22:27:38	4.08×10^{-6}	Burst	-	-	6.8	5.57×10^{-7}	13.01	24.54
S200319d	2020-03-19T01:38:23	6.70×10^{-6}	CBC	0.053	BNS	6.2	3.44×10^{-7}	49.34	0.28
S200320af	2020-03-20T08:35:13	1.65×10^{-5}	Burst	-	-	5.9	6.95×10^{-7}	1.24	25.73

S200320bm	2020-03-20T22:34:05	5.16×10^{-7}	CBC	0.193	Mass Gap	NFL	6.95×10^{-7}	3.09	0.4
S200320p	2020-03-20T04:36:30	1.23×10^{-6}	CBC	0.075	NSBH	5.8	2.35×10^{-7}	49.27	35.71
S200320q	2020-03-20T04:37:11	1.49×10^{-5}	Burst	-	-	6.0	5.27×10^{-7}	20.22	24.6
S200320w	2020-03-20T06:15:52	1.51×10^{-6}	Burst	-	-	5.4	6.25×10^{-7}	4.29	30.47
S200321ak	2020-03-21T14:34:50	2.09×10^{-5}	Burst	-	-	5.8	4.99×10^{-7}	10.79	43.72
S200321bb	2020-03-21T22:32:26	2.45×10^{-6}	CBC	0.058	BNS	6.7	6.93×10^{-8}	39.15	59.12
S200321h	2020-03-21T03:46:57	5.11×10^{-6}	Burst	-	-	6.5	4.66×10^{-7}	27.21	20.06
S200321n	2020-03-21T05:03:14	2.21×10^{-5}	CBC	0.009	Mass Gap	5.6	9.15×10^{-7}	0	5.69
S200321z	2020-03-21T10:08:10	1.67×10^{-5}	CBC	0.005	Mass Gap	5.4	7.36×10^{-7}	3.83	2.07
S200322ab	2020-03-22T09:11:33	9.98×10^{-6}	CBC	0.072	BBH	6.2	5.51×10^{-7}	0.06	24.67
S200322at	2020-03-22T14:59:58	1.37×10^{-6}	Burst	-	-	4.8	3.75×10^{-7}	8.31	44.23
S200322ax	2020-03-22T16:35:09	6.07×10^{-6}	Burst	-	-	6.4	5.71×10^{-7}	1.29	33.95
S200322bh	2020-03-22T19:11:57	5.66×10^{-6}	CBC	0.035	Mass Gap	6.8	1.99×10^{-7}	46.19	3.33
S200322bs	2020-03-22T22:32:58	2.23×10^{-5}	Burst	-	-	6.4	1.39×10^{-7}	61.44	1
S200322bv	2020-03-22T23:06:07	1.81×10^{-7}	CBC	0.300	NSBH	-	-	-	-
S200322by	2020-03-22T23:34:00	5.92×10^{-7}	CBC	0.133	NSBH	-	-	-	-
S200322n	2020-03-22T04:11:26	2.32×10^{-6}	CBC	0.037	NSBH	NFL	4.87×10^{-7}	65.29	4.61
S200322q	2020-03-22T04:24:47	4.55×10^{-6}	CBC	0.027	BNS	5.4	2.69×10^{-7}	65.73	11.29
S200322z	2020-03-22T07:51:55	8.31×10^{-6}	CBC	0.017	Mass Gap	6.1	1.96×10^{-7}	61	7.99
S200323ah	2020-03-23T11:31:55	1.82×10^{-5}	Burst	-	-	6.1	5.75×10^{-7}	9.2	15.61
S200323aj	2020-03-23T11:59:25	1.65×10^{-5}	Burst	-	-	5.9	5.11×10^{-7}	8.89	36.02
S200323aq	2020-03-23T13:33:24	4.12×10^{-6}	CBC	0.017	Mass Gap	5.8	2.81×10^{-7}	31.38	31.42
S200323as	2020-03-23T13:53:52	7.47×10^{-6}	CBC	0.013	Mass Gap	5.9	1.30×10^{-7}	24.74	68.22
S200323ax	2020-03-23T14:56:35	1.43×10^{-5}	CBC	0.009	BNS	6.3	8.59×10^{-7}	0.86	1.88
S200323bf	2020-03-23T19:37:34	6.60×10^{-7}	Burst	-	-	8.3	7.72×10^{-7}	2.7	77.62
S200323n	2020-03-23T05:20:05	2.08×10^{-5}	CBC	0.010	BNS	6.2	7.74×10^{-7}	52.37	28.86
S200324a	2020-03-24T01:46:44	6.30×10^{-6}	CBC	0.021	BNS	6.5	2.39×10^{-7}	32.95	36.47
S200324ax	2020-03-24T22:46:32	1.85×10^{-5}	CBC	0.006	NSBH	10.6	-	-	-
S200325au	2020-03-25T23:58:52	2.28×10^{-5}	CBC	0.008	Mass Gap	NFL	1.24×10^{-6}	1.94	90.04
S200325j	2020-03-25T07:23:35	2.81×10^{-6}	CBC	0.105	BBH	6.4	5.41×10^{-7}	1.33	92.1
S200325s	2020-03-25T11:06:27	9.84×10^{-6}	CBC	0.011	Mass Gap	6.4	4.11×10^{-7}	7.56	57.29
S200325w	2020-03-25T12:33:00	9.84×10^{-6}	Burst	0.011	-	5.4	6.61×10^{-7}	0.33	9.94
S200326af	2020-03-26T11:25:01	2.09×10^{-7}	Burst	-	-	6.3	4.21×10^{-7}	12.18	31.76
S200326ax	2020-03-26T16:10:49	1.10×10^{-5}	CBC	0.017	BNS	NFL	1.70×10^{-7}	26.39	55.04
S200326ay	2020-03-26T16:15:13	8.90×10^{-6}	CBC	0.020	BNS	5.8	6.29×10^{-8}	29.72	69.63
S200326az	2020-03-26T16:15:06	4.02×10^{-6}	Burst	-	-	5.8	5.02×10^{-7}	3.33	11.8
S200326d	2020-03-26T02:36:25	1.57×10^{-5}	CBC	0.008	NSBH	-	-	-	-
S200326k	2020-03-26T04:25:22	1.01×10^{-5}	Burst	-	-	-	-	-	-
S200326x	2020-03-26T09:10:40	2.30×10^{-5}	Burst	-	-	6.2	5.18×10^{-7}	8.15	31.08
S200327am	2020-03-27T12:53:52	2.18×10^{-5}	CBC	0.020	BBH	5.9	4.80×10^{-7}	0.76	59.11
S200327as	2020-03-27T14:00:08	1.24×10^{-5}	CBC	0.027	BBH	6.2	4.54×10^{-7}	23.93	34.74
S200327az	2020-03-27T16:01:26	1.51×10^{-5}	CBC	0.009	BNS	7.0	3.04×10^{-7}	51.95	12.82
S200327g	2020-03-27T02:34:28	8.28×10^{-7}	CBC	0.111	BNS	5.7	4.27×10^{-7}	10.82	3.53
S200327i	2020-03-27T03:12:11	1.20×10^{-5}	CBC	0.033	BBH	5.8	4.18×10^{-7}	38.79	17.17
S200327j	2020-03-27T03:15:27	1.66×10^{-5}	CBC	0.006	Mass Gap	22.4	5.80×10^{-7}	26.32	0.13

Table 2. Details of the O3 candidates confirmed by the offline analysis and with a $p_{\rm astro} > 0.5$, for which GUANO data dumps are available. The reported $p_{\rm astro}$ and FAR are relative to the pipeline with the highest $p_{\rm astro}$. If two pipelines have equal $p_{\rm astro}$, we select the one with the highest SNR. The GW FAR, $p_{\rm astro}$ and Class details are quoted from Abbott et al. (2024) and Abbott et al. (2023).

SID	GW name	FAR (Hz)	Group	$p_{\rm astro}$	Class	$p_{\rm Class}$	Pipeline
S190701ah	GW190701_203306	1.79×10^{-8}	CBC	>0.99	BBH	1.00	PyCBC-BBH
S190915ak	GW190915_235702	2.22×10^{-12}	CBC	>0.99	BBH	1.00	PyCBC-BBH
S190930s	GW190930_133541	3.81×10^{-10}	CBC	>0.99	BBH	0.85	PyCBC-BBH
S191127p	GW191127_050227	1.29×10^{-7}	CBC	0.74	BBH	0.74	PyCBC-BBH
S191204r	GW191204_171526	1.86×10^{-13}	CBC	>0.99	BBH	1.00	MBTA
S191216ap	GW191216_213338	2.96×10^{-11}	CBC	>0.99	BBH	1.00	MBTA
S200128d	GW200128_022011	1.36×10^{-10}	CBC	>0.99	BBH	1.00	PyCBC-BBH
S200129m	GW200129_065458	9.03×10^{-41}	CBC	>0.99	BBH	1.00	GstLAL
S200208q	GW200208_130117	9.84×10^{-12}	CBC	>0.99	BBH	1.00	PyCBC-BBH
S200216br	GW200216_220804	1.11×10^{-8}	CBC	0.77	BBH	0.77	GstLAL
S200220ad	GW200220_061928	2.16×10^{-7}	CBC	0.62	BBH	0.62	PyCBC-BBH
S200225q	GW200225_060421	2.79×10^{-11}	CBC	>0.99	BBH	1.00	cWB
S200302c	GW200302_015811	3.54×10^{-9}	CBC	0.91	BBH	0.91	GstLAL
S200322ab	GW200322_091133	1.44×10^{-5}	CBC	0.62	BBH	0.62	MBTA

Table 3. List of the O3 candidates confirmed by the offline analysis with $p_{\mathrm{astro}} < 0.5$, for which GUANO data dumps were available. GW FAR, p_{astro}, Class and p_{Class} are reported from Abbott et al. (2023). CBC or Burst group categories are quoted as per the offline analysis and not from the low-latency information.

SID	Time (UTC)	Group	GW FAR (Hz)	p_{astro}	Class	p_{Class}	Pipeline
S190906ah	2019-09-06T20:05:00	CBC	5.66×10^{-6}	2.38×10^{-3}	BBH	1.51×10^{-3}	GstLAL
S191106r	2019-11-06T18:41:51	CBC	1.18×10^{-5}	1.97×10^{-2}	BBH	1.97×10^{-2}	PyCBC-BBH
S191116ac	2019-11-16T14:21:55	CBC	8.25×10^{-6}	2.10×10^{-4}	NSBH	1.67×10^{-4}	PyCBC-broad
S191121bt	2019-11-21T16:45:42	CBC	5.44×10^{-6}	4.13×10^{-3}	BBH	4.13×10^{-3}	GstLAL
S191208b	2019-12-08T02:02:15	CBC	2.10×10^{-5}	4.26×10^{-4}	BNS	4.26×10^{-4}	PyCBC-broad
S191213be	2019-12-13T19:54:22	CBC	5.78×10^{-6}	5.40×10^{-2}	BBH	5.40×10^{-2}	PyCBC-BBH
S191225aq	2019-12-25T21:57:15	CBC	1.57×10^{-6}	1.30×10^{-2}	BBH	1.30×10^{-2}	GstLAL
S191229o	2019-12-29T12:02:34	CBC	4.17×10^{-6}	1.15×10^{-1}	BBH	6.13×10^{-2}	PyCBC-broad
S191230at	2019-12-30T21:24:48	CBC	1.72×10^{-5}	7.01×10^{-4}	BNS	7.01×10^{-4}	PyCBC-broad
S191231ad	2019-12-31T11:45:12	Burst	4.31×10^{-7}	8.30×10^{-3}	-	-	cWB
S200103az	2020-01-03T23:31:11	CBC	5.09×10^{-6}	3.02×10^{-4}	NSBH	2.98×10^{-4}	PyCBC-broad
S200105aj	2020-01-05T18:00:59	CBC	3.61×10^{-6}	5.88×10^{-4}	BNS	5.85×10^{-4}	MBTA
S200106k	2020-01-06T04:37:09	CBC	1.00×10^{-5}	5.03×10^{-4}	BNS	3.83×10^{-4}	MBTA
S200109m	2020-01-09T08:48:21	CBC	9.82×10^{-6}	1.44×10^{-3}	NSBH	1.34×10^{-3}	PyCBC-broad
S200112e	2020-01-12T09:44:25	CBC	2.01×10^{-6}	3.10×10^{-3}	BNS	3.02×10^{-3}	MBTA
S200113f	2020-01-13T02:14:20	CBC	2.23×10^{-5}	4.20×10^{-5}	BNS	4.20×10^{-5}	MBTA
S200113g	2020-01-13T02:20:40	CBC	8.02×10^{-6}	1.48×10^{-3}	NSBH	1.06×10^{-3}	PyCBC-broad
S200114f	2020-01-14T02:08:18	Burst	5.04×10^{-7}	2.10×10^{-3}	-	-	cWB
S200114w	2020-01-14T13:17:40	CBC	2.89×10^{-6}	9.44×10^{-2}	BBH	4.98×10^{-2}	PyCBC-BBH
S200118p	2020-01-18T05:07:50	CBC	1.75×10^{-5}	6.41×10^{-4}	BNS	6.41×10^{-4}	PyCBC-broad
S200127o	2020-01-27T11:43:05	CBC	1.57×10^{-5}	1.38×10^{-4}	BNS	1.37×10^{-4}	MBTA
S200127s	2020-01-27T15:27:19	CBC	1.31×10^{-5}	1.34×10^{-4}	BNS	1.33×10^{-4}	MBTA
S200128f	2020-01-28T04:54:04	Burst	2.34×10^{-7}	1.49×10^{-1}	-	-	cWB
S200128p	2020-01-28T09:54:07	CBC	1.40×10^{-6}	1.06×10^{-2}	NSBH	1.02×10^{-2}	PyCBC-broad
S200129ap	2020-01-29T15:39:24	Burst	5.57×10^{-7}	1.50×10^{-3}	-	-	cWB
S200129i	2020-01-29T05:07:00	CBC	9.03×10^{-6}	1.13×10^{-3}	BNS	1.13×10^{-3}	PyCBC-broad
S200208l	2020-02-08T09:01:03	CBC	1.33×10^{-5}	2.75×10^{-3}	BBH	2.75×10^{-3}	PyCBC-BBH
S200209am	2020-02-09T13:14:49	CBC	2.10×10^{-5}	7.40×10^{-5}	BNS	7.40×10^{-5}	MBTA
S200210an	2020-02-10T16:13:46	CBC	1.06×10^{-5}	2.47×10^{-2}	BBH	2.47×10^{-2}	PyCBC-BBH
S200212aa	2020-02-12T10:18:23	CBC	4.82×10^{-6}	1.55×10^{-1}	BBH	1.55×10^{-1}	MBTA
S200213q	2020-02-13T03:43:44	CBC	1.06×10^{-5}	3.58×10^{-4}	BNS	2.79×10^{-4}	MBTA
S200214bq	2020-02-14T22:33:07	CBC	8.68×10^{-7}	2.61×10^{-1}	BBH	2.61×10^{-1}	PyCBC-BBH
S200214br	2020-02-14T22:45:26	Burst	4.17×10^{-9}	9.10×10^{-1}	-	-	cWB
S200218al	2020-02-18T10:05:22	Burst	6.84×10^{-8}	4.88×10^{-1}	-	-	cWB
S200218i	2020-02-18T01:25:25	CBC	2.03×10^{-5}	3.59×10^{-3}	BBH	3.59×10^{-3}	GstLAL
S200219f	2020-02-19T03:09:19	CBC	3.91×10^{-6}	1.34×10^{-2}	BBH	1.34×10^{-2}	GstLAL
S200220v	2020-02-20T04:25:03	CBC	8.19×10^{-6}	1.25×10^{-3}	BNS	9.78×10^{-4}	MBTA
S200220w	2020-02-20T04:51:22	CBC	2.28×10^{-5}	7.00×10^{-6}	BNS	7.00×10^{-6}	MBTA
S200221bh	2020-02-21T15:19:18	CBC	4.51×10^{-6}	1.29×10^{-3}	NSBH	1.29×10^{-3}	MBTA
S200223aj	2020-02-23T13:50:49	CBC	1.18×10^{-5}	4.41×10^{-4}	BNS	4.41×10^{-4}	GstLAL
S200223ao	2020-02-23T14:28:21	CBC	1.47×10^{-5}	4.31×10^{-2}	BBH	4.31×10^{-2}	PyCBC-broad
S200223aw	2020-02-23T18:06:59	CBC	1.53×10^{-7}	2.33×10^{-1}	BBH	2.33×10^{-1}	GstLAL
S200223u	2020-02-23T08:09:27	CBC	3.37×10^{-7}	1.39×10^{-1}	BBH	1.39×10^{-1}	GstLAL
S200224cd	2020-02-24T23:13:13	CBC	1.45×10^{-5}	1.50×10^{-4}	NSBH	1.19×10^{-4}	PyCBC-broad
S200224o	2020-02-24T03:05:24	Burst	1.04×10^{-7}	4.00×10^{-1}	-	-	cWB

S200225as	2020-02-25T14:28:07	CBC	1.37×10^{-5}	3.87×10^{-3}	BBH	3.87×10^{-3}	GstLAL
S200225az	2020-02-25T21:59:37	CBC	4.85×10^{-6}	2.65×10^{-4}	NSBH	1.83×10^{-4}	PyCBC-broad
S200225k	2020-02-25T03:41:20	CBC	1.07×10^{-5}	4.48×10^{-4}	NSBH	4.48×10^{-4}	GstLAL
S200225u	2020-02-25T08:22:49	CBC	1.39×10^{-5}	4.46×10^{-2}	NSBH	3.50×10^{-2}	PyCBC-broad
S200226z	2020-02-26T07:18:43	CBC	4.22×10^{-6}	3.34×10^{-3}	NSBH	2.90×10^{-3}	PyCBC-broad
S200302m	2020-03-02T06:14:02	CBC	3.42×10^{-6}	1.40×10^{-2}	BBH	1.40×10^{-2}	GstLAL
S200303aj	2020-03-03T08:36:14	CBC	2.16×10^{-5}	5.14×10^{-3}	BBH	4.85×10^{-3}	MBTA
S200304ao	2020-03-04T14:46:28	CBC	7.87×10^{-6}	6.56×10^{-3}	BBH	6.56×10^{-3}	GstLAL
S200307ba	2020-03-07T17:53:38	CBC	7.90×10^{-6}	1.04×10^{-2}	BBH	1.04×10^{-2}	PyCBC-BBH
S200307c	2020-03-07T02:34:37	CBC	1.97×10^{-5}	2.71×10^{-3}	BBH	2.71×10^{-3}	GstLAL
S200308g	2020-03-08T01:38:18	CBC	2.97×10^{-6}	2.43×10^{-3}	NSBH	2.43×10^{-3}	GstLAL
S200310b	2020-03-10T00:20:05	CBC	1.58×10^{-5}	2.29×10^{-2}	NSBH	1.67×10^{-2}	PyCBC-BBH
S200310u	2020-03-10T06:21:24	CBC	7.18×10^{-8}	4.79×10^{-3}	BNS	4.79×10^{-3}	MBTA
S200311ba	2020-03-11T10:31:22	CBC	4.10×10^{-8}	1.94×10^{-1}	BNS	1.94×10^{-1}	PyCBC-broad
S200311r	2020-03-11T04:04:20	CBC	1.78×10^{-5}	7.42×10^{-4}	NSBH	4.67×10^{-4}	PyCBC-broad
S200314be	2020-03-14T19:47:18	CBC	2.30×10^{-6}	1.42×10^{-1}	BBH	1.36×10^{-1}	PyCBC-BBH
S200314x	2020-03-14T07:26:14	CBC	1.54×10^{-5}	4.20×10^{-4}	NSBH	4.00×10^{-4}	MBTA
S200316aj	2020-03-16T11:39:17	CBC	9.52×10^{-6}	9.08×10^{-4}	NSBH	9.08×10^{-4}	MBTA
S200318be	2020-03-18T17:57:32	CBC	2.34×10^{-6}	1.97×10^{-4}	BNS	1.97×10^{-4}	MBTA
S200320p	2020-03-20T04:36:30	CBC	7.49×10^{-7}	1.61×10^{-2}	NSBH	1.55×10^{-2}	PyCBC-broad
S200321bb	2020-03-21T22:32:26	CBC	1.82×10^{-7}	3.55×10^{-3}	BNS	3.53×10^{-3}	MBTA
S200323as	2020-03-23T13:53:52	CBC	3.02×10^{-6}	1.72×10^{-2}	BBH	1.72×10^{-2}	GstLAL
S200325j	2020-03-25T07:23:35	CBC	9.14×10^{-6}	1.02×10^{-2}	BBH	1.02×10^{-2}	PyCBC-BBH
S200326af	2020-03-26T11:25:01	Burst	7.51×10^{-8}	4.57×10^{-1}	-	-	cWB
S200326ax	2020-03-26T16:10:49	CBC	1.39×10^{-5}	3.60×10^{-5}	BNS	3.60×10^{-5}	MBTA
S200327g	2020-03-27T02:34:28	CBC	8.91×10^{-7}	2.80×10^{-3}	BNS	2.80×10^{-3}	MBTA
S200327j	2020-03-27T03:15:27	CBC	1.00×10^{-5}	9.57×10^{-4}	BNS	9.34×10^{-4}	PyCBC-broad

Table 4. Details of the joint FAR computed according to the procedure detailed in Section 5.4 for all the triggers with $\mathrm{FAR}_{\mathrm{GRB,max}} < 10^{-3}$ Hz. The RAVEN alert is, by definition, evaluated considering only information received in low latency. The events marked with a (*) are GW candidates with $p_{\mathrm{astro}} > 0.5$.

Name	GW FAR (Hz)	Group	Class	$\sqrt{\mathrm{TS}}$	Joint FAR (Hz)	Raven Alert
S190919ag	3.42×10^{-6}	Burst	-	7.23	2.16×10^{-7}	no
S190919au	3.24×10^{-6}	Burst	-	9.44	7.36×10^{-9}	no
S190919u	8.18×10^{-6}	Burst	-	8.00	8.56×10^{-8}	no
S190930t	1.54×10^{-8}	CBC	NSBH	14.60	5.97×10^{-11}	yes
S191110x	2.93×10^{-11}	CBC	Mass Gap	7.17	9.59×10^{-12}	yes
S191212l	9.31×10^{-6}	CBC	Mass Gap	7.16	4.62×10^{-7}	no
S191219ak	1.22×10^{-6}	Burst	-	7.15	1.19×10^{-7}	no
S191226ae	1.99×10^{-6}	CBC	NSBH	10.70	4.81×10^{-9}	yes
S191229ah	1.23×10^{-6}	Burst	-	8.87	3.15×10^{-9}	no
S200101o	1.66×10^{-5}	CBC	BNS	7.44	4.15×10^{-7}	no
S200108ah	2.16×10^{-5}	CBC	NSBH	7.12	6.77×10^{-7}	no
S200108p	1.93×10^{-7}	CBC	BNS	7.35	1.71×10^{-8}	yes
S200110aa	2.12×10^{-5}	Burst	-	7.06	6.91×10^{-7}	no
S200110d	1.45×10^{-5}	Burst	-	7.29	4.84×10^{-7}	no
S200114f	1.23×10^{-9}	Burst	-	8.82	5.70×10^{-12}	yes
S200117z	1.88×10^{-5}	CBC	NSBH	7.27	5.63×10^{-7}	no
S200130ai	1.78×10^{-5}	CBC	NSBH	16.40	3.13×10^{-8}	no
S200214bo	1.93×10^{-5}	CBC	BNS	7.20	6.15×10^{-7}	no
S200225af	1.64×10^{-6}	CBC	BNS	10.57	4.06×10^{-9}	yes
S200225as	6.23×10^{-6}	CBC	BBH	7.30	2.86×10^{-7}	no
S200225q*	9.19×10^{-9}	CBC	BBH	8.21	1.40×10^{-10}	no
S200303bl	1.75×10^{-5}	CBC	BBH	10.10	3.09×10^{-8}	no
S200304ay	1.89×10^{-5}	CBC	NSBH	7.08	6.74×10^{-7}	no
S200304d	2.21×10^{-5}	CBC	NSBH	7.08	6.90×10^{-7}	no
S200317ag	3.35×10^{-7}	Burst	-	7.36	2.66×10^{-8}	no
S200323bf	6.60×10^{-7}	Burst	-	8.27	1.81×10^{-9}	no
S200324ax	1.85×10^{-5}	CBC	NSBH	10.60	3.24×10^{-8}	no
S200327j	1.66×10^{-5}	CBC	Mass Gap	22.46	2.96×10^{-8}	no